Deposition and Characterization of Wide Band Gap P-Type Metal Oxides for Photovoltaic Applications

Inauguraldissertation

Zur

Erlangung der Würde eines Doktors der Philosophie

vorgelegt der

Philosophisch-Naturwissenschaftlichen Fakultät

der Universität Basel

von

Medina Umar

2022

Genehmigt von der Philosophisch-Naturwissenschaftlichen Fakultät

auf Antrag von:

PD Dr. Thilo Glatzel

Prof. Dr. Ilaria Zardo

Prof. Dr. Paolo Postorino

Basel, 17 November 2020

Prof. Dr. Martin Spiess, Dekan

# Abstract

Daily, the population in the world is increasing, along with the quantity of needed energy. However, the fossils are running out and climate change is a global concern now, thus, the demand for alternative energies is growing. Solar energy comes free by the sun light and, if well harvested, it could be a valuable and readily available alternative source of energy for humanity. In this work, we perform deposition and characterization of thin films of copper oxides to be used in photovoltaic devices.

Thin films of copper oxide were grown by radio frequency-magnetron sputtering in an oxygen-argon environment onto silicon and FTO-coated substrates at two different oxygen partial pressures (15% and 23%). Control over the oxygen flow during deposition is of paramount importance and quite difficult, making reproducible growth challenging. Post deposition annealing in vacuum environment was conducted on the films at different temperatures (between 250°C and 550°C), as an alternative pathway towards the creation of the desired phase and stoichiometry of copper oxide films in a reproducible manner.

We investigated the surface morphology of the thin films by Scanning Electron Microscopy, Energy Dispersive X-ray, Atomic Force Microscopy and Kelvin Probe Force Microscopy. These studies show that the pristine films are made up of densely packed grains that are homogeneously distributed. In the annealed thin films, the size of the grains evolves greatly with the annealing temperature increase: besides the change in the morphology of the grains, which become bigger and less homogeneous, the films become nano porous in the annealed samples. The contact potential difference measurements show the presence of some islands in samples annealed at temperature higher than 450°C, only above this temperature, that the regions with higher and lower CPD values correlated with higher and lower work functions, respectively. Suspecting that these areas represent the co-existence of CuO and $Cu_2O$ crystals.

The structural properties of the thin films were studied via spectroscopy and X-ray diffraction and Raman, which reveal that two oxide phases (i.e. CuO and $Cu_2O$) co-exist in the films deposited with high oxygen ratio. In particular, high oxygen pressure during deposition favours CuO and annealing in vacuum converts CuO to $Cu_2O$. Instead, low oxygen pressure

directly promotes the formation of $Cu_2O$ thin films. In the thin films deposited on glass, we also performed transmission measurements and found that the transmittance of films is higher in the near IR region while absorption is higher at the ultraviolet to visible region of the spectra.

Finally, we uncovered a novel parasitic crystallite growth as a result of aging on the pristine and low-temperature annealed samples, and we found out that high temperature annealing prevents this kind of aging. This aging effect is completely absent in the thin films deposited onto the FTO substrates.

Our results demonstrate the impact of the annealing mediation route in the reproducibility of $Cu_2O$ thin films, which should be explored towards the standardization of copper oxides formation technique. The produced thin films are good substrates for the deposition of $Ga_2O_3$ for dye sensitized solar cells.

# Deposition and Characterization of Thin Films of Wide Band Gap P-Type Mixed Metal Oxides for Photovoltaic Applications

## 1. Introduction

In 1862, Christian Bovee famously wrote in his novel *Intuitions and Summaries of Thought*: "The light in the world comes principally from two sources – the sun and the student lamp" [1]. More than a century after, the world is truly searching for materials to harness the radiation from the sun (solar energy) which is a gold to everything under it. The German physicist Robert Bunsen, together with Gustav Kirchhoff, among several discoveries, found the cause for the dark lines in the solar spectrum. It is famous a story of when Kirchhoff pitched his tent to the sun: when asked whether Fraunhofer's lines revealed the presence of gold in the sun under investigation, his banker's response was "What do I care for gold in the sun if I cannot go and fetch it down here?" However, when England honored Kirchhoff for his discovery with a medal and cash prize in gold, while handing it over to his banker, Kirchhoff said, "Look here, I have succeeded at last in fetching some gold from the sun" [2]. Today, researchers are trying to make the gold in the sun available to everyone in form of cheap, environmentally friendly and sustainable energy, hence the prominence of photovoltaics (PV), which is a crucial renewable energy source. PV is sunlight conversion into electrical current using semiconducting materials that are optically active, i.e. via the generation of free charge carriers upon exposure to light (photovoltaic effect). PV has gained a central stage in the global energy market and its role is expected to rise, if the issues related to the storage and to the conversion of energy are solved. The greatest challenges in the field are the optimization of light absorption, the reduction of electron-hole recombination and, in the case of nanoporous layers in particular, the improvement of charge transport.

For reaching optimal radiation harvest, there are hurdles and challenges to overcome by materials investigation. One of these hurdles is the search for alternative non-toxic materials for environmental sustainability. The first generation of solar cells is mostly based on silicon. These cells have a reasonable efficiency and the technology is well known. However, there are a number of drawbacks to current silicon-based solar cells, like the difficulty to implement them in

a tandem solar cell. Therefore, the research moved to second-generation solar cells, based on viable thin films technologies; they did not replace the first generation of solar cells but seek to address the cost of materials by eliminating the need for wafers. However, also these cells still had several disadvantages. Firstly, they are single band gap cells and, therefore, only a small portion of the solar spectrum will actually be exploited. This is because the material will not absorb photons with energy smaller than the band gap. While photons with energy much higher than the band gap will be absorbed, but they will not be converted efficiently into electric current because the extra energy will not be exploited, as it will be "lost" in the form of heat. Thus, the search for alternative materials for innovative device engineering is gaining more and more attention. Among the novel materials that are attracting attention there are the metal oxides (MOs), some of which are functionally active semiconductors with good tunability in terms of band gap.

The research carried out in this PhD project seeks to contribute to the material research for PV by working on the deposition and investigation of MOs wide band gap materials, more specifically copper oxides. Metal Oxides can be semiconductors, conductors, or insulators but the interest for PV is in the former two, conductors as contacting layers, and semiconductors as active materials.

In general, the recent quest for advancement in nanotechnology made a call for the interest of all bulk materials studied in the past, especially the compound semiconductors, to be synthesized into nanoscale form for further exploitation in modern technological applications. Indeed, some of the material's properties can be engineered and tailored at nano level, making them different from those of the bulk form, like the surface to volume ratio for dye sensitized solar cells. One of the materials that experienced a research revival in recent years, both for its fundamental properties and for the technological applications is copper oxide. This because the awareness of the need for environmentally friendly materials lead to the avoidance of some compound semiconductors whose toxicity level is considered and labelled as 'hazardous' (like, e.g., some arsenide's and sulphide's families of semiconductors) and here our interest material, cuprous oxide, fit into their replacement as a nontoxic metal oxide material. Copper oxide are abundant, nontoxic, and have direct or indirect band gap, depending on the phase. Copper has three known oxides: cupric ($CuO$), paramelaconite ($Cu_4O_3$) and cuprite or cuprous ($Cu_2O$). When

comparing to literatures [3, 4, 5, 6], multiple sources indicate that there is no easy route for obtaining a single phase of the three oxides, confirming our finding that deposition of cuprous oxide is very sensitive to precise deposition parameters.

In this context, we have given our contribution to the research in the field by carrying out a systematic and thorough study of the deposition parameters and resulting properties of copper oxides. In particular, the challenges and the push for detailed research of cuprous oxide material, which this project seeks to contribute to, is the the realization of the desired oxide phase formation between CuO and $Cu_2O$, which we addressed during deposition by tuning the oxygen pressure window and exploiting the annealing mediation post-growth route. In conclusion, the results obtained via several characterization techniques are consistent regarding the two phases of the grown copper oxide. We have also investigated the effect of substrates, and we were able to point out the surface interaction of the $Cu_xO$ layer with a Si and FTO-coated glass substrates. Finally, while studying the stability of the grown $Cu_xO$ thin films, we uncovered novel crystallites growth on the pristine and low temperatures annealed thin films and found that annealing at high temperatures prevents this unwanted growth. We recommend more research in the area of stability studies, which were not addressed before our study.

This work is organized as it follows.

**Chapter 2** is devoted to the theoretical background on MOs and their properties as well as their implementation into devices, with special focus on MOs for photovoltaics. It also describes the general synthesis routes and the previous research, and reports on copper oxide, which is the type of MO on which this work is focused.

**Chapter 3** described the deposition of copper oxide, which sets the beginning of the experimental work related to this project. The synthesis of copper oxide thin films onto Silicon (Si) and FTO-coated glass substrates was conducted via radio frequency (RF)-magnetron-sputtering technique at room temperature with different oxygen (15% and 23%) partial pressure. The substrate choice and preparation are also discussed. A route to improve reproducibility of the properties of the obtained films was tested, that is the post deposition thermal treatment of the thin films.

The characterization techniques are explained in **Chapter 4**. Several methods were employed for the characterization of the deposited thin films. Scanning Electron Microscopy (SEM) and Atomic Force Microscopy (AFM) allowed for a morphological investigation. Energy dispersive X-ray (EDX) was used for the elemental analysis. The electrical characterization was done by the use of Kelvin Probe Force Microscopy (KPFM) that gave the Contact Potential Difference (CPD) of the $Cu_xO$ thin films. The structural investigation was carried out via X-ray diffraction (XRD) and Raman Spectroscopy. Finally, the absorption properties were investigated via a portable UV-Vis Spectrometer.

The analysis of the data obtained by each of the characterization techniques listed above and their obtained results are discussed in **Chapter 5**.

Our work could aid in the reliable and reproducible production of high quality $Cu_2O$ films on different substrates for photovoltaic applications.

<div align="right">

# Chapter 2

</div>

## 2. Theoretical background

This chapter reviews the scientific concepts and the relevant previous results. In Section 2.1, the properties of the metal oxides (MOs), their classification and applications are discussed briefly. In particular, a review on the properties of cuprous oxide as MO is presented. Section 2.2 describes the implementation of MOs in devices, Section 2.3 their photovoltaic applications, while Section 2.4 describes the synthesis methods for MOs and thin films. Finally, Section 2.5 is dedicated to the discussion of the theoretical and experimental investigations of $Cu_2O$ as metal oxide.

## 2.1. Metal oxides and their properties

A metal oxide, as the name suggests, is a combination of two elements, a metal and oxygen, coming together to form a chemical compound. The resulting compound contains at least one oxygen atom and one metal element in its chemical formula. Metal oxides form an important group of multifunctional materials with diverse structural, electronic, magnetic, and optical properties, and, as semiconductors, are promising materials for photovoltaic applications. Many MOs are abundant, non-toxic and chemically stable, therefore interesting materials for further research and development and play important roles in chemistry, material science, and physics [7, 8, 9]. For example, the metal elements are able to form a large diversity of oxide compounds leading to wide range of crystal structures with an electronic structure that can exhibit a metallic, semiconducting or insulating character [10, 11, 12]. Some of the metal atoms exhibit multiple oxidation states. This is the case, for example, for vanadium, molybdenum and manganese that have five different stable oxidation states and hence participate in redox reactions. Some metals, instead, possess only one oxidation state. The nature of the metal-

oxygen bonding varies between nearly ionic to highly covalent or metallic [13]. Most of the MOs involve the transition metals. MOs can be insulators, conductors, or semiconductors (p-type or n-type) with direct or indirect optical band gap that is useful in several industrial and technological applications, such as photovoltaics (PV), optoelectronics, and photonics. See Table 2.1 for the presentation of some MOs along with their main properties, such as position of the metal in the periodic table, metal element category, band gap energies, conduction type and crystal structure.

MOs are mostly crystalline and their structural properties are examined systematically via different characterization techniques. In thin film investigation, the structural characterization is typically performed after the chemical composition analysis to identify the chemical elements. The structural quantitative analysis is performed to determine the structural composition i.e. the detailed information about atomic arrangement, and organization of interrelated elements. The chemical compositions, and the morphological and structural properties can be analysed via some specific techniques such as Scanning Electron Microscopy, Energy dispersive X-ray, Atomic force Microscopy, Kelvin Force Microscopy, Raman spectroscopy and X-Ray Diffraction. The listed techniques were employed in the analysis of the deposited metal oxide in this work (i.e. $Cu_2O$ and $CuO$) and will be discussed in Chapter 4.

| Metal oxide names | Periodic table position | Element category (metal) | Band gap (eV) | Conduction Type | Crystal structure | References |
|---|---|---|---|---|---|---|
| Titanium oxide ($TiO_2$) | group 4 (IV) | transition | 3.2 – 3.05 | n-type | Rutile, brookite and anatase | [7] |
| Vanadium oxide ($V_2O_5$) | group 5 (V) | transition | 0.7 | p-type | distorted rutile | [14] |
| Tungsten oxide ($WO_3$) | group 6 (VI) | transition | 2.6 - 3.1 | p-type or n-type | monoclinic | [14] |
| Molybdenum oxide ($MoO_2$) | group 6 (VI) | transition | 1.96 | n-type | BCC | [15] |
| Manganese oxide (MnO) | group 7 (VII) | transition | 4.1 | p-type | halite | [14] |
| Iron oxide (FeO) | group 8 (VIII) | transition | 2.4 - 2.5 | p-type | spinel | [7, 14] |
| Ruthenium oxide ($RuO_2$) | group 8 (VIII) | transition | 2.2 | amphoteric | rutile | [7] |
| Cobalt oxide (CoO) | group 9 (IX) | transition | 2.4 | p-type | FCC | [16, 17] |
| Nickel oxide (NiO) | group 10 (X) | transition | 3.6 - 4.2 | p-type | FCC | [17] |
| Cuprite oxide (CuO) | group 11 (XI) | transition | 1.11-1.51 | p-type and /or n-type | monoclinic | [18] |
| Cuprous oxide ($Cu_2O$) | group 11 (XI) | transition | 2.32-2.62 | p-type | Tetragonal | [18, 19] |
| Cadmium oxide (CdO) | group 12 (XII) | transition | 2.2 - 2.9 | n-type | FCC | [10] |
| Zinc oxide (ZnO) | group 12 (XII) | transition | 3.3 | n-type | Wurtzite | [10, 20] |
| Gallium oxide ($Ga_2O_3$) | group 13 (XIII) | other | β 4.7-4.9 | n-type | α trigonal β monoclinic | [16] |
| Tin oxide ($SnO_2$) | group 14 (XIV) | other | 3.7 | n-type | simple primitive | [10] |

**Table 2.1:** Few examples of MOs and their main characteristics.

In order to understand the optoelectronic properties of the material, the band structure is an important aspect that explores the electronic level in an ideal crystal structure. The band structure in MOs is critical in determining the ranges of energy levels of the electrons and the prohibited energy levels, known as the bandgap. Metals are known for their partially filled energy bands; hence, the band theory predicts electron delocalization and metallic properties. Nevertheless, in reality, some of their oxides exhibits insulating behavior implying that the d-electrons are localized. The short-range Coulomb repulsion of electrons can prevent formation of the band states that are stabilized by the localized electron states [13, 21]. Some MOs are being studied for their optical properties, which describe a material's response to electromagnetic radiation exposure, in particular, reflection, absorption, transmission of photons in relation to the material's optical constants are studied. The optical properties of MOs can be determined via the analysis of their band gaps and this is vital to their PV and optoelectronic applications [22]. In looking at the magnetic properties, several MOs formed with transition metals exhibit ferromagnetic behaviour like e.g. NiO, $Fe_2O_3$ and $Co_3O_4$. This magnetic property sparks from the unpaired electrons in (n-1) d-orbital while the MOs with paired electrons exhibit diamagnetic behaviour. The magnetic properties of MOs are heavily investigated for their utilization in the field of electronics, for instance in $\alpha$-$Fe_2O_3$ nanofibers and nanotubes [7, 23]. Finally, the electronic properties of MOs cannot be overlooked, MOs can possess ionic or mixed ionic/electronic conductivity and both are influenced by the size of the solid (bulk or nano). The electronic conduction can be n- or p- type doping depending on the principal charge carriers (electrons or holes, respectively). Ionic conduction is in place when ions can hop from one site to another within a crystal lattice due to thermal activation [24].

## 2.2. Implementation of metal oxides in devices

MOs have been incorporated in devices for well over a century. The implementation of some of the MOs in devices includes microelectronic circuits, sensors, piezoelectric devices, fuel cells, corrosion-resistant coatings, catalysis, field emission, magnetic memory, photoelectrochemical cells and solar cells. In particular, MOs widespread utilization goes from active or passive components in a broad range of available applications, e.g. as active channel layer in transistors [25, 26], transparent conducting front electrodes [27]. All-oxide photovoltaic

cells [28, 29], Active Matrix Organic Light Emitting Diode (AMOLED) displays [30], hetero-interfaces for solar cell applications [20, 31], gas sensors [32], photocatalytic activity studies [33, 34], and as a catalyst for redox reaction in composite material and water treatment [35]. MOs have also been incorporated into biodegradable polymers with a high capacity to form macromolecular metal complexes [17]. Bio-nanomaterials have $Fe_2O_3$ nanoparticles as SPION: superparamagnetic iron oxide nanoparticles that act as antitumor agents [36]. Nanoscale ZnO is widely used in organic solar cells as electron transporting layer. All of these properties that have engineered the wide utilization of MOs can be influenced by particle sizes.

Material sizes and interfaces are important factors in the incorporation and applications in devices. Indeed, the physical-chemical properties of MOs are highly influenced by their particle sizes, especially if they are in the 'nano' domain, via two major factors that are surface effects and quantum effects [37]. As the particle, size reduces to tens of nanometers, the ratio of surface to bulk atoms increases. This results in a higher number of chemically active sites and in a modified density of electronic states at the surface of the particles [38]. Notably, the nano-scaling not only increases the active surface area, but it also induces new effects due to quantum confinement, e.g. band gap widening opening up more opportunities for material engineering. Amongst the applications that benefit specifically from these modified properties, there is an area of PVs where nanostructured MO thin films are applied, as it is further discussed in Section 2.3.

## 2.3. Metal oxides for photovoltaic application

PV is the best of the four sources of green energy generation, the others being thermal, wind and hydro energy. PV is the conversion of sunlight into readily usable electricity using semiconducting materials that exhibit photovoltaic effects. The photovoltaic effect is the creation of voltage and current in a material upon exposure to light and it is both a physical and chemical phenomenon studied in physics, photochemistry and electrochemistry. A photovoltaic system popularly known as solar power system is designed to accommodate components such as solar panels (arrays) to absorb and convert the radiant light from the sun into electricity, an inverter for the conversion of the output from direct current to alternating current and other electrical accessories like cables and a solar tracking system [39]. Ref [40] summed up a brief definition of photovoltaics as the science and technology of solar cells. Therefore, the name photovoltaics and

solar cells are interchangeable. Solar cells are classified based on their modus operandi or historical evolution. The evolution is currently at its third generation. The first-generation solar cells were made up of single layer p-n junction diode, based on silicon as semiconducting material. The photoexcited carriers in the p-n junctions are separated into mobile carriers by the built-in electric field or band bending at the p-n junction. The photo voltage in the p-n junction arises from the difference in quasi-Fermi levels (i.e., the band bending) of n-type and p-type regions.

The challenge of this generation of solar cells was the inherent limitation between the absorption and radiative recombination in the crystals, i.e. the Schockley-Queisser limit on the photovoltaic conversion efficiency. The power conversion efficiency's theoretical prediction places a 32% upper limit for single junction (p-n) solar cells [41]. The second disadvantage is the production of high quality silicon, which comes at a high cost. The use of polycrystalline materials later overcame the cost limitations [39]. However, these limitations gave birth to research into thin film solar cells to replace the active materials, resulting in the second generation of solar cells. Thin film solar cells are made by depositing one or more thin layers of photovoltaic material on substrates such as silicon wafers, plastic, metal or glass (see sec. 2.4 for more details). This generation of solar cells typically involves charge separation at an interface [40].

The third generation of solar cells are to emerge from the combined design of the two previous generations merging their advantages and disadvantages. It was predicted not to possess the Shockley- Queisser limit that has been the major hindrance to the former. Examples include copper zinc tin sulfide (CZTS or $Cu_2ZnSnS_4$) solar cells, perovskite solar cells, dye sensitize solar cells (DSSC), organic photovoltaics (OPV), and the quantum dot and nanowires solar cells, in which quantum dots and nanowires are in use as sunlight harvesters. The third-generation solar cells thicknesses are expected to be less than a micrometer [42].

If we consider the typical setup of MO based solar cells, the MOs play a key role as active layer or as a contact layer in a PV's cell structure, depending whether the MO is semiconducting or conducting. For example a typical cell structure includes soda lime glass as the substrate, MO layer as the back contact, Copper Indium Gallium Sulphur as the absorber layer, cadmium sulfide (CdS) or Zn (S,OH)x as the buffer layer, and ZnO:Al as the front contact

[43]. In the DSSCs structure, a wide-band-gap MO, such as $NiO_2$, $TiO_2$ and ZnO, that offers high electron mobility and affinity is, anchored to dye [44]. In reference [45], the author concluded that the success in the field of organic PVs came mainly due to the incorporation of transition metal oxides, which offer a wide range of optical and electronic properties, making them practically applicable in organic-based PV in different capacities due to the intrinsic charge carrier mobility found in many MOs.

In the perovskite PV, the cell structure typically includes a metal back contact of one of Al, Au or Ag. A hole transfer layer (spiro-MeOTAD, P3HT, PTAA, CuSCN, CuI, or NiO), an absorber layer ($CH_3NH_3PbI_xBr_{3-x}$ or $CH_3NH_3PbI_xCl_{3-x}$ or $CH_3NH_3PbI_3$), an electron transport layer (TiO, ZnO, $Al_2O_3$ or $SnO_2$), and a top contact layer (fluorine doped tin oxide (FTO) or tin doped indium oxide (ITO)) [46]. One of the quaternary compounds gaining recognition for its good properties is a I-IV compound semiconductors of $Cu_2ZnSnSe$ or $Cu_2ZnSnS$ with about 1.45eV to1.6 eV band gap, non-toxic, readily available and absorption coefficient [47]. The basic structural layout for this solar cell is outlined as follows. Molybdenum on glass substrate as a contact layer, followed by the CZTS as p-type absorber layer, on top is deposited a thin layer of CdS as a buffer for band alignment, and is sealed with ZnO as a window layer and finally an n-type indium Tin oxide as transparent conducting oxide [48].

Now, we look at an organic photovoltaic (OPV). Light absorption from the solar spectrum is guaranteed for organic semiconductors solar cells and this leads to current generation because of the presence of a conjugated system though their charge carrier mobility is low (due to the short lifetime of the generated exciton) but higher absorption coefficients. An example arrangement is an OPV with $CuGaO_2$ as hole transporting layer and PEDOT:PSS as the dye molecules and the and another MO for top the layer eMoO3 [49].

Quantum Dots Solar Cell (QDSC): The merits of quantum dots are multiple generation of excitons, and sizes. The simple structural arrangement in a solar cell is MOs as photoanode, quantum dots as sensitizers, electrolytes and counter electrodes. Moreover, the narrow band gap quantum dot MOs are used to increase the absorption areas in dye sensitized solar cells. [50]

Semiconductor nanowires solar cell growth is unique because it can be grown elsewhere and be transferred to a desired substrates, this is called manipulation and this can be useful in solar cell fabrication. Nanowire semiconductors for solar cells are unique in their sizes: typically,

100nm-2µm in diameter, interestingly, when wire diameters are decreased, the band gap increases [51]. There are vertical arrays structure and planar arrays, the disadvantage of the later is the high reflection losses.  For typical solar cells nano wires, the sequence of fabrication is from synthesis to junction formation (i.e introduction of charge separation and collection to cause chemical potential difference that mediate the flow of electron and hole in opposite directions) followed by contact deposition to extract electrons and holes, ohmic contact techniques like interfacial layers and doping can be adopted. [52], reported nanowire solar cells are hybrid and dye sensitized SiNWs incorporated with Si quantum dots: core shell Si/PEDOT:PSS layer heterojunction SiNWs, where the heterojunction is the combination of inorganic materials and SiNWs for enhanced performance of solar cells. MO nanowires are also investigated, the most reported MO NWs are $SnO_2$, ZnO, $In_2O_3$, and $WO_3$, $In_2O_2$, TiO2, $V_2O_5$, $Sb_2O_5$ and $Ga_2O_3$ [53]. Some MO nanowire structures are:$MoO_3/Ag/MoO_3/TiO_2$ composite electrode NPs and AgNMs [54]. Au or $Ag/p-Cu_2O/n-ZnO$ [55].

## 2.4. General synthesis methods for metal oxides and thin films

*"Deposition"* defines the process to produce a (thin) film of material unto substrates or unto previously deposited layers and can be achieved by several methods. The deposition methods may be broadly classified under three headings: Chemical Vapor Deposition (CVD), Solution Based Chemistry (SBC), and Physical Vapor Deposition (PVD). Each technique can be subdivided into different subclasses [56, 57] as shown in Fig. 2.1.
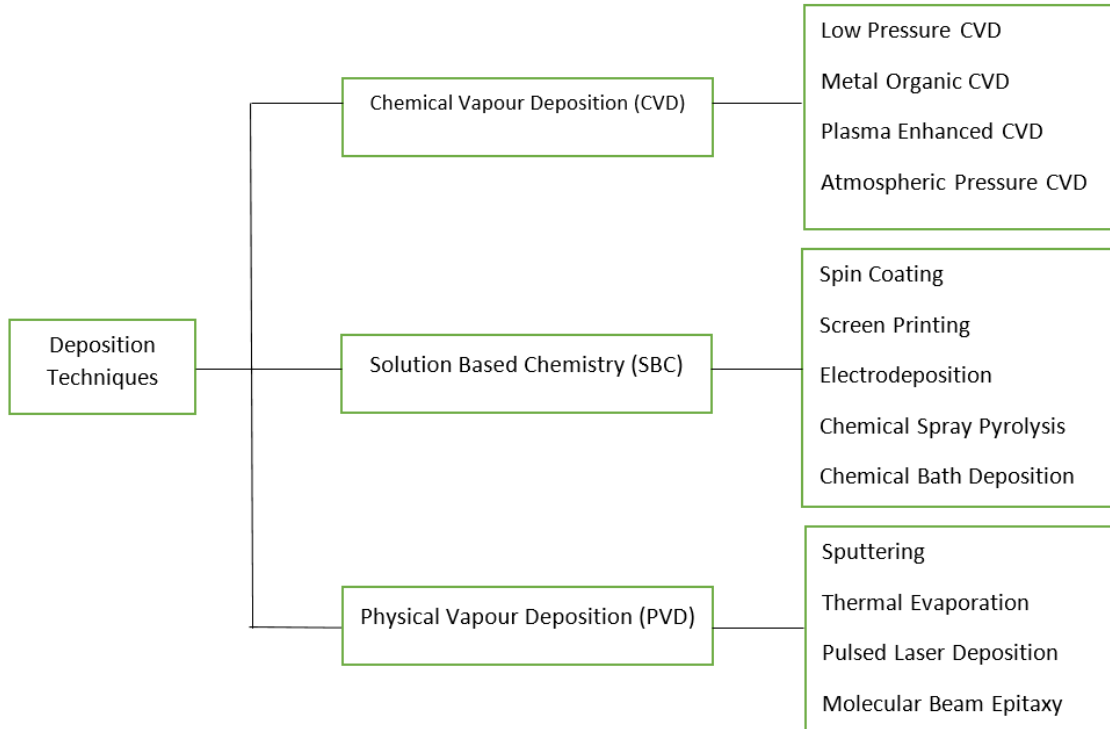
**Figure 2.1:** Thin films deposition techniques [57]

Each synthesis technique from Fig. 2.1, e will be discussed briefly below; CVD is the formation of a non-volatile solid film on a substrate by the reaction of vapor phase chemicals (reactants), that contain the required constituents, with a surface [58]. All other by-products of the reactions are gaseous and pumped out of the system. For some processes, plasmas can help to generate the reactive species. CVD is useful for a large number of deposition processes in the semiconductor industry [58, 59]. CVD processes have some disadvantages, which include the possibility of carbon contamination from metal organic precursors in the films, adhesion problems under certain conditions, limitations on temperature for compatibility with the substrate, the shelves-life of the precursors and possible side reactions. For the advantages, large surface area can be deposited at once and the process pressure can be controlled.

SBC techniques include chemical bath deposition, spin coating, spray pyrolysis, and screen-printing among others. These techniques involve chemical reactions at the liquid state and have the ability to produce materials with high yield and uniformity. SBC is used for the deposition of multi-functional coatings on glass and polymeric substrates. Examples are water

repellent coatings, antireflective coatings, transparent conductive coatings, porous films, metallic mirrors, and many other applications [60].

Thermal Evaporation is the simplest, most convenient, and most widely used method for the preparation of thin films. In this method, the material vaporizes by heating it to a sufficiently high temperature and condensation occurs onto a relatively cooler substrate yielding thin solid films. Several variants include (i) arc evaporation, (ii) radio frequency heating, (iii) laser evaporation, (iv) electron bombardment heating, (v) resistive heating, (vi) flash evaporation, and (vii) exploding wire technique. A simple arrangement of a thermal evaporation chamber is shown in Fig. 2.2. The target material for evaporation is placed on a filament boat through which a heating current passes and the material is deposited on the substrate attached to the heater. This setup is located in a vacuum chamber [61, 62]

Physical Vapor Deposition (PVD) processes consist of atomistic deposition whereby materials are vaporised from a solid or a liquid source in the form of atoms or molecules and transported in the form of a vapor through a vacuum or low pressure gaseous environment to the substrate (anode) where it condenses or sublimes. A common feature to almost all PVDs is that they require a high vacuum level (pressure $10^{-6}\,mbar$) to avoid impurities in the film. Besides, loss of energy of particles from the solid source due to collisions is also avoided, so that the bombarding particles can keep enough energy in a sputtering (ions) or in an evaporation (electrons and/or ions) process. PVD deposition rates are 1-10 nanometers per second. PVDs are considered a cold process because the substrate is not deliberately heated or exposed to intense bombardment by charged particles. If the chosen substrate and film itself can endure higher temperatures then an auxiliary additional heating may be applied, if needed to promote the film growth and to improve the adhesion and the film properties. For the deposition of compound materials like oxides and nitrides, it is necessary to introduce a gas such as e.g. oxygen, nitrogen, into the chamber. The possibility of the process control, the resulting high purity of the films, and the choice of the substrate materials are among the reasons for the wide spreading of PVD methods in thin film technology. The categories of physical vapour deposition processing are thermal evaporation, sputtering deposition, arc vapour deposition, and ion plating [61, 63].
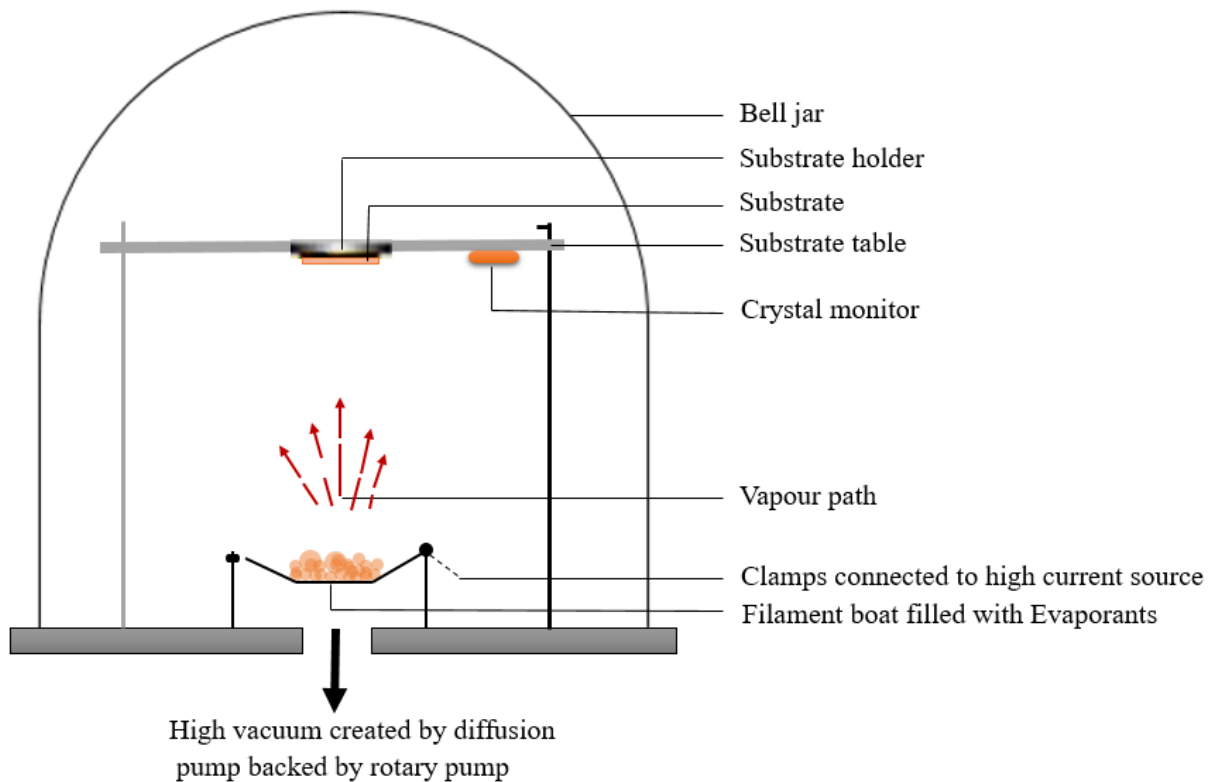
**Figure 2.2:** A schematic diagram of resistive thermal evaporation system [62].

We will now discuss the sputtering technique in more detail, as it was the technique employed in this work. Sputter deposition is the deposition of particles coming from a surface (target) being sputtered. Sputtering is one of the most versatile techniques used for the deposition of metal back contacts and for deposition of transparent conductors when standard device quality is required. Sputtering process produces films with better-controlled composition, thin films with greater adhesion, homogeneity and enables better control of thickness than some other techniques. The sputtering process involves the creation of a gas plasma (usually from an inert gas such as argon, or nitrogen) by applying a voltage between a cathode and an anode [63, 64]. In particular, energetic ions (usually argon ions) from the plasma of a gaseous discharge bombard a target that is the cathode of the discharge. The target atoms are ejected and settle upon a substrate surface (attached to the anode), forming a coating i.e. a deposited layer of film [65]. During the collision the energy and momentum transferred to the film from the mass of the bombarding species is conserved. Thus, from the laws of the conservation of energy and the

conservation of momentum, the energy, $E_t$, transferred by the collision between the surfaces is given by equation [61] below:

$$E_t/E_i = 4M_t M_i cos^2\theta/(M_i + M_t)^2. \qquad\qquad (2.1)$$

where, $E$ = energy, $M$ = mass, the subscripts $i$ and $t$ indicate the incident and target particle, respectively, while $\theta$ is the angle of incidence as measured from a line joining their centres of masses. Sputtering is normally performed in a vacuum environment (pressure $2\times10^{-6}$ mbar) [19].

There are two modes of powering the sputtering system, namely Direct Current (DC) and Radio Frequency (RF) biasing. In a typical DC diode sputtering deposition, the target (source) and the substrate are placed parallel to each other inside a chamber filled with inert gas (Ar). The DC sputtering system involves the application of a direct voltage between the cathode and the anode. This method is restricted to conducting materials only. DC sputtering for the deposition of dielectrics is not advisable, as the insulating cathode will cause charge build up during $Ar^+$ bombardment. Successful deposition of metal back contacts by DC sputtering was reported in ref. [66].

Some advantages of sputtering over some other techniques are:

1. Parallel plate source, resulting into good uniformity;

2. All components sputtered with similar rate, thus maintaining the stoichiometry;

3. High energy atoms/ions (1-10 eV), thus leading to denser films, smaller grain sizes and better film adhesion than other techniques;

4. It is easier to deposit materials with a very high melting point;

5. It can be combined with reactive gasses, like oxygen, to change the stoichiometry.

In general, MO thin films and the study of related structures like surfaces and interfaces involves various types of deposition methods among those listed above. Each method of deposition is carefully chosen not only for fabrication purposes but also for achieving a precise chemical and structural control for specific applications. The RF-magnetron technique was employed in the deposition of thin films within the frame of this work and, therefore, this

technique will be discussed in details in chapter 3, section 3.1, while the thin film deposition is discussed here in details.

In this work we focus on thin film deposition. Thin films possess special properties: e.g. they can exhibit different density or strain level, have defect structures different from bulk films, be quasi-two dimensional, and be strongly influenced by surface effects which change the electrical, chemical, magnetic, thermal, optical and mechanical properties of the films. The coated component can also have unique properties achievable in other ways like using two methods to produce a film where the first coating method is different from the second coating, with these methods each thin film fabrication technique has unique properties but each technique has intrinsic strengths and weaknesses as well as specific advantages for specific applications. Moreover, each technique varies widely in terms of system configuration, consisting of various reactor types, and reaction co-product removal [67, 68]. In sputtering, to yield good thin films, there are some processing steps that could help as listed in the next paragraph. Thin films are important because of their low cost of fabrication, large areas, and the possibility of convenient integration with other devices. They can be obtained by unique growth process that makes it possible to tailor-make materials with desired properties [63].

There are in total five successive processing steps involved in a thin film deposition: i. provision of film-forming material source (may be a solid, liquid, vapour or gas), ii. transportation of material to substrates, iii. deposition, iv. annealing (sometimes), and v. evaluation of the process by analysis techniques. The result of the analysis helps to adjust conditions for modification of film properties for further iteration of the process. In all steps, process monitoring is valuable and contamination is always a key concern [63].

Of all the different deposition methods that exist and some discussed here, the following techniques have been successfully applied for the deposition of copper oxide thin films: chemical deposition [11, 69, 70], oxidation [71, 72], electrochemical deposition [73], magnetron sputtering techniques via direct current [74, 75, 76] and radio frequency [4, 5, 77, 78, 79]. It is of extreme importance and significance to select an appropriate methodology when growing a specific metal oxide structure (bulk or nano) as this influences the morphology and structure of the material and, consequently, its properties with an impact on the target application. The properties of the investigated MO are discussed next.

## 2.5. Properties of the investigated metal oxide: $Cu_2O$

Copper (Cu) is a metal whose name comes from 'cyprium aes', the Latin term for metal of Cyprus, where it was first discovered; it is an orange/red metal that is highly conductive. Copper is heavily used as an industrial metal, in both alloy and unalloyed form. In the periodic table, it belongs to group 11, period 4, block d, has atomic number 29, atomic mass of 63.546 u, density of 8.96 g $cm^{-3}$, and has electronic configuration of $3d^{10}4s^1$. The metal oxide formation is a result of the Cu affinity for oxygen; Cu exhibit ionic bonds to form oxides with oxygen that belongs to p-block of the periodic table. It has three known oxides namely, cupric oxides (CuO), paramelaconite ($Cu_3O_4$), and cuprous oxides ($Cu_2O$) [19]. The oxide growth kinetic depends largely on the oxygen partial pressure thus, a very slim window of deposition parameters for obtaining a specific oxide exists and the distinguishing factors are the growth parameters, especially the process pressure. Copper oxides are nontoxic, cost effective and formed with different deposition techniques. From the equilibrium phase diagram, $Cu_2O$ ($Cu^+$) and CuO ($Cu^{2+}$) are stable. However, other metastable phases like $Cu_3O_2$ can be obtained at low temperature of oxidation of copper ($< 300°C$), as reported by Lenglet et al. [80].

Cupric oxide (also called Copper (II) oxide in the IUPAC notation) has a monoclinic symmetry, with four Cu-O molecules in the unit cell, see Fig. 2.3a [81], and the band gap energy is still an active field of study but the reported values are 1.21-1.5eV, it is the most stable of the three oxides [69, 82, 83].

The second oxide, paramelaconite, was discovered in 1870 as mineral in the copper queen mine at Bisbee, Arizona, USA. It is called paramelaconite from the Greek word παρά meaning "near" and the word melaconite (tenorite, which is CuO, was known then as melaconite so paramelaconite means near CuO, since it was originally found near it). It has a band gap of about 1.34eV and a tetragonal lattice [84, 85] . On this material there are very few studies but in one of them, Fondel established the space group to be $I4_1/amd$ $\{I4_1/a\ 2/m\ 2/d\}$ [85]. O'Keeffe and Bovin found that the formula is $Cu_4O_3$, specifically as $Cu_2^{1+}Cu_2^{2+}O_3$, claiming that Fondel gave the composition as $CuO_{0.884}$ without resolving the structure [86]. The other contributors to the crystallographic studies of paramelaconite are Datta and Jeffery [87].

The third oxide, cuprous oxide (or copper (I) oxide in the IUPAC notation), has the copper ion with a +1 charge and the oxygen ion with -2 charge, therefore, two copper (I) ions are required to knock off one oxygen ion; the formula is thus:

$$2Cu^{+1} + O^{-2} \rightarrow Cu_2O. \qquad\qquad (2.2)$$

Regarding the history of $Cu_2O$, the first reported $Cu_2O$ deposition was in August 1925 by L.O. Grondahl and documented as 1.640.335 file at the United States patent office for an unidirectional current-carrying device based on a $Cu_2O$-metal contact [88]. This marked the start of current semiconductor electronics, preceding the now standard silicon. L. O. Grondahl and P. H. Geiger [89] worked on a copper-$Cu_2O$-solar cell and established that $Cu_2O$ is a p-type semiconductor. With the world shifting attention to clean energy and the depletion of fossil fuels, $Cu_2O$ is beginning to regain attention for its usage in the solar energy industries, especially due the direct band gap energy of 2.1 eV and the prediction of a 20% theoretical efficiency based on the Shockley-Queisser limit [90, 91, 92]. Over the years, the reported optical band-gap energy values range from 2.1 to 2.62 eV [3, 5, 77, 93] and interestingly the band gap can be slightly tuned by tuning the grain sizes through recrystallization especially by annealing.

Cu$_2$O is naturally a cation ion deficient and hole conductor. Cu$_2$O crystallizes in a cubic lattice structure (see Fig. 2.3a). The unit cell has six atoms, with four copper atoms positioned in a face centered cubic (FCC) lattice (grey balls), and two oxygen atoms at tetrahedral sites forming a body centred cubic (BCC) sub-lattice (red balls). Overall, oxygen atoms are fourfold coordinated with copper atoms as nearest neighbours and copper atoms are linearly coordinated with two oxygen atoms as nearest neighbours [12, 18, 94, 95]. The reciprocal lattice of the brillouin zones of the two most common types of copper oxides are shown in Fig. 2.4. The space group is Pn$\overline{3}$m for Cu$_2$O. The physical and crystallographic properties of Cu$_2$O are tabulated in table 2.2.
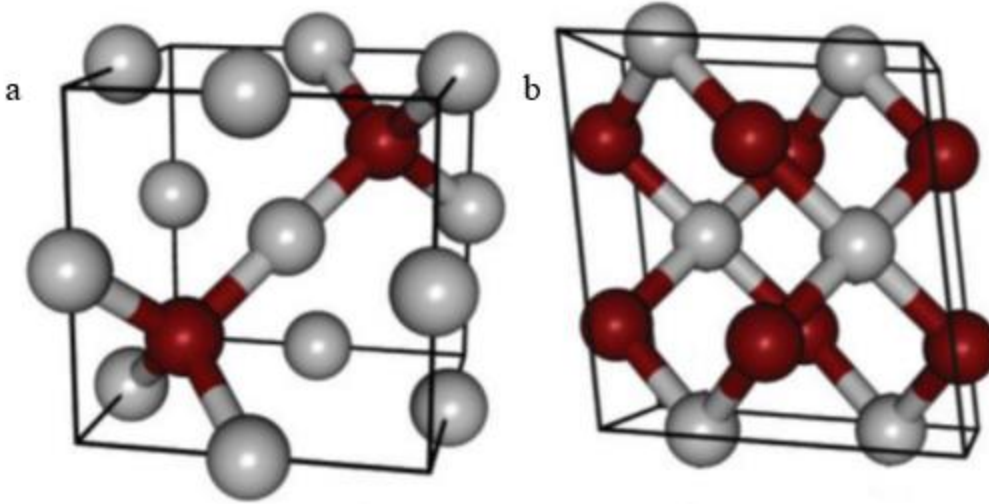
**Figure 2.3:** Present the primitive cell for Cu$_2$O (panel a) and CuO (panel b). Copper atom is represented by the grey color and oxygen atoms by the red color. Adapted from ref. [96]
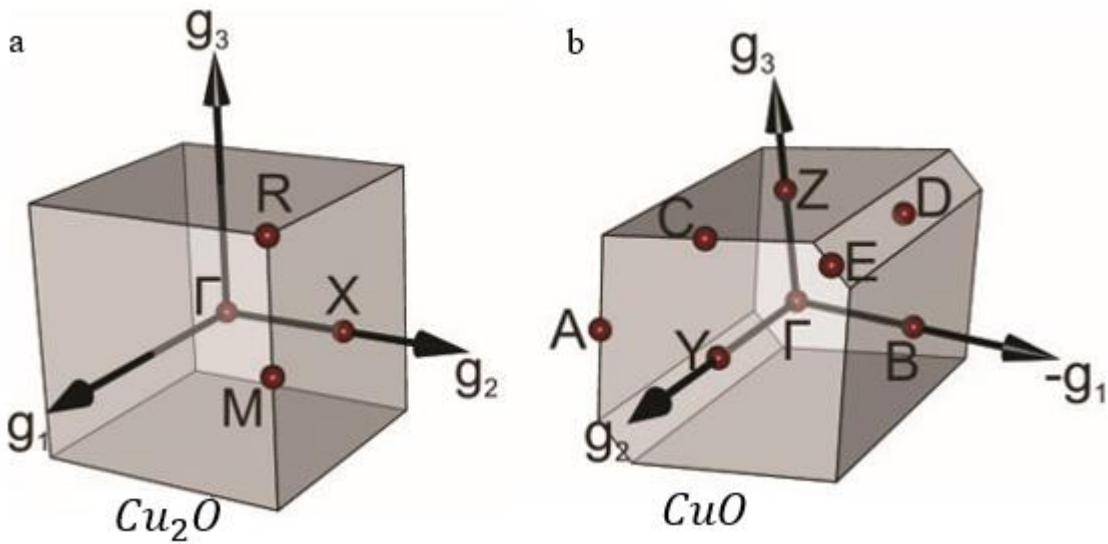


**Figure 2.4:** The Brillouin zones of Cu$_2$O (panel a), and CuO (panel b). The alphabetic letters represent high symmetric points and the $\Gamma$ is the center zone. Adapted from ref. [18].

| Crystallographic properties | | Physics Properties | |
|---|---|---|---|
| Lattice constant | 4.2696 Å | Young Modulus | 30.12 GPa |
| Space group | Pn$\bar{3}$m  224 | Shear Modulus | 10.35 GPa |
| Cu-O Bond length | 1.849 Å | $c_{11}$ | 116.5 -126.1 GPa |
| O-O Separation | 3.68 Å | $c_{12}$ | 105.3 - 108.6 GPa |
| Cu-Cu Separation | 3.012 Å | $c_{44}$ | 12.1- 13.6 GPa |
| Cell volume | 78.833 | Thermal expansion coefficient | $2.3*10^{-7}\,K^{-1}$ |
| Molar weight | 143.09 g/mol | $\varepsilon(0)$ | 7.11 |
| Density | 6.14 g/cm$^3$ (measured) 6.15g/cm$^3$ (calculated) | $\varepsilon(\infty)$ | 6.46 |
| Melting point | 1235 °C | Electron affinity | ~ 3.1 eV |
| Boiling point | 1800 °C | Work function $\Phi$ | ~ 4.84 eV |
| Hardness | 3½ - 4 on Mohs scale | | |

**Table 2.2**:  Crystallographic and general properties of cuprous oxide [92, 97].

The quality of copper oxide depends greatly on the preparation. Various deposition methods have been utilized to obtain high quality films of cuprous oxide. The main categories of the deposition techniques were discussed in section 2.4. Table 2.3 shows some radio frequency sputtered thin films deposition parameters available in the literature and their yields in terms of copper oxide phases based on partial pressures, temperature and power. From the existing RF magnetron sputtering results, the best temperature for high quality $Cu_2O$ yield is between 450 and 500°C [4, 93].

| Target material | Temp (°C) | Working Pressure (mbar) | Partial pressure (%) | Power (W) | Phase yield | Refs |
|---|---|---|---|---|---|---|
| Cu | RT and 500 | 0.06, 0.07, 0.08 mbar | $Ar/O_2 = 79/21$ | | $Cu_4O_3$ $Cu_2O$ Metallic Cu | [4] |
| Cu | RT | $2.66*10^{-6}$ | $Ar/O_2 = 60/40$ | 300 | CuO, $Cu_2O =$ $500°C =$ | [5] |
| $Cu_2O$ | RT | 0.0133, $6.66*10^{-3}$, $1.33*10^{-2}$ mbar | | 40 50 80 | $Cu_2O$ $Cu_xO$ CuO | [77] |
| Cu | 200 | $3*10^{-2}$ mbar | $Ar/O_2 = 20$ | 40 | $Cu_2O$ | [79] |
| $Cu_2O$ | RT | $2*10^{-5}$ mbar | $Ar = 17$ | 100 | $Cu_2O$ CuO | [98] |
| Cu | RT and 500 | $2.0*10^{-3}$ mbar | | 80 | $Cu_2O$ | [99] |

**Table 2.3**: Deposition parameters and copper oxide phase yield on RF-sputtered Cu-O films from literature.

The above listed deposition techniques were performed onto different substrates such as silicon wafers [5, 6, 98], stainless steel substrates [78], soda-lime glass [4, 100], glass, quartz, or fibre glass substrates [72, 76, 77], polyethylene terephthalate and plastic substrates [30, 99], and co-fired ceramics substrates [101]. For epitaxial growth of $Cu_2O$, MgO substrates were used due to the compatibility in terms of their lattice constant. Indeed, both possesses cubic unit cells with comparable lattice parameters, i.e., 4.213 Å (MgO) and 4.269Å ($Cu_2O$) [94]. Below we'll describe in more detail the morphologies that evolved from both the deposition techniques and substrates.

Depending on the deposition technique and parameters, different shapes and sizes of crystallites can form. The two mechanisms influencing crystallite formation are deposition anisotropy and surface diffusion. The morphologies of the crystallites also differ, largely depending on the processes. The most commonly reported morphologies aside cubic are tetragonal [4, 78] and octahedral [7, 69]. Recent studies on morphology evolution revealed that dendritic morphology, 8-pod branching growth of $Cu_2O$ crystals increases their efficiency for the various applications, and highly symmetric branching growth of $Cu_2O$ structures yields higher surface area [71, 102]. From the deposition techniques to substrates and morphologies, the desired result is to get films with optimal properties, thus, the next paragraph examines this aspect.

Opto-electronic properties are important in MOs, hence also in $Cu_2O$. The electrical and transport properties of cuprous oxide were reviewed in 1951 and the role of defects in cuprous oxide was established. It was found that cuprous oxide is a semiconductor with natural defects that has its impurities as acceptors [103], the other contributors are the the Cu vacancies and the oxygen interstitials [104].  In order to discuss the optoelectronic properties of $Cu_2O$, we have to consider their band structure. In a pure ionic description of $Cu_2O$, the highest valence band is d-like in character and made up from the $3d^{10}$ states of Cu. Two different theoretical electronic dispersion curves are considered in Figs. 2.5 and 2.6.
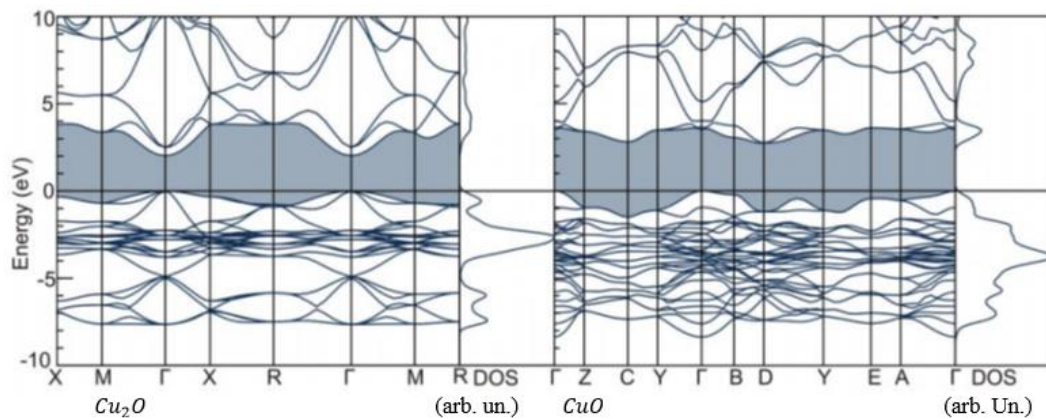


**Figure 2.5:** Electron dispersion curves and electronic density of states (DOS) for $Cu_2O$ (left) and CuO (right) determined by hybrid functional DFT calculations. [96].
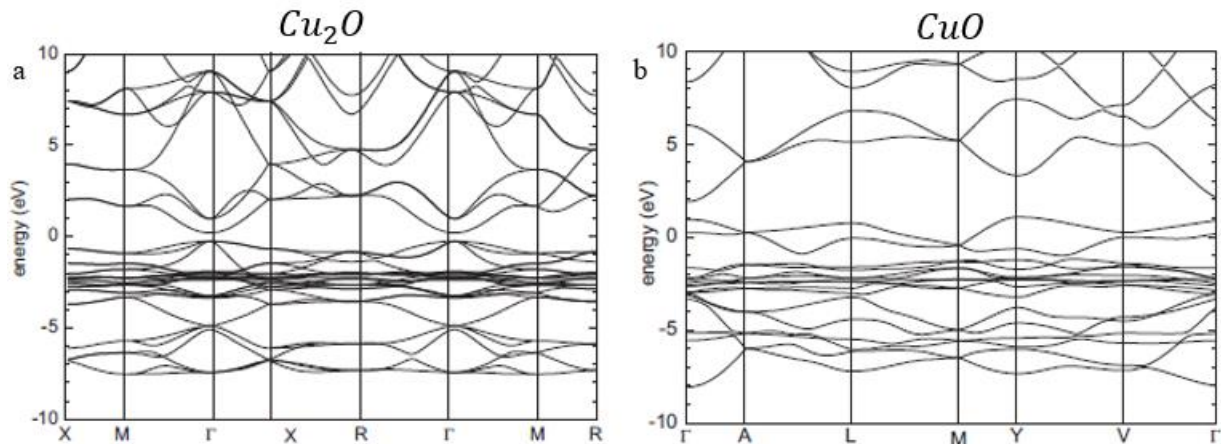
**Figure 2.6:** Band structures of (a) $Cu_2O$ and (b) CuO determined by DFT calculations [18].

The electronic structure of the Cu is strongly modified by the tetrahedral coordination with oxygen; this symmetric arrangement makes the 3d orbitals that are extended along the diagonals of the cubic structure to energetically favour the crystal field splitting as shown in Fig. 2.5 and Fig. 2.6. These DFT results however show a band gap energy level different from one another. The DFT calculations as shown in Fig. 2.5 favours $E_g$ ($Cu_2O$) $< E_g$ (CuO), while Fig. 2.6 shows that $E_g$ ($Cu_2O$) $> E_g$ (CuO). This discrepancy and related un-clarity of the true band properties, point out that conclusive research is still required.

According to ref. [105], the formation energies of both the oxygen interstitials and the copper vacancies defects are at 1.15eV and 1.14eV, respectively. Both defects introduce hole states above the valence-band maximum [106] (see Fig. 2.7).
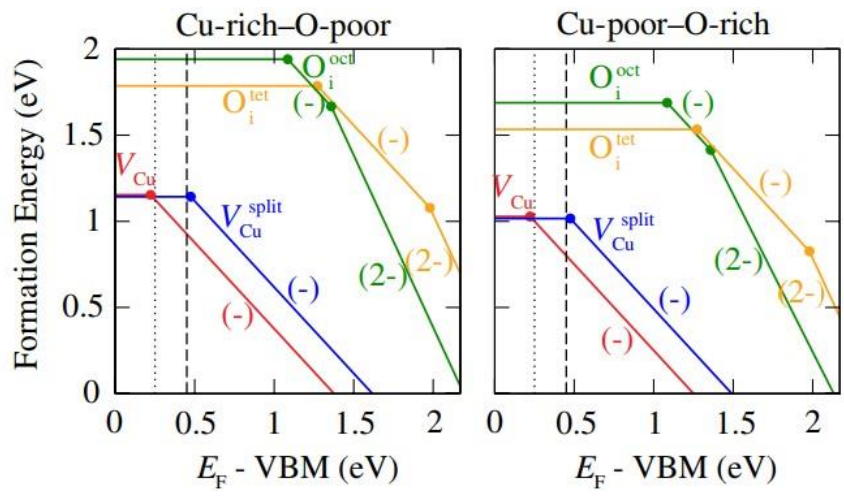
**Figure 2.7**: Formation energies for intrinsic p-type defects in $Cu_2O$ in (left) Cu-rich–O-poor conditions and (right) Cu-poor–O-rich conditions. The full dots denote the transition levels [105].

In this chapter, the description of the experimental realization of copper oxide thin films by Radio Frequency (RF)-magnetron sputtering is treated and the choice and preparation of substrates as well as the deposition of layers of $Cu_xO$ are explained.

## 3.1. RF-Magnetron sputtering for metal oxides deposition

The used  ultra-high vacuum sputtering machine is displayed in the picture in Fig 3.1.
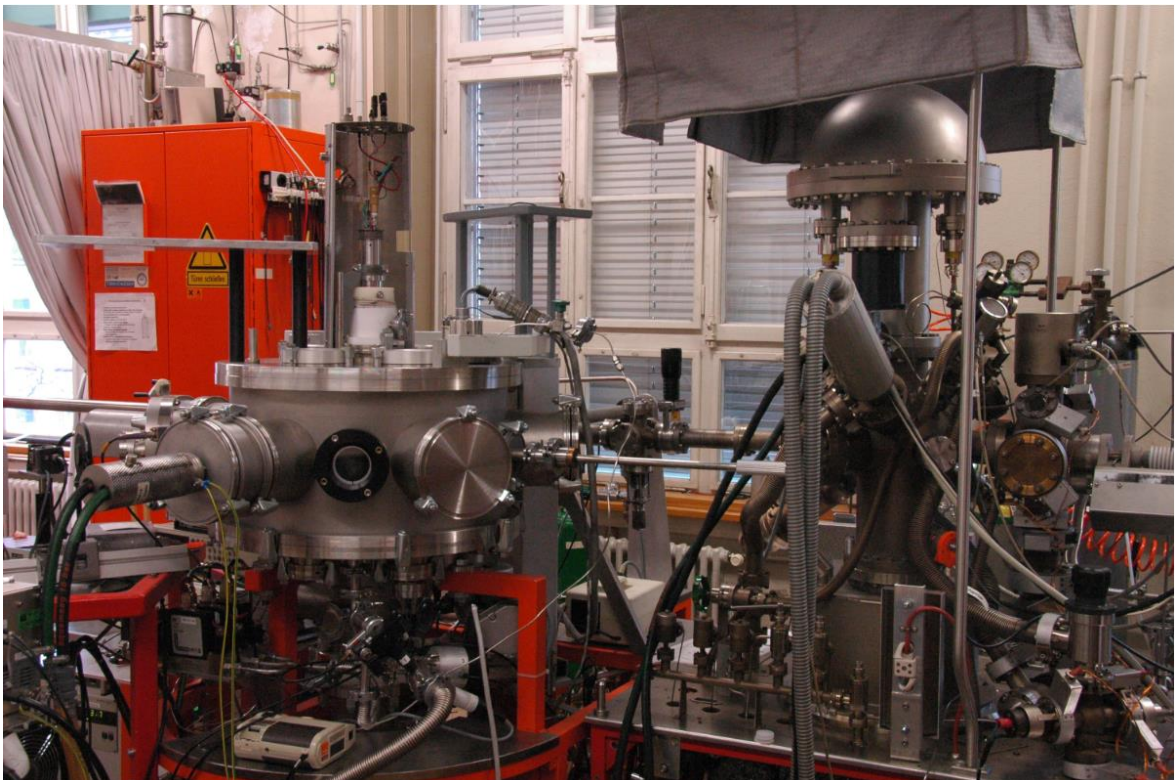


**Figure 3.1:** Sputtering chamber machine used for this work.

As mentioned in the previous chapter, RF-magnetron sputtering technique can be employed for the deposition of conducting and non-conducting materials. In our case, it was used to deposit compound semiconductor thin films of $Cu_xO$.

Fig. 3.2 displays the schematic diagram of the sputtering deposition system. The advantage of magnetron sputtering is its ability to use the low chamber pressure to maintain high deposition rate and the magnetic field to confine the electrons near the sputtering target to sustain the needed plasma. Magnetron sputtering is particularly useful when high deposition rates and low substrate temperatures are required [63] and for high melting point materials, like in the case of copper. In magnetron sputtering, there is an electric field at the sputtering target surface. The target holder serves as cathode and the substrate holder as anode. Source material (in our case Cu target) is subject to intense bombardment by energetic gas ions such as $Ar^+$. By momentum transfer, the particles ejected from the surface of the cathode, condense on the substrate to form a layer of thin film. Sputtering is normally performed at a pressure around $2x10^{-6}$ mbar. The deposition rates and properties of the films strongly depend on the sputtering conditions such as the partial pressure of the reactive gas, the sputtering pressure, the substrate temperature, and the substrate-to-target spacing. In case of RF sputtering, a high frequency generator (13.56 MHz) is connected between the electrodes and it assists the momentum transfer of the gases (Ar or N ions) to the sputter target that is needed for the sputtering deposition.

The sputtering machine used for these experiments consists of four parts: the main deposition chamber with rings for cooling and sample rotation handles for fittings, the transfer chamber, the load-lock, and the in-situ X-ray photoelectron spectroscopy (not used for this deposition process). The transfer chamber is a temporary holder of the substrates before they are moved to the various chambers of interest. The load-lock is the loading chamber. Samples are moved between the different chambers using a magnetic handle to ensure vacuum is maintained while the sample is transferred. The magnetron is water cooled and coupled to the RF source. Two pumps, the primary and the turbo pump, pump the deposition chamber. Mass flow controllers regulate the supply lines.
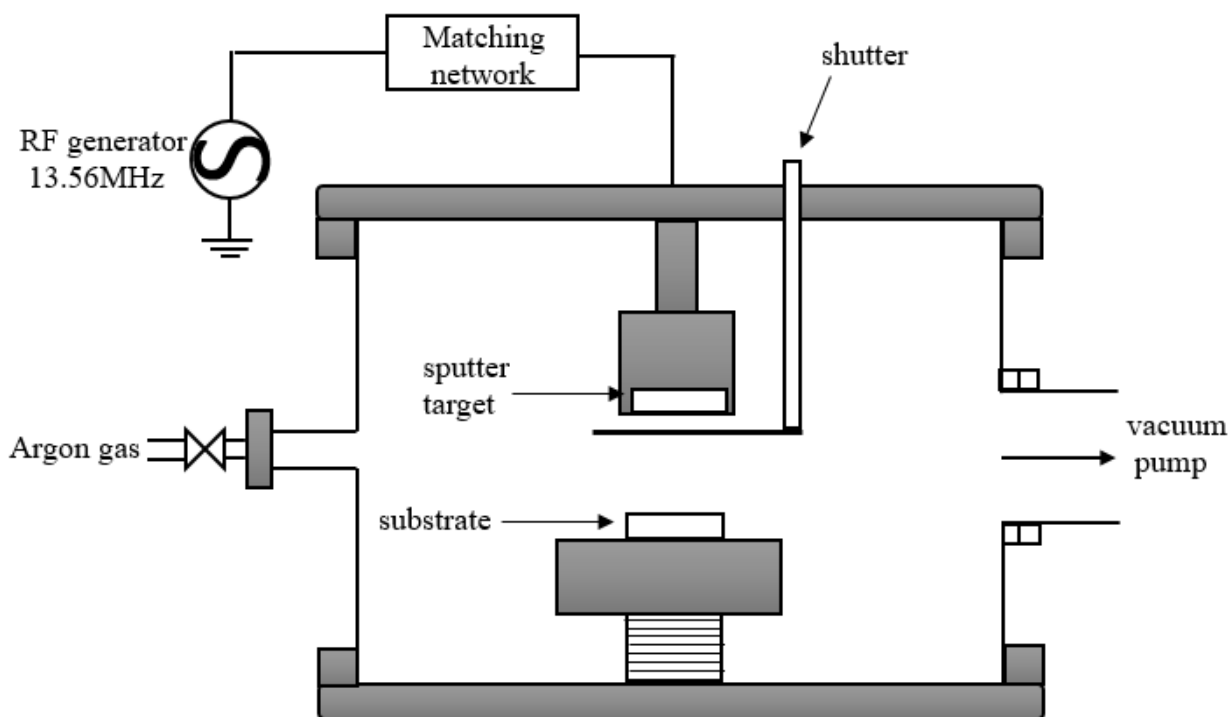
**Figure 3.2:** Schematic diagram of an RF Magnetron sputtering deposition system. Adapted from ref. [107].

## 3.2. Substrates choice and preparation

We used two common substrates utilized for the deposition of copper oxide thin films, namely <100> Silicon wafers and Fluorine-doped Tin Oxide glasses (FTO).

The most relevant properties of a substrate are its surface, chemical composition, mechanical strength, and thermal conductivity [108]. Common substrates are silicon wafers of different orientation, quartz, ceramic, mica, MgO, and coated glasses (Fluorine treated oxide and Indium treated oxide). Other reported substrates for anchoring of metal oxides are Polyethylene terephthalates (PET) foils [109]. Hence, the choice of the substrate is an integral part of any deposition process.

Cleaning and preparation of substrates is a vital and integral part of the deposition, as it helps to remove contamination, which has a decisive influence on the thin film growth and adhesion. There are different kinds of impurities on substrates, starting from the moment of

purchase, impurities in commercial distilled water produce stains on the substrates and thin layers of oxide form due to exposure to atmospheric oxygen. The storage after cleaning is as important as the substrate cleaning itself, therefore the petri dishes and other storage devices must have tight lids for coverage. To ensure a clean substrate, for this work the petri dishes were washed thoroughly and dried. The flow chart in Fig. 3.3 shows the cleaning steps followed before deposition. First, the sample was degreased with ethanol. Then, it was rinsed in distilled water, followed by sonication for 5 minutes in acetone, and drying under nitrogen flux. The clean substrates were then moved into the storage device using tweezers. For the FTO coated glass substrates, the multimeter (volt-ohm-milliamp-meter) was used to check the conducting surface before storage to avoid deposition on the wrong side of the substrates.
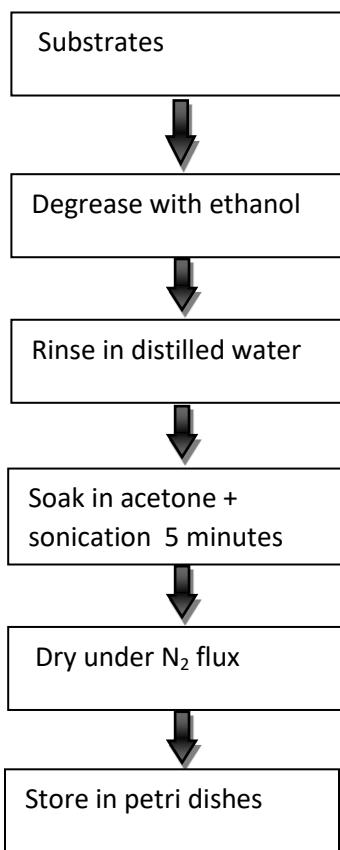


**Figure 3.3:** Flow chart explaining substrates cleaning steps.

**3.3. Deposition of layers**

The art of thin film deposition, purpose and merits were discussed earlier in Chapter 2, Sec. 2.4. This section is devoted to the description and explanation of the deposition of $Cu_xO$ layers as related to this project. The deposition of thin film layers was performed on both <100> Si or FTO coated glass substrates that were pre-cleaned. The deposition onto FTO glass substrates is required for using $Cu_xO$ for photovoltaic applications. Furthermore, it allowed us to perform absorption measurements on the grown films. This section describes the exact deposition parameters employed in this work.

The deposition of copper oxide films was performed in a high vacuum chamber pumped to a base pressure of about $2\times10^{-6}$ mbar. Copper oxide films were grown onto pre-cleaned (see Section 3.2) silicon wafers and FTO coated glass substrates, which were loaded simultaneously.

The copper target (99.9% purity, oxygen-free, high thermal conductivity) had a diameter of 2 cm. Argon (99.9999%) and oxygen (99.9995%), introduced through a mass flow controller, were used as sputter gas with the flow rate being fixed at 6.0 (Ar): 4.0 ($O_2$) sccm and 6.6 (Ar): 2.5 ($O_2$) sccm, for oxygen partial pressures of 23% and 15%, respectively. The estimated target-to-substrate distance was 7 cm, and the deposition process was carried out at room temperature at fixed RF electrical power of 100 W applied to the target. We used three sets of parameters. The very first deposition was performed with a flow rate of 8.3 ($O_2$): 1.7 (Ar), which yielded no films at all. The two other sets of parameters resulted in layer deposition: one deposition was performed at a low oxygen partial pressure (15%) and one at a high partial pressure (23%). See table 3.1 for the description of the parameters of the two depositions. The deposition rate, which translates to the film thickness for a fixed deposition time, was measured via the micro quartz balance connected to the sputtering machine.

Since the very first deposition did not produce any film, we now focus our attention to the second and third deposition at 23% oxygen partial pressure. Despite monitoring and keeping the same parameters (with the exception of a slight variation in deposition time to correct for the different growth rate measured in the quartz microbalance), we observed differences in the film thicknesses. From this variation, we concluded that reproducible growth of copper oxides is a challenging task. Bearing in mind these challenges, we changed our approach for the fourth and fifth depositions by having both the silicon and FTO glass substrates on the same substrate

holder for sputtering at the same time. In this way, we could ensure that the two different substrates were grown using exactly the same deposition parameters.

While for the second to fourth deposition we used a 23% oxygen partial pressure, for the fifth deposition we reduced the oxygen to 15% partial pressure.

When comparing to literature [3, 4, 77, 98], multiple sources indicate that there is no easy route for obtaining a single phase of the three oxides, confirming our finding that deposition of copper oxide is very sensitive to precise deposition parameters. This difficulty in synthesis represents a major drawback for the application of copper oxides. Therefore, in this work we will present another path towards reliable and reproducible production of copper oxide films through post-deposition annealing.

| Deposition at low oxygen ratio | Deposition at high oxygen ratio |
|---|---|
| Excitation: RF = 13.56 MHz  Power = 100 W | Excitation: RF = 13.56 MHz  Power = 100 W |
| Partial pressure of $O_2$ = 1.7x10$^{-3}$ mbar → 15% | Partial pressure of $O_2$ = 2.6x10$^{-3}$ mbar → 23% |
| Partial pressure of Ar = 9.6x10$^{-3}$ mbar → 85% | Partial pressure of Ar = 8.8x10$^{-3}$ mbar → 77% |
| Total pressure = 1.09x10$^{-2}$ mbar | Total pressure = 1.09x10$^{-2}$ mbar |
| Deposition time: 130 s | Deposition time: 130 s |

**Table 3.1**: Deposition parameters for the two series of thin films in the RF-magnetron sputtering machine

To ensure that the post-growth annealed samples were all having the same original properties before annealing, namely that they were all obtained with the same deposition parameters, the samples were cleaved into pieces and then each piece was annealed at a different temperature. Si samples were each cleaved into five pieces, while the FTO samples were cleaved into four. This resulted in a total of 20 silicon samples (15 grown with 23% oxygen and 5 grown with 15% oxygen) and 8 FTO samples (4 with 23% oxygen and 4 with 15%).

## 3.4. Annealing of metal oxides thin films

Annealing is a common heating treatment leading to the modification of film properties. It is important to consider the melting temperature for both substrates and films before the commencement of annealing processes. Annealing can be in-situ or post deposition.

The post deposition annealing of MO thin films can cause oxidation, activate grains growth and alter the film's stoichiometry (i.e. microstructure and phases). The annealing of a solid-state crystalline material at sufficiently high temperature can enable the Ostwald ripening i.e. when the reaction temperature increases the grains can merge to form bigger grains. Annealing could increase film thickness in some polycrystalline materials [110].

In this work, annealing was performed post deposition in a tabletop programmable digital compact rapid thermal annealing (RTA) oven system called AO 600. The oven is connected to a gas pump that is able to maintain a pressure of about 5 mbar. The dimension of the direct current driven heater plate is 15 mm x 30 mm and the plate is made of $Al_2O_3$ thin film for resistive heating. The temperature measurement occurs via a platinum resistive thermometer. The oven has a round transparent glass lid that gives an open view to the sample holder, enabling observation of the sample during the annealing process. The temperature stability is about 1 K, the heat-up speed for vacuum annealing is about 50 K/s, while the cooling-down speed for gas flow annealing chamber is approximately 12 K/s.  See Fig. 3.4 for a picture of the oven with the $Cu_xO$ sample.
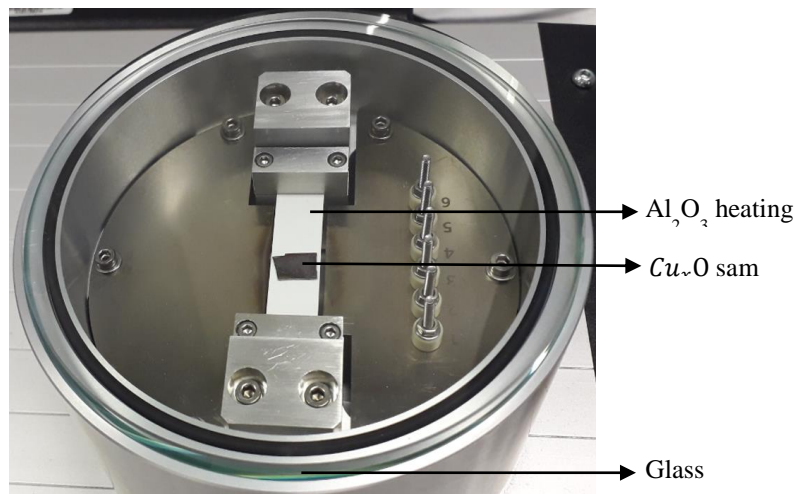


**Figure 3.4:** Annealing oven containing a $Cu_xO$ sample deposited on a Si wafer

The samples deposited on Si and cleaved after deposition were annealed in vacuum at the annealing temperatures of 250, 350, 450, 500 and 550 $^{o}$C; the ramping time was 300 s, and the samples' annealing time was one hour each.

Heat treatment was also conducted on the thin films deposited unto FTO coated glass substrates at temperatures of 250, 350, 450 and 550 °C. In the course of the annealing process, we observed that the thin films deposited on FTO-coated substrates deposited at the higher value of 23% $O_2$ partial pressure changed color from brownish to yellowish when annealed at the temperature of 350°C and 450 °C. This observation has likely to do with the reduction process of CuO to $Cu_2O$, as the dark color by visual inspection suggests the presence of oxidized CuO. The properties of the obtained thin films on Si and glass are discussed in Chapter 5.

.

# Chapter

# 4

This chapter presents an introduction to all the techniques and the equipment used in the characterization of the investigated copper oxides thin films. The surface morphologies of the grown thin films were imaged by scanning electron microscopy (SEM). The structural investigation was performed by means of Raman spectroscopy and X-ray diffraction (XRD). The Energy Dispersive X-ray spectroscopy (EDX) enabled the elemental composition analysis. The topography and contact potential difference (CPD) characterization was done by atomic force microscopy (AFM) and Kelvin Probe Force Microscopy (KPFM), respectively. We performed the absorption measurements using a UV-VIS spectrometer.

## 4.1. Scanning Electron Microscopy

The SEM scans a focused electron beam over a sample's top surface to form images of it. The electrons and the electromagnetic lens sources are from tungsten filament lamps that are usually placed at the column top. The electrons are emitted after the application of thermal energy to the source and the electrons are in fast motion towards the positively charged anode. The electron beam is stirred by condenser lenses in order to scan the sample' surface. The beam of electrons activates the emission of primary scattered electrons (at high energy levels) and of secondary electrons (at low energy levels) from the sample's surface. A special detector apparatus collects the secondary electrons. When they reach and enter the detector, they strike a scintillator (a luminescence material that fluoresces when reached by a charged particle or high-energy photon). This emits flashes of light, which are converted into an electric current by a photomultiplier, sending a signal to the cathode ray tube. The latter produces an image. Figure 4.1 shows the schematic diagram of an SEM. The samples must be conducting or otherwise coated to become conductive.
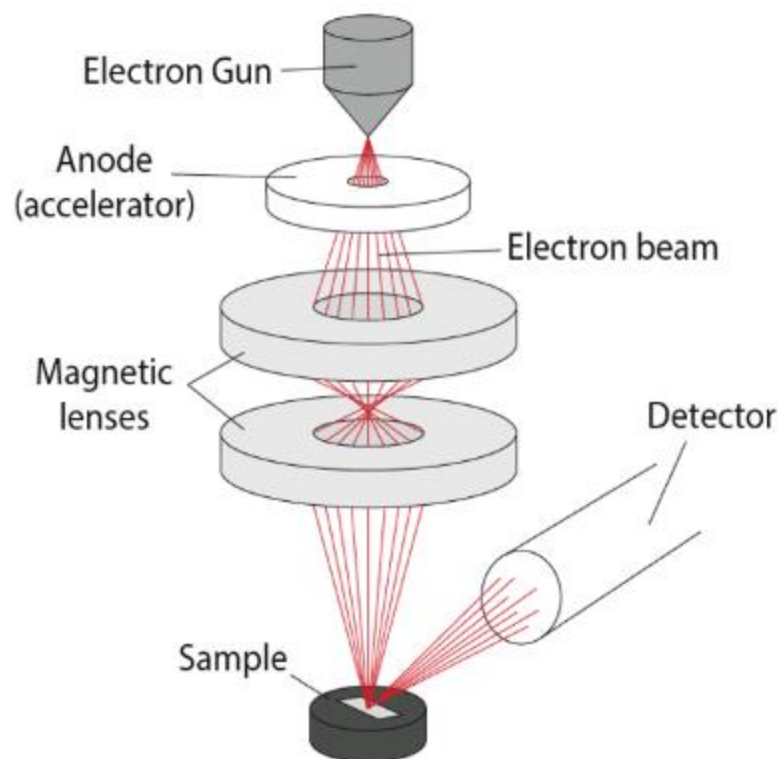
**Figure 4.1:** Schematic of a scanning electron microscope (online) [111].

SEM measurements were performed with a "Zeiss Supra 35" SEM. The general settings were an acceleration voltage of 5.00 kV and a working distance of about 5 mm for top view imaging, while an acceleration voltage up to 15.00kV was used for layer thickness estimation (i.e. cross-sectional imaging). The large working distance was a precautionary measure to prevent contact of the sample with the highly damageable SEM-cone (the gun). The silicon samples were mounted with double-sided carbon-tape disks onto the aluminum pin-stub holders, which were screwed onto the sample holder base. The cross-section images were recorded at 90° tilt angle to orientate the side of the sample towards the electron-beam. Prior cross-sectional imaging, after deposition, the sample was prepared cleaving it in order to expose a fresh interface between the $Cu_2O$ layer and the substrate underneath. We experienced some charging due to the semiconducting nature of the film. For the films deposited on FTO coated glass, carbon tape was not used, to avoid excessive charging; instead, we clamped the glass samples creating a conductive contact directly from the top layer straight onto the sample holder.

We obtained the thickness of the deposited films on both Si and FTO coated glass samples using cross-section images taken by SEM. Figure 4.2 displays the cross sectional SEM images of $Cu_2O$ thin films deposited on Si wafer. For the thickness of the FTO-coated glass substrates, a cross section of a reference substrate without a copper oxide layer was recorded. Afterwards, we subtracted the reference sample thickness from the deposited films thicknesses, since the copper oxide layer could not always be precisely identified with respect to the FTO layer. The images of the thin films' surfaces will be shown and discussed in Chapter 5.
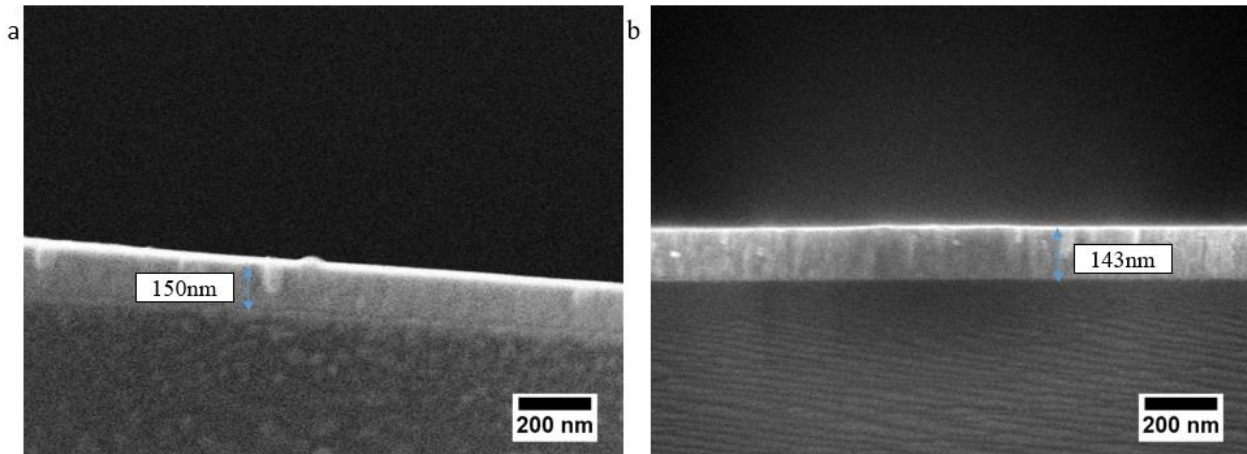


**Figure 4.2:** Cross sections of the films deposited on Si wafers (a) at 15% oxygen partial pressure with 150 nm thickness and (b) at 23% oxygen partial pressure with 143 nm thickness. The blue arrow indicates the height of the measured thickness. The scale bars are 200nm.

## 4.2. Energy Dispersive X-ray Spectroscopy

The control of composition is important in any compound film or alloy as the properties of semiconductor compounds are sensitive to changes in composition.

For performing the qualitative analysis to determine the composition of the thin films sputtered unto silicon substrate, we used a REM-FEI Nova Nano SEM 230 with an EDX detector "Octane Elite" and the software "Genesis" from the company EDAX. Fig 4.3 shows the complete setup. The acceleration voltage was 10 kV and working distance 7.0 mm and we used a secondary electron detector and chose a magnification of 30 000 X. The samples deposited on Si wafers substrates were loaded into the chamber as described in sec. 4.1 (with the same system as used for the SEM).

The process giving rise to EDX can be described as follows: The electron beam inside the scanning electron microscope bombards the loaded sample. The bombarding electrons collide with the electrons in the core orbitals of the investigated specimen, knocking some of them off in the process. The higher-energy electrons from the outer shells fills the vacancy positions left behind by inner shell electrons. To be able to do so, however, the transition electrons must give away some of their energy by emitting an X-ray. The amount of energy released by the transition electrons depends on the difference in energy between the initial (higher energy outer shell) and final (lower energy core shell) shell. As a result, the atom of every element releases X-rays with unique amounts of energy during the transition process. Thus, by measuring the amounts of energy present in the X-rays released by the sample during electron beam bombardment, the identity of the atom from where the X-rays were emitted can be established. The output of an EDX analysis is an EDX spectrum, as the one shown in Fig. 4.4. The EDX spectrum displays peaks corresponding to the energy levels. Each of these peaks is unique to an atom and, therefore, can be associated to a single element. The intensity of a peak in a spectrum is proportional to the abundance of the element in the sample. More EDX spectra for both Si and FTO of the deposited thin films will be displayed and discussed in Chapter 5.
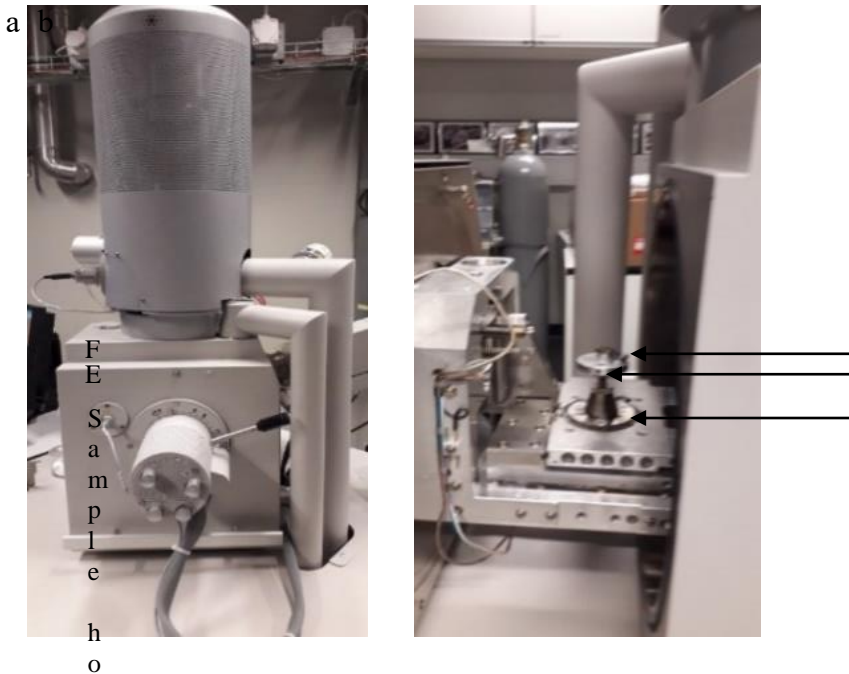


**Figure 4.3:** REM-FEI Nova Nano SEM 230 at the Swiss Nano Imaging Lab, University of Basel.
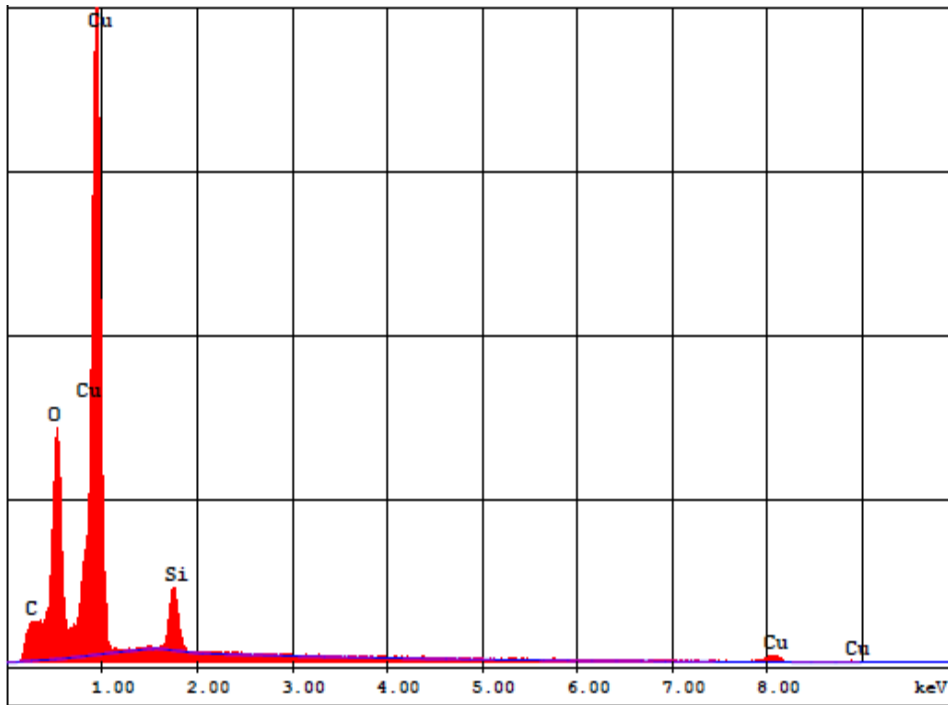
**Figure 4.4:** EDX spectra of a $Cu_2O$ thin film displaying the carbon, oxygen, copper and silicon contribution. The abscissa is the ionization energy (keV) while the ordinate axis gives the counts per seconds per electron volts (cps/eV).

## 4.3. Atomic Force Microscopy and Kelvin Probe Force Microscopy

In 1986, Binnig et al. [112] introduced the scientific world to their new invention, the AFM. The AFM technique is a surface probing microscope that measures the topography of a sample surface with nanometric resolution [113]. The AFM probes are called cantilevers: a cantilever is a beam with a sharp tip on its lower side which performs the actual measurement. A sensitive force sensor measures the deflection upon interaction with a sample's surface. The deflection is employed to measure the surface topography. A laser focused onto the back of the cantilever is used to quantify the cantilever deflection as its reflection changes position on a position sensitive detector (PSD). There are different measurement modes, such as contact-mode and non-contact mode. Based on the measurement mode, the deflection signal is processed and fed into a control-loop: there is a piezo that adjusts the z- position of this functional cantilever and enables the measurement of the surface topography. An outline of an AFM setup is displayed in Fig. 4.5.
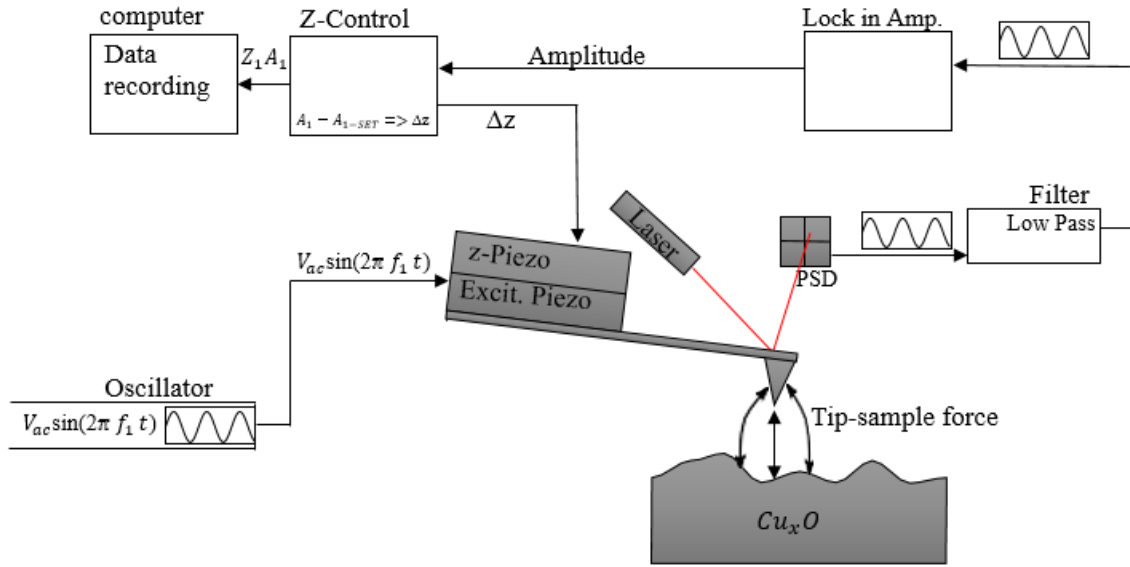
**Figure 4.5:** Outline of the basic instrumentation of an AFM. Adapted from ref. [114].

KPFM is a surface probing microscopy technique based on AFM in non-contact mode. In 1898, Lord Kelvin developed and demonstrated the first Kelvin probe. He used two sets of parallel plates capacitors, where the first plate was a known metal and the second plate was the sample to be identified. In a KPFM setup, the two materials, which have work functions $\phi_1$ and $\phi_2$, are the tip and the sample, respectively, and are brought into close contact with each other. The two plates are connected electrically through a back electrode and the electrons flow from the metal with lower Fermi energy to the one having higher Fermi energy until there is the alignment of the Fermi levels. Lord Kelvin measured the variation in the current in between the two metallic plates by applying an AC voltage [115]. The contact potential difference $V_{CPD}$ is the difference in the work function $\Phi$ of two metals [116]:

$$V_{CPD} = \frac{\Phi_1 - \Phi_2}{e} \; . \tag{4.1}$$

Concisely, KPFM is described as the mechanical response of a cantilever to the voltage difference between a cantilever tip and a sample.
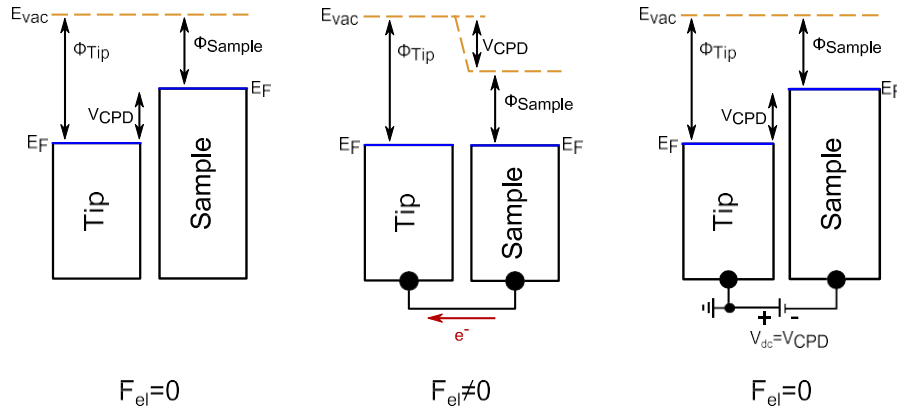
**Figure 4.6:** Contact potential difference between two plates, two separate metallic samples with equal vacuum energy levels ($E_{vac}$) but different Fermi energy ($E_F$) levels (left). When tip and sample are connected, the Fermi energies align by an electron transfer from the lower Fermi energy levels to the higher Fermi energy level, thus, an electrostatic force evolves (center). By applying a dc-voltage, the vacuum levels re-align and there is a compensation of the electric field, hence the work function $\Phi$ can be determined if $V_{dc} = V_{CPD}$, (right) [114].

In this thesis, both AFM and KPFM measurements were performed with the same "Flex-AFM" microscope. The measurements were carried out inside a glove box (labmaster 130, mBraun) under a dry nitrogen atmosphere ($< 0.1\,\text{ppm}\ H_2O$ and $O_2$) with a commercial microscope (FlexAFM, Nanosurf) in standard tapping mode at the first cantilever resonance. We conducted the electrical analysis via KPFM employing the use of the single pass mode to capture both the topography and the contact potential difference (CPD) simultaneously with amplitude modulation [116, 117]. An external lock-in amplifier (HF2, Zurich Instruments) was employed to excite, detect and compensate the electrostatic forces at the second resonance of the cantilever [118]. The data acquisition was performed using a PtIr coated cantilever (PPP-NCLPT, Nanosensors).

## 4.4. X-ray Diffraction

X-ray diffraction is a versatile, non-destructive technique that reveals detailed information about crystal phase, crystal structure, defects, crystallite sizes, crystal orientation, and strain from X-ray diffraction patterns. The phase identification is one of the routine applications of the XRD, and it involves comparing the measured peak intensities from the diffraction spectra with those for known standards given in literature [119].

In this technique, a sample is irradiated with a collimated beam of X-rays (with wavelengths between 0.5 and 2.0 Å) and the scattered X-rays are detected. The sample's orientation with respect to the detector, and the specific crystal structure of the sample, are important for a good XRD pattern to be recorded. Such a pattern consists of peaks in the scattered X-ray intensity plotted as a function of scattering angle. The peaks are due to the constructive interference of the scattered X-rays.
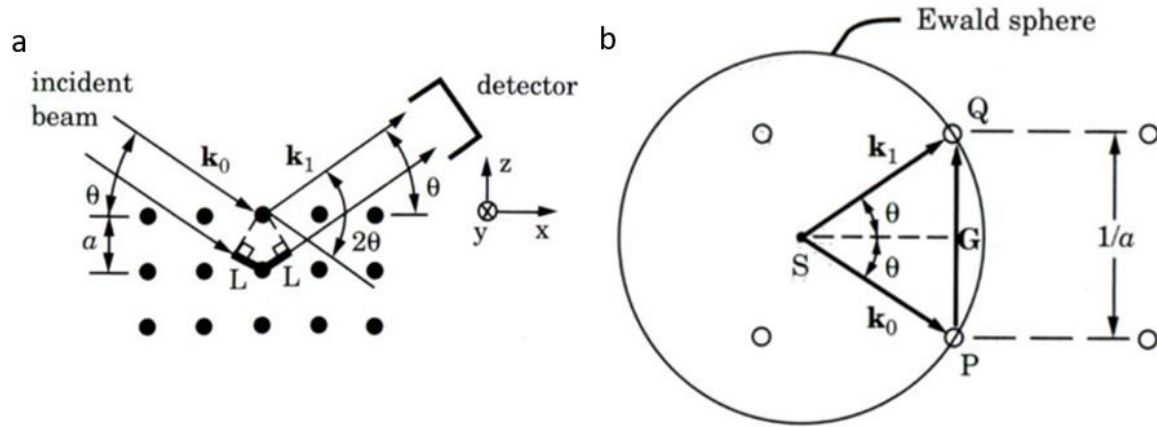


**Figure 4.7:** Geometry of diffraction from a stack of x-y atomic planes: (a) is real space construction and (b) is the reciprocal space construction. Adapted from ref. [63].

In a typical XRD experiment, the incident beam penetrates the lattice and scatters from each of the atoms in the 3D array (see Fig. 4.7a). Diffraction can occur only for specific angles between the lattice planes and the X-ray beam, providing constructive interference, according to Bragg's law [120].

$$2d\sin\theta = n\lambda .$$ 
(4.2)

where $\lambda$ is the wavelength of the beam (in our case 1.5418 Å with a copper target being used as a source of CuKα radiation), $d$ is the interplanar distance and $\theta$ is half of the diffraction angle ($2\theta$).

The grazing incidence can be employed to examine the crystallography of a material's top surface within a few nanometers depth. The incident and reflected beams are almost parallel to it, hence the lattice constant $a$ of the planes perpendicular to the film surface is measured [121].

We recorded the XRD patterns using a SIEMENS D5000 instrument with Cu Kα radiation (40 kV and 30 mA) at a grazing incidence of 5°. A graphite secondary monochromator (no filter) was used and a width of 1° for the primary and secondary divergence slits is applied. All XRD patterns were acquired with scan steps of 0.02° and with 8 s acquisition time, within scanning Bragg angle of $2\theta$ from 20° to 72°. The $Cu_2O$ peaks positions were taken from the Inorganic Crystal Structure Database (ICSD pattern 01-077-0199), while the CuO peak positions came from ICSD pattern 00-045-0937 and ICSD pattern 00-048-1548.

## 4.5. Raman spectroscopy

### 4.5.1 Fundamentals of Raman spectroscopy

Raman spectroscopy is a non-destructive characterization technique for the three states of matter (liquid, gas and solid materials) and it cuts across almost all the spheres of science. For example, it can be used to investigate the distribution of active compounds in drugs, it can identify pigments, artistic identity, and eras in medieval paintings, and, in semiconductor research, it can unlock the crystal lattice structures. Raman spectroscopy is based on inelastic light scattering and it allows probing the vibrational properties of materials. In particular, Raman spectroscopy allows the investigation of phonons. A phonon is the quantum-mechanical correspondent of the classical normal mode of vibration, which is an elementary vibrational motion in which a periodic lattice of atoms oscillates with the same frequency.

In 1928, C.V. Raman and his student K.S. Krishnan first observed the effect of Raman scattering on organic liquids and, independently, G. Landsberg and L. Mandelstam observed the same effect in their investigations of inorganic crystals [122, 123]. C.V. Raman won the Nobel Prize in Physics in 1930 for the discovery of the Raman effect, using sunlight as excitation source. Nowadays, Raman signal is commonly excited with lasers, which are monochromatic and intense light sources, which is beneficial to observe the usually weak Raman signals. In the Raman effect, the laser light interacts with molecular vibrations, phonons or other excitations in the system, resulting in the emitted light having an energy shifted up or down with respect to the laser energy. The change in energy (called Raman shift) gives information about the vibrational modes in the system. Typically, each peak in the Raman spectrum brings information on a specific vibrational mode, i.e specific chemical bonds in molecules or crystal lattices. Raman

spectroscopy allows investigating the vibrational properties of materials and can reveal information about crystals, such as a materials' crystal composition, electronic band structure, and crystal structures, all through the investigations of the materials' phonons. The Raman effect is not restricted to the change in energy of the electromagnetic radiation that is inelastically scattered by the materials through phonons, as Raman effect extends to scattering by quasi-particles like plasmons, polaritons, and electronic and spin excitations.

Spontaneous Raman scattering can be represented in a simple sketch as the one in Fig. 4.8, showing the vibrational energy states, the virtual energy states, the laser excitation energy $\hbar\omega_i$ (see vertical black arrows), and the energy, $\hbar\omega_s$, of scattered light (vertical purple, blue and red arrows). There are three types of light scattering processes: the elastic Rayleigh scattering (where the frequency of the scattered light and incident light are the same, i.e $\hbar\omega_s=\hbar\omega_i$) and the two inelastic scattering known as Stokes and anti-Stokes Raman processes [124]. For any given process or system the laws of energy and momentum conservation are always guiding. Inelastic light scattering processes involve two fundamental steps, that are absorption of a photon with energy $\hbar\omega_i$ and wave vector $\vec{k}_i$, and emission of a scattered photon with energy $\hbar\omega_s$ and wave vector $\vec{k}_s$. This happens via the creation of a phonon in the system (Stokes process), or via the destruction of a phonon (anti-Stokes). Thus, the scattered light frequency is expressed by the equation:

$$\omega_s = \omega_i \pm \omega_q, \tag{4.3}$$

in which $\omega_q$ is the frequency of the phonon, having momentum $\hbar\vec{q}$, and the sign + describes the Stokes process while the – describes the anti-Stokes (see also the energies represented by the blue and red lines in the diagram, respectively).

For the conservation of momentum, the system gives out a photon with energy $\hbar\omega_s$ and the wave vector $\vec{k}_s$, described by:

$$\vec{k}_s = \vec{k}_i \pm \vec{q}. \tag{4.4}$$

The typical energy of a phonon is in the range of IR light and it can also be probed directly by IR spectroscopy (see green arrow in Fig 4.8).
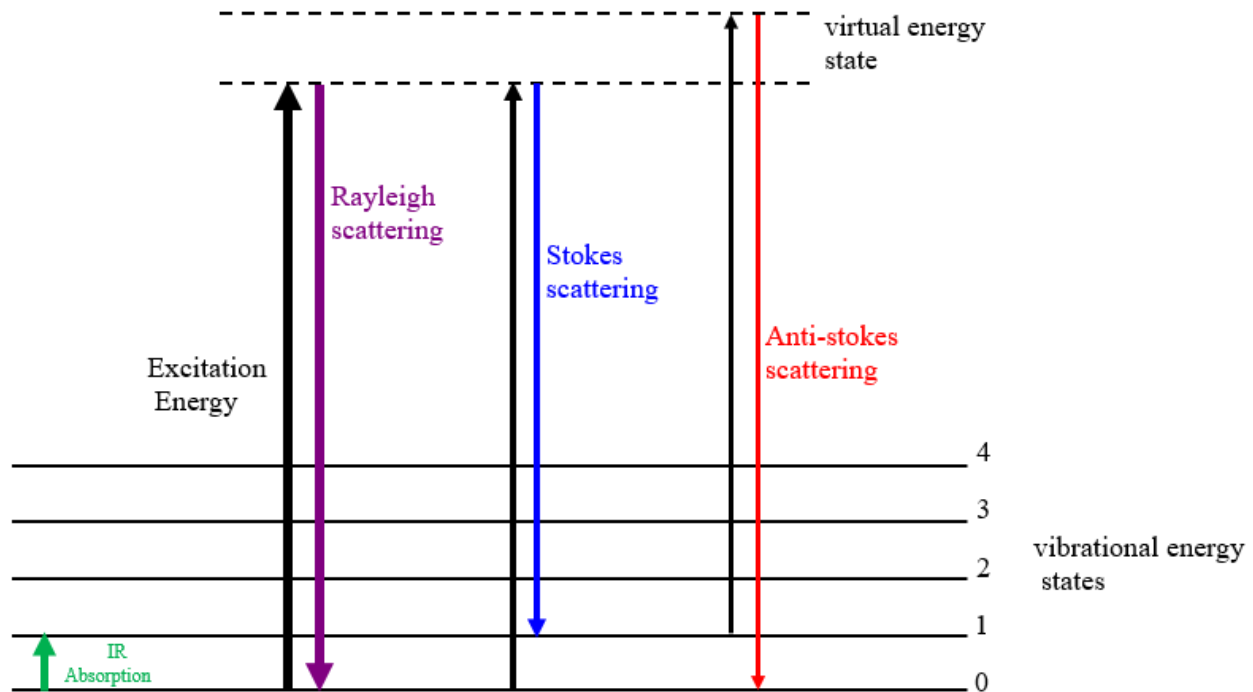
**Figure 4.8:** Schematics displaying the vibrational energy states (0-4) of a system, the infrared absorption in green (the arrow corresponds to the typical energy of a phonon), the excitation energy (usually provided from a laser) represented by vertical black arrows, the Rayleigh scattered photon energy in purple color, the Stokes scattered photon energy in blue, the anti-Stokes scattered photon energy in red, and the virtual states as dashed lines.

As depicted in Fig. 4.8, Stokes processes occur due to excitation of the atoms from ground state to the excited state, while anti-Stokes processes occur due to transitions from an excited state to the ground state. Therefore, the intensity of Stokes lines is proportional to the population of the ground state and that of anti-Stokes lines is proportional to the population of the excited state. Since, at a given finite temperature, the population of the ground state is larger than that of the excited state, the intensity of Stokes lines is higher.

### 4.5.2 Phonon modes of copper oxides

In Chapter 2 we have described the crystal structure of the two stable phases of copper oxide in Fig 2.3 and their corresponding Brillouin Zones in Fig. 2.4. The zone center identification of the phonon modes of CuO is:

$$\Gamma = 4\,A_u + 5\,B_u + A_g + 2\,B_g, \qquad\qquad [4.5]$$

namely, 12 phonon modes, as there are 4 atoms per primitive unit cell [125, 126]; 3 of the 12 phonon modes are Raman active. The other oxide phase, which is the paramelaconite ($Cu_4O_3$), has been reported to have a total of 14 atoms in its primitive cell, giving a total of 42 phonons [18, 126], that we don't list here because it is beyond the scope of this work. The cubic structure of the $Cu_2O$ crystal contains 6 atoms per primitive unit cell, i.e. 18 phonon branches. The zone center identification is the following:

$$\Gamma = A_{2u} + E_u + 3T_{1u} + T_{2u} + T_{2g}, \qquad\qquad [4.6]$$

The modes with A, E and T symmetry are one, two and three fold degenerate, respectively, for the phonon vibration. The 3 acoustic phonon modes have $T_{1u}$ symmetry character, $T_{2g}$ is the only Raman active mode in a perfect cubic crystal, the 2 IR active modes have $T_{2u}$ symmetry character, and all the rest are optically silent. Overall, in $Cu_2O$ there are only 8 optical phonons at the $\Gamma$ point, namely, $A_{2u}$, $E_u$, $T_{2g}$, $2T_{1u}(LO)$, $2T_{1u}(TO)$ and $T_{2u}$. These six types of vibrations are represented in Fig. 4.9 [127, 128, 129].
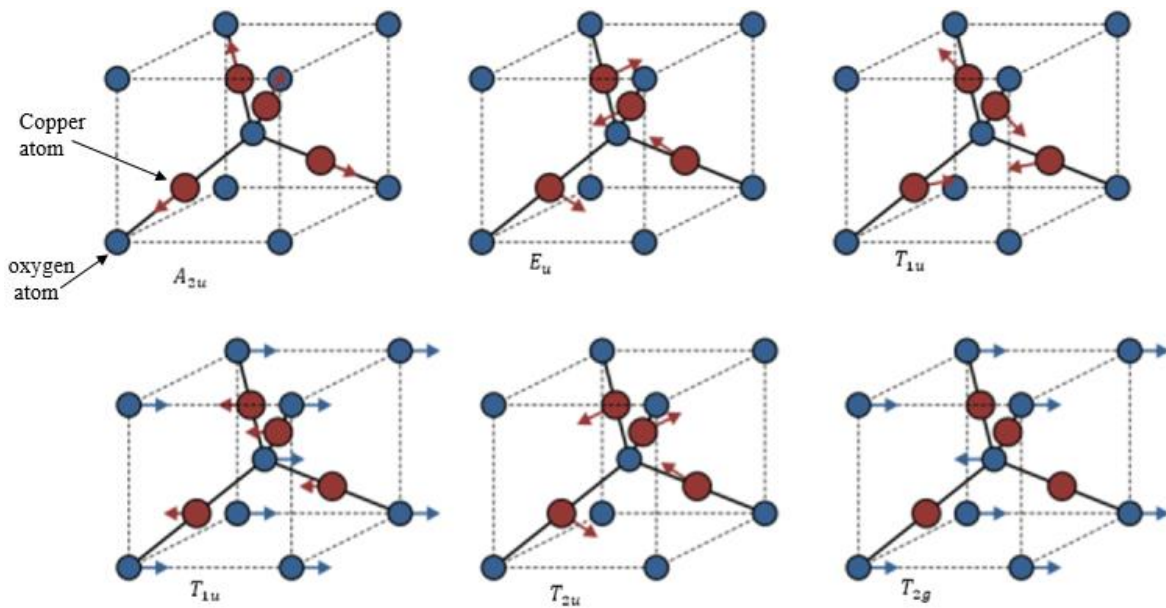


**Figure 4.9:** $Cu_2O$ eigenvectors (red and blue arrows) of the six optical vibrations in $Cu_2O$. The red ball is representing copper atom and the blue ball the oxygen atom. Adapted from ref. [129].

In Chapter 5, we observe some phonon modes of CuO and some of $Cu_2O$. In general, there is a difference between the names used for the phonon identification in this chapter and in literature. Above we have labelled the phonon modes according to the Mulliken notation, while in the literature (and in chapter 5) for some modes it is used the Mulliken notation, for some others the BSW (L. P. Bouckaert, R. Smoluchowski, and E. Wigner) notation. The correspondence between the Mulliken notation given above and the BSW notation is summarized in the table below, along with the calculated and experimental frequencies of the main phon modes of $Cu_2O$.

| Symmetry | Calculated frequencies (cm$^{-1}$) | Experimental values (cm$^{-1}$) |
|---|---|---|
| $T_{2u}/ \ \Gamma_{25}$ | 60-98.6 | 86-88 |
| $E_{u}/ \Gamma_{12}^{-}$ | 72-110 | 109-110 |
| $T_{1u}/ \Gamma_{15}^{-(1)}$ | 144-143 (TO)-159 (LO) | 146-153 |
| $A_{2u}/\Gamma_{2}^{-}$ | 338-307 | 305 |
| $T_{2g}/ \Gamma_{25}^{-}$ | 503-549 | 515 |
| $T_{1u}/\Gamma_{15}^{-(2)}$ | 616-608(TO)-639 (LO) | 638-665 |

**Table 4.1:** Symmetry (with Mulliken/BSW notation), calculated and experimental frequencies of the vibrational modes of $Cu_2O$ [94].

### 4.5.3 Experimental setup

In this work, we performed Raman spectroscopy on our samples by using a Witec Raman Alpha 300 setup consisting of an optical microscope with a coupling tower connected to a spectrometer and lasers via optical fibers. The microscope offers both bright and dark fields imaging. In addition, a motorized xy stage on which the samples are mounted enables sample scanning. Laser light is coupled to the microscope tower with a single-mode optical fiber and its power can be manually tuned between 0.00mW to 10.00mW by using a filter. The monochromatic laser is focused onto the sample with an objective. In a backscattering geometry, the objective also allows the collection of the scattered light and sends it upward as a parallel beam. A notch filter blocks the Rayleigh (elastically) scattered light before entering into the spectrometer. A half-wave plate placed on the microscope tower allows turning the polarization of the excitation laser and of the detected signal. The Raman shifted light passes to the top of the tower, where it is focused onto the end of a standard optical fiber, acting as the second focal

point for this confocal setup. The setup has a visible-near infrared spectrometer with two gratings available (600 and 1800 g/mm) and with a Peltier cooled charge coupled device (CCD) for acquiring signals. The complete setup and its schematic are displayed in Fig. 4.10 a and b, respectively.
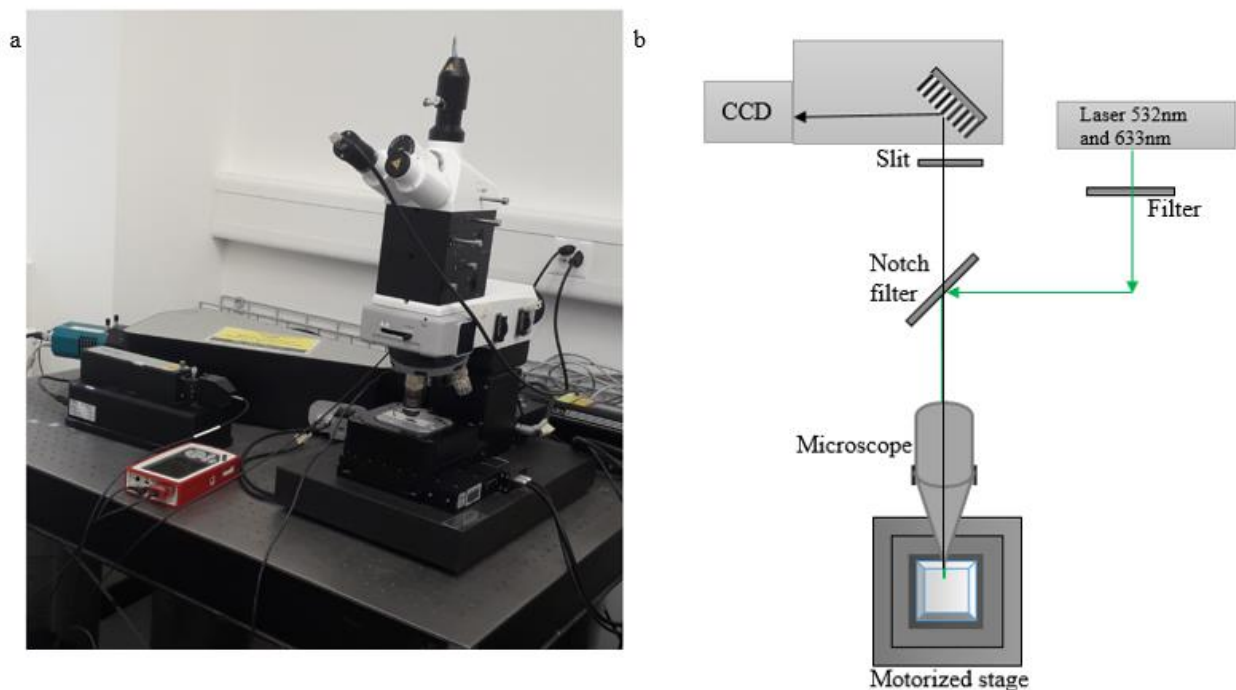


**Figure 4.10:** (a) Picture of the Witec Raman alpha300 setup and (b) schematics of the components of the Raman setup. Panel b is adapted from [130].

For this thesis, the sample was placed on a pre-cleaned glass slide and mounted on the top of the motorized stage. The Stokes Raman spectra were acquired at room temperature using a 532 nm excitation laser. The power density (measured after the microscope objective) was fixed to $250\,kW/cm^2$, which allowed to avoid laser-induced sample modification/damage. The laser beam was focused on the sample surface using a 100X objective with 0.9 numerical aperture (NA), resulting in a spot size of about 0.6 µm. The scattered light was collected in backscattering geometry and analysed using a spectrometer with a 600 grooves/mm grating. Additionally, to check the homogeneity of the deposited thin films, we have performed spatially resolved Raman measurements on several samples, see details in Chapter 5, Sec. 5.1 and Fig 5.8. In all the measurements, the polarization of the detected light was parallel to the one of the laser light.

## 4.6. Absorption spectroscopy

Generally, the interaction of light with matter results into reflection, absorption and scattering, where the scattering can be elastic as seen in Mie and Rayleigh theories and the inelastic, which can be measured in Brillouin and Raman studies.
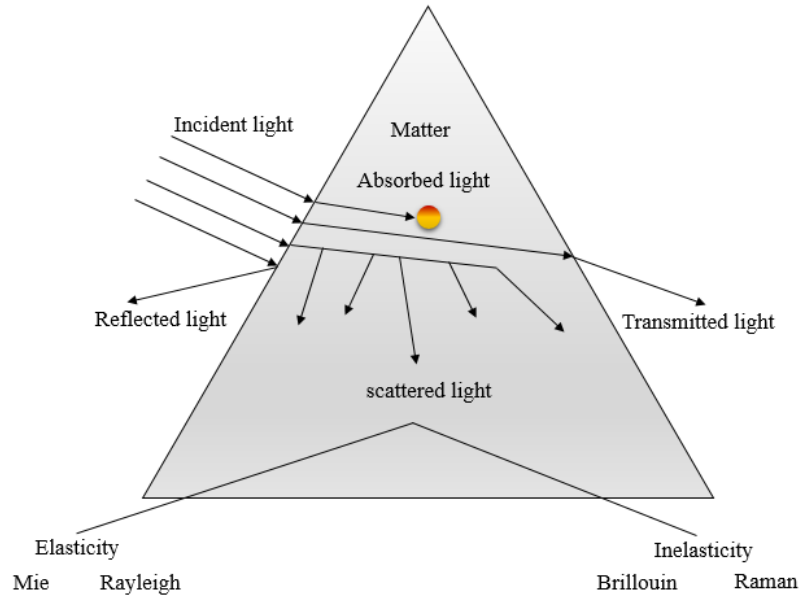


**Figure 4.11:** The sketch shows possible light-matter interactions. Adapted from [94].

Different kinds of materials have specific interactions with light; for example, bulk metals have 90% of the incident light reflected in the visible light range and about 10% is absorbed. Semiconductors materials can transmit light with an energy lower than their band gap and absorb light with an energy above their band gap.

- **Transmittance**:

The light reaching the surface of a sample and transmitting can be defined by its transmittance [131, 132], namely the ratio of the transmitted flux ($I_t$) to the incident flux ($I_o$), that is

$$T = \frac{I_t}{I_o}$$

[4.5]

- **Absorbance**

The absorbance (A) is the fraction of radiation absorbed with respect to the radiation that strikes the surface of the material. The absorbance A is on the material's thickness even so the $\alpha$. The absorption coefficient $\alpha$ is, in case of no reflection, given by $\alpha = \frac{1}{d} ln[\frac{1}{T}]$, where $d$ is the thin film thickness and $T$ is the transmission. Alternatively, A is the logarithm to base 10 of the transmittance, that is,

$$A = -log_{10}(I_t | I_o) \tag{4.6}$$

Absorption is the decrease in the intensity of a beam of photons or particles due to its passage through a particular substance or medium. When light passes through or is reflected from a sample, the amount of light absorbed is the difference between the incident radiation ($I_o$) and the transmitted or reflected radiation (I).

From the above, it is clear that knowing the transmittance of a material, its absorption can be calculated. Since generally only photons with an energy ($hv$) above the bandgap of the material ($E_g$) are absorbed, the absorption and the bandgap are also closely linked. The relation between the absorption coefficient and the bandgap is given by the following formula:

$$\alpha hv = A(hv - E_g)^{-n} \tag{4.7}$$

where the exponential $n$ depends on the type of transition. For semiconductors with a direct band gap the value of n is 2 and for an indirect band gap is 1/2.

- **Reflection**

Reflection is the fraction of the incident radiation of a given wavelength that is reflected when it strikes a surface. Reflection as defined by the Fresnel equation is the ratio between incident and reflected intensities and depends on the polarization direction with respect to the interface thus,

$$R_\perp = \frac{tan^2(\theta_1 - \theta_2)}{tan^2(\theta_1 + \theta_2)} \tag{4.8}$$

$$R_{//} = \frac{sin^2(\theta_1 - \theta_2)}{sin^2(\theta_1 + \theta_2)} \tag{4.9}.$$

In the equations [4.8] and [4.9], the incident angle is represented by $\theta_1$ while the transmission angle is $\theta_2$.

The relation between T, A and reflectance R, according to the law of conservation of energy is given by

$$A + T + R = 1 \ . \tag{4.10}$$

In this thesis, the absorption and transmission measurements were carried out using the Schweizerische Stiftung für Edelstein-Forschung (SSEF) portable UV-Vis Spectrometer. It is a spectrometer with a sample chamber and an optical fiber cable. It is equipped with a light control switch and a luminescence i.e. UV transparent light diffuser. The Spectrometer platform is AvaSpec-2048 with a symmetrical Czerny-Turner configuration, 75 mm focal length, with a contribution from stray light of less than 0.1%. The CCD linear array detector has 2048 pixels, a UV detector coating, and a slit size of about 25 µm.

The UV transparent light diffuser ensures illumination of the sample exposed under it, the Visible (halogen and Xenon) and UV (LEDs) lights are switched on/off separately. The spectrometer has a number of plastic rings as sample holder with adjustable aperture depending on the sample size, protective cover against surrounding stray light, with UV light resistant fiber, see Fig. 4.12 for the sketch of the simple but efficient SSEF portable UV-Vis Spectrometer.
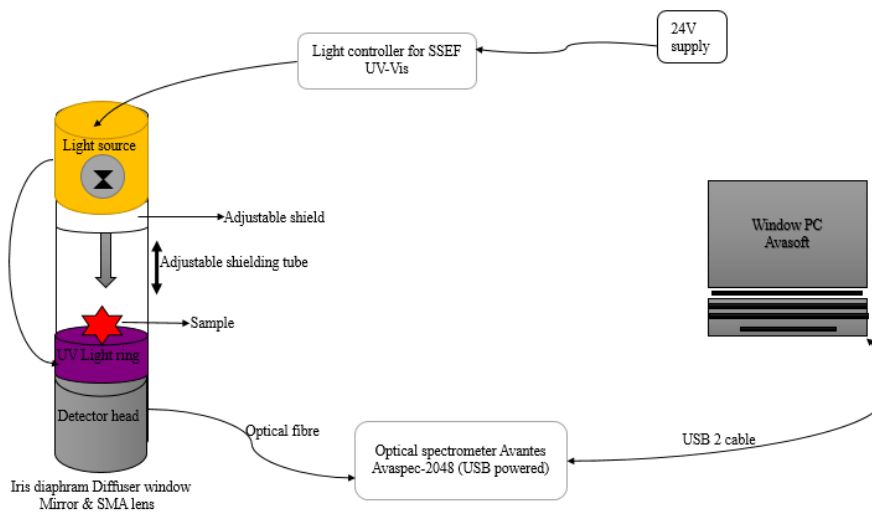


**Figure 4.12:** Sketch of the SSEF portable UV-Vis spectrometer.

In the measurements, the integration time was set to 300 ms, averaging 100 spectra and the transmission scale was 0 to 100 while the wavelength spanned from 175nm to 1100nm. The dark measurement without sample was recorded followed by the FTO sample reference for the bright field measurement under both Xenon and the Halogen light simultaneously. With the dark and bright field (reference) measurements spectra acquired, the transmittance of the samples could be measured. The samples were placed into the holder one at a time and the diaphragm was closed gently to avoid stray light from the environment and to acquire the transmittance of the deposited thin films. The obtained spectra are displayed in Sec. 5.3 in Chapter 5. In addition, the calculated results for absorbance, absorption coefficient, and the existence of a direct band gap will be discussed.

In the previous chapters, we discussed the synthesis method of copper oxides thin films, as well as the characterization techniques. This chapter presents the properties of successfully deposited $Cu_xO$ thin films on Si and glass substrates and the results of the investigations of their morphology and structure. There was no clear path towards the deposition of reproducible $Cu_xO$ thin films so we introduced post deposition thermal treatment as a way of improving the quality of the films and their reproducibility. In this chapter, we investigate the effect of annealing at different temperatures on the produced films. The morphology of the grown thin films were revealed via the SEM micrographs, the quantitative elemental compositions analysis was conducted using the EDX and the AFM technique examined the topography of the top surface of the grown thin films. The investigations are displayed and discussed systematically. We present here also the samples' work functions measured as contact potential difference using KPFM as well as XRD and Raman fingerprints found in the grown $Cu_xO$ thin films. Moreover, we discuss here the optical transmission results. Finally, we examined the effect of aging using AFM, KPFM and SEM and the results unveil the growth of unwanted crystallites, as it is presented and discussed at the end of this chapter.

**5.1 Investigation of $Cu_xO$ thin films deposited on Si substrates**

In this section, we discuss the investigated properties of $Cu_xO$ films that were deposited onto Si substrates. The oxygen partial pressures at deposition were 15% and 23% and the films were thermally treated after deposition. Further details on the deposition conditions are given in Section 3.3. We characterized the obtained samples via SEM, EDX, AFM/KPFM to see the morphology, chemical composition and the topography of the films along with their contact potential difference. XRD and Raman characterization were used to reveal the structures of thin films.

**SEM results**

The deposition of Cu$_x$O thin films and the subsequent thermal treatment was discussed in Chapter 3. After deposition, the films were characterized starting from the morphological analysis. To compare results arising from a difference in oxygen partial pressure during deposition onto Si substrates, we choose a representative sample of the ones containing nominally 23% oxygen at deposition and compared that to the samples with 15% oxygen partial pressure. In the following sections, we will describe the results of the investigation.

To study the evolution of the surface morphology with annealing temperature, the films were analysed via SEM at 5 kV. The obtained images of the as-deposited and annealed films (formed with 15% or 23% O$_2$ partial pressure) are presented in Fig. 5.1. While the cross sections of each film is captured and presented under additional figures, see Fig. 6.3.
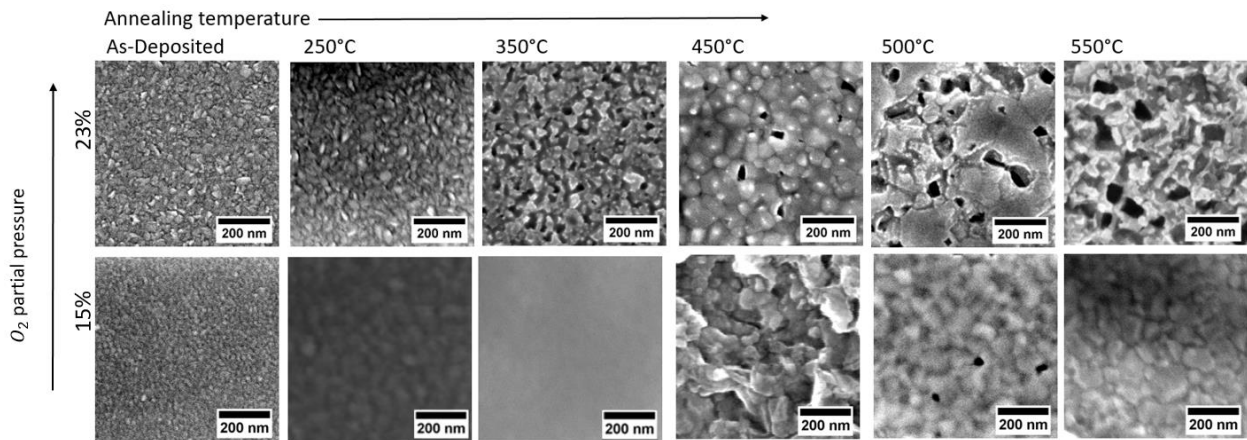


**Figure 5.1:** SEM surface morphology of sputtered thin films on Si substrates deposited at 15% (bottom panels) and 23% (top panels) O$_2$ partial pressure. Annealing temperature increases from left to right.

The images show that the annealing of the Cu$_x$O thin films produced some changes in the microstructures. While the as-deposited films show densely packed grains that are homogeneously distributed, the pattern and shape of the annealed thin films evolve greatly with the annealing temperature increase: besides the change in the morphology of the grains, which become bigger and less homogeneous, we also notice dark spots on the annealed samples

showing that they became nano-porous films. However, these voids (pores) could be present in films before annealing that may not be physically visible but expand on annealing. Sometimes the voids could result from deposition conditions such as the substrate temperature, the sticking coefficient of the molecules as they settle down on the substrates, and thermal strain [133, 134]. Sometimes porosity (voids) are beneficial for specific applications. Indeed, porosity can be beneficial in MO $Cu_xO$ for solar cell applications, e.g. the porosity of films allows for the absorption of dye molecules in Dye Sensitized Solar Cells and to avoid cracking and buckling in solid structures. We observe that although films obtained with both oxygen partial pressure during deposition show a change in morphology caused by the annealing, the changes for the higher oxygen ratio are more conspicuous, as they exhibit agglomerated grains.

**EDX results**

EDX was employed for elemental identification and composition analysis of the deposited samples, as described in Chapter 4 (Section 4.2). The EDX characterization, performed at 10 kV, was conducted on both the pristine samples and those annealed at 500 °C, deposited at 15% and 23% $O_2$ partial pressures onto Si substrates. The extracted data were taken in an area of 1 μm x 1 μm. The EDX results, displayed in Fig. 5.2, show that in the sample deposited at high oxygen partial pressure the oxygen percentage decreases upon annealing. In particular, the oxygen ratio of the film annealed at 500°C decreased from 23% to 20%, which highlights the effect of annealing on Cu-O, i.e. a reduction of the compound. This result suggests an annealing-mediated change in the relative Cu and oxygen contents possibly related to a phase change, which we have also investigated by XRD and Raman.
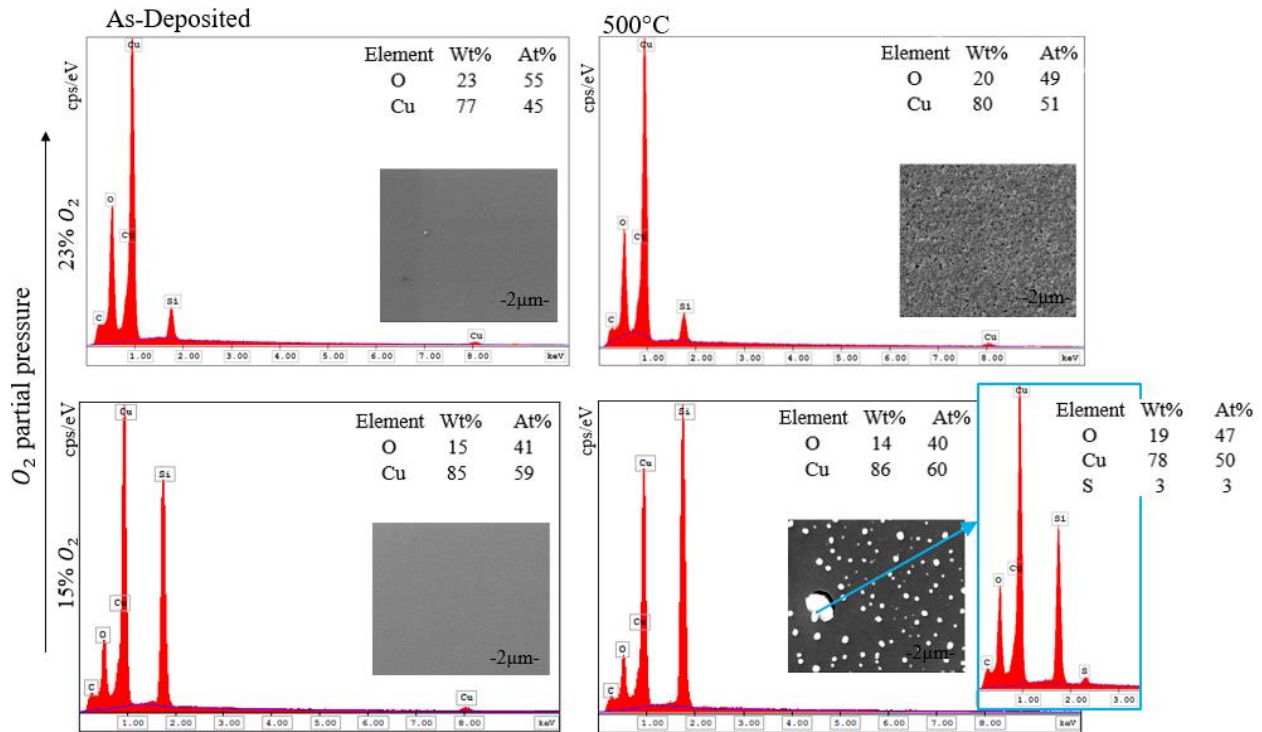
**Figure 5.2:** EDX spectra and insets with the SEM micrograph showing both as-deposited (left panels) and annealed at 500°C (right panels) sputtered thin films deposited on Si at 15% (bottom panels) and 23% (top panels) $O_2$ partial pressure. The extracted data were taken in an area of 1 µm x 1 µm. The 15% $O_2$ sample at 500°C has an inset describing the analysis for the cluster spot, which contains Sulphur and has a higher oxygen content, 19%. In the table, Wt % indicates the weight percentage and At % indicates atomic percentage of the element.

The EDX spectra contain other elements besides the expected Cu and O, like Si, which is coming from the Si substrates, and C (carbon), that is a common contaminant of oxides [135]. The other source of the carbon could also be the SEM exposure, which was carried out before the EDX measurement.

It is evident that the Si peak is quite high in the EDX spectra of the sample with 15% oxygen partial pressure. This could be possibly due to the thinness of the film, whose cross-sectional SEM image is shown in Fig. 4.2. Finally, as shown in the inset of Fig. 5.2, the thin film deposited at 15% $O_2$ partial pressure and annealed at 500°C displays some clusters (white spots in the SEM image) which contain Sulphur (3%); the EDX analysis also reveals that the cluster has higher oxygen content (19%) than in the clean surface without cluster (14%). The Sulphur (S) is suspected to be a contaminant from the covering oxide layer of the Cu target, which then comes to the surface at higher annealing temperatures. If this speculation is correct, all the

samples should be S contaminated. We explain the detection of this contamination only in this sample because of the creation of cluster with a higher S concentration. In this respect, it is worth remembering that the detection limit of EDX is approximately 1%, explaining why Sulphur wouldn't show up outside of these clustered areas. The clusters were not seen in previous depositions so further investigation is required to corroborate this theory..

**AFM/KPFM results**

AFM in tapping mode and KPFM investigations were carried out on the samples grown at 23% oxygen to obtain their topography and CPD, respectively, as described in Chapter 4 (Section 4.3). The scanned area was 8 x 8 $\mu m^2$ and the CPD was measured from ~110 mV to ~360 mV. Fig. 5.3 shows the AFM images in the top panels and their corresponding CPDs in the bottom panels for increasing annealing temperature from left to right. While the height scale bar was fixed for all the AFM images shown as main panels, the insets in the AFM images display a 4 x 4 $\mu m^2$ section of the original images with the optimal height scale. We observe an increase of grain size as the annealing temperature increases, which is consistent with the SEM results. The Root Mean Square (RMS) surface roughness deduced from the AFM topography images are: 1.9 nm, 1.8 nm, 6.2 nm, 5.1 nm, 10.9 nm and 28.3 nm, for increasing annealing temperature.
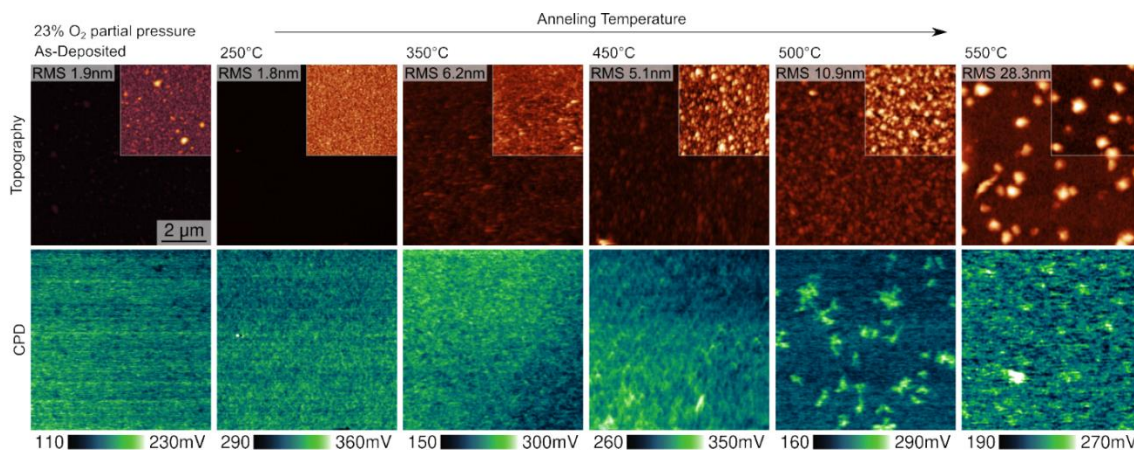


**Figure 5.3:** AFM topography (top panels) and CPD (bottom panels) of sputtered thin films on Si substrates at 23% $O_2$ partial pressure. Annealing temperature increases from left to right. The scanned area is 8 x 8 $\mu m^2$. The height

scale bar was adjusted to $\Delta z = 200$ nm for the top panels. In the insets, we show a 4 x 4 $\mu m^2$ section rescaled to the optimal height range. Overall, the AFM images show an increase in the RMS roughness as the temperature increases.

In the bottom panels, the CPD measurements show a nearly homogeneous distribution up to an annealing temperature of 450 °C. Only above this temperature, we found regions with higher and lower CPD values correlated with higher and lower work functions, respectively. We suspect that these areas represent the co-existence of CuO and $Cu_2O$ crystals, since the just discussed EDX and the XRD and Raman results that will be discussed all point to the co-existence of these two phases in the sample deposited at 23% oxygen partial pressure for these annealing temperatures. Generally, it is expected for $Cu_2O$ to have a lower work function than CuO: $\Phi[Cu_2O] = 4.84$ eV and $\Phi[CuO] = 5.32$ eV [118, 136]; however, the work function depends also on crystallinity and doping concentration, which could even reverse the order of work funtion between the two phases. This work function allows us to correlate the bright areas with remaining CuO segregating at 500 °C and vanishing for higher temperatures. The exact values of the work function would only be available if a calibrated tip had been used.
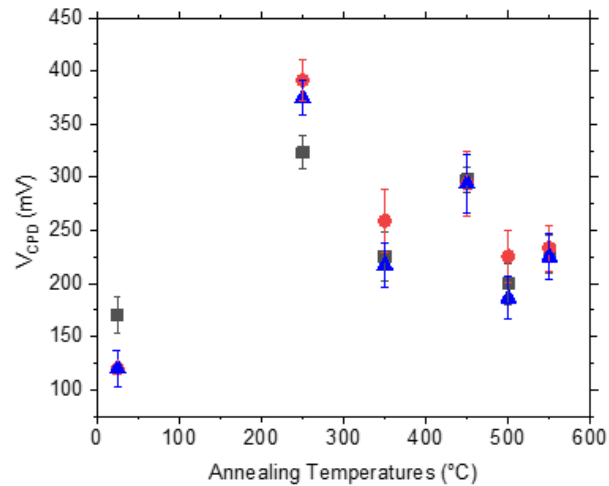


**Figure 5.4:** CPD values extracted at three different positions on each sample grown at 23% oxygen for all annealing temperatures. The black squares, red circles and the blue triangles represent the different positions on the sample surfaces. The error bars come from the variations in measured values for each position of the thin films.

CPD values were obtained at three different positions on each sample for all annealing temperatures as shown in Fig. 5.4. The similarity between the three points within a sample proves that tip changes or sample inhomogeneity are influencing only marginally the following conclusions. We observe an increase in the sample work function (measured as contact potential difference) of about 200 mV as we anneal the sample at 250 °C. This increase is probably due to the cleaning (reorganization of the surface due to annealing in vacuum) of the CuO surface. Further increase of the annealing temperature shows an overall decrease of the sample work function most probably due to the increasing formation of $Cu_2O$. There was a time lag between the deposition (and annealing in vacuum) and this investigation, thus we cannot rule out air contamination; moreover, glove box annealing to remove residual water was not conducted. Generally, contamination by water homogenizes work function differences at surfaces; therefore, we do not expect to see the theoretical values for the work functions of CuO and $Cu_2O$ [136, 137].

**XRD results**

The structural analysis was performed using XRD in the scanning Bragg angle 2Θ from 20° to 72°. The $Cu_2O$ phase belongs to the space group $Pn\overline{3}m$ or $O_h^4$, documented in the Inorganic Crystal Structure Database (ICSD) pattern 01-077-0199, while the CuO belongs to the space group C2/c (ICSD pattern 00-045-0937). Figure 5.5 shows the XRD patterns of the different deposited films, with contributions from the different copper oxide phases. The thin films sputtered at 15% $O_2$ partial pressure (see panel a and its magnification below it) have patterns indexed to planes of the $Cu_2O$ phase, namely the reflections at 29.56° (110), 36.18° (111) and 42.43° (200). In the 350 °C sample, the plane at 29.04° (110) is attributed to the $Cu_2O$. The data indicate a phase transition at 450 °C where both oxides coexist. Indeed, the diffraction peaks at 35.70° (-111) [72] and at 38.86° (200) are attributed to CuO. At 500 °C and 550 °C we notice the disappearance of the CuO peaks, with the exception of a tiny peak at 38.86° (200), while all the $Cu_2O$ peaks stay.
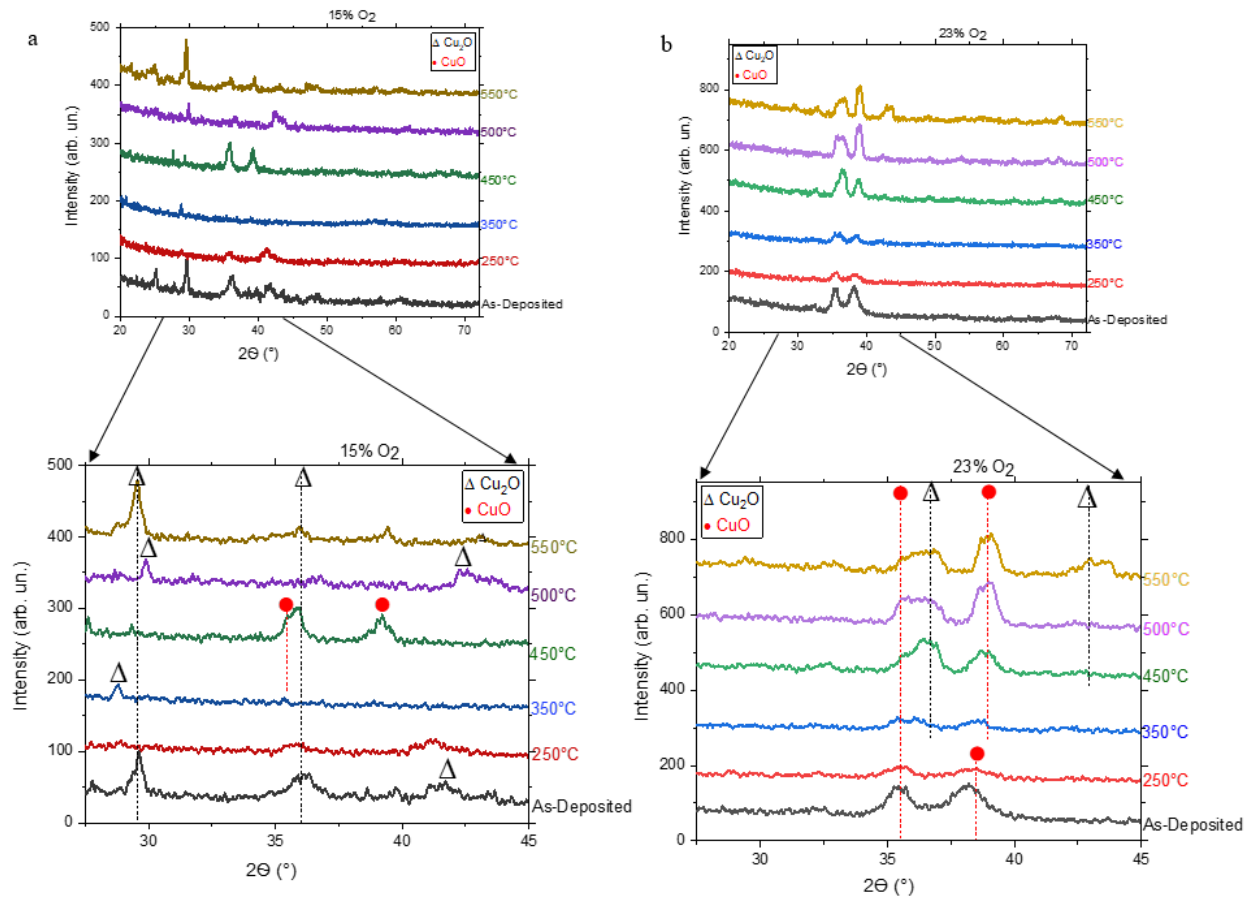
**Figure 5.5:** XRD patterns of nanoporous thin films prepared on Si substrates by RF-magnetron sputtering at 15% (panel a) and 23% (panel b) $O_2$ partial pressure. In the bottom panels (zoom between 27.5° and 45°), triangles and circles indicate peaks attributed to $Cu_2O$ or CuO, respectively, and the dashed lines highlight their evolution. The spectra are vertically shifted for clarity. Annealing temperature increases from bottom to top.

Figure 5.5b shows the XRD data of all the films sputtered at 23% $O_2$ partial pressure. It displays diffraction peaks of CuO at 35.43° (-111), 38.54 (111)  [138], and 38.86° (200). Figuiredo [72] and Nair [139] revealed in their studies that at annealing temperatures greater than 350°C $Cu_2O$ could reverse to CuO. While in our study, we observed both this and the reverse trend. $Cu_2O$ transforming to CuO with annealing up to 450°C and CuO reversing to $Cu_2O$ beyond 450 °C (for the low $O_2$ partial pressure deposited samples), and CuO partially transforming to $Cu_2O$ at 350 °C (for the samples deposited at high $O_2$ partial pressure), the latter being similar to ref. [3]. The observation of the partially opposite trend compared to literature

could arise from the fact that in those studies annealing was performed in air, while, in our study, it was performed in vacuum. The annealing-driven reduction process leads to the formation of $Cu_2O$.

## Raman results

To further elucidate the structural composition of the thin films and its dependence on annealing temperature, we performed Raman spectroscopy studies on all films. Figure 5.6 shows the Raman spectra of the as-deposited and annealed thin films for both sputtering processes at 15% and 23% $O_2$ partial pressure (panels a and b, respectively).
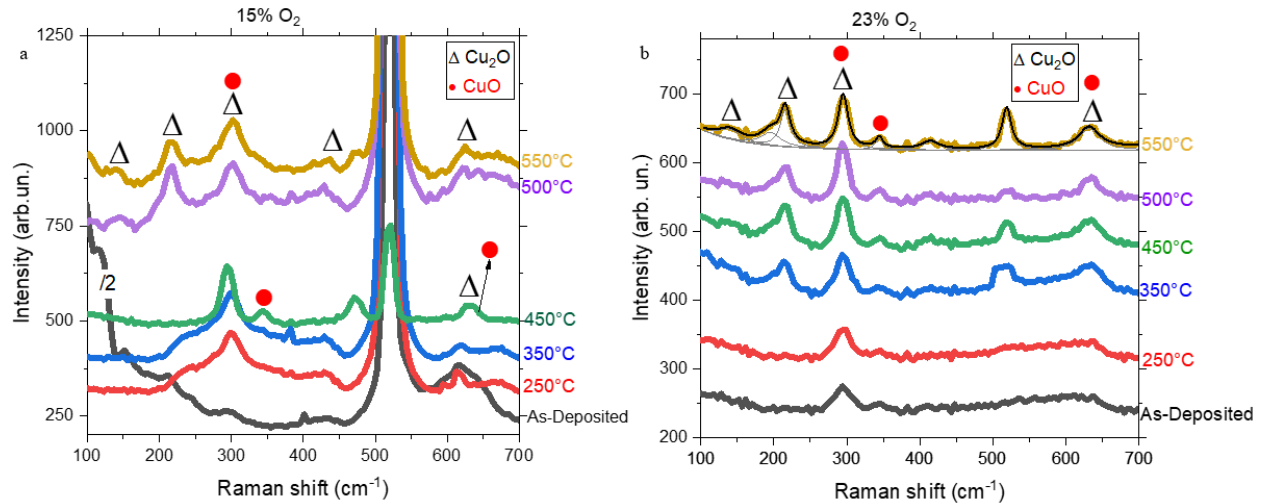


**Figure 5.6:** Raman spectra of nanoporous thin films prepared on Si substrates by RF-magnetron sputtering deposited at 15% (panel a) and 23% (panel b) $O_2$ partial pressure. The spectra were vertically shifted for clarity. Annealing temperature increases from bottom to top. In panel a, the intensity of the Raman spectrum of the as-deposited thin film was halved to accommodate it into the spectra stacking, as indicated by the division by 2 in the spectrum. In panel b, the increased thickness (279 nm) of the film screens the contribution of the Si substrate peak at 521 cm$^{-1}$. Peaks attributed to $Cu_2O$ or CuO are indicated by triangles and circles, respectively. As a representative case, in the spectrum of the sample annealed at 550 °C in panel b we show the fitting procedure: grey thin lines indicate the Lorentzian components, and the black thin line is the cumulative result.

We performed a careful quantitative analysis of the collected spectra. As an example of the deconvolution procedure, we display the fitting with Lorentzian curves of the whole spectrum of the sample annealed at 550 °C in Fig. 5.6b (see grey and black thin lines), from

which we derived the full width at half maximum (FWHM) and the average intensity of each peak. The FWHM and the average intensity are plotted in Fig. 5.7 for selected phonon modes.
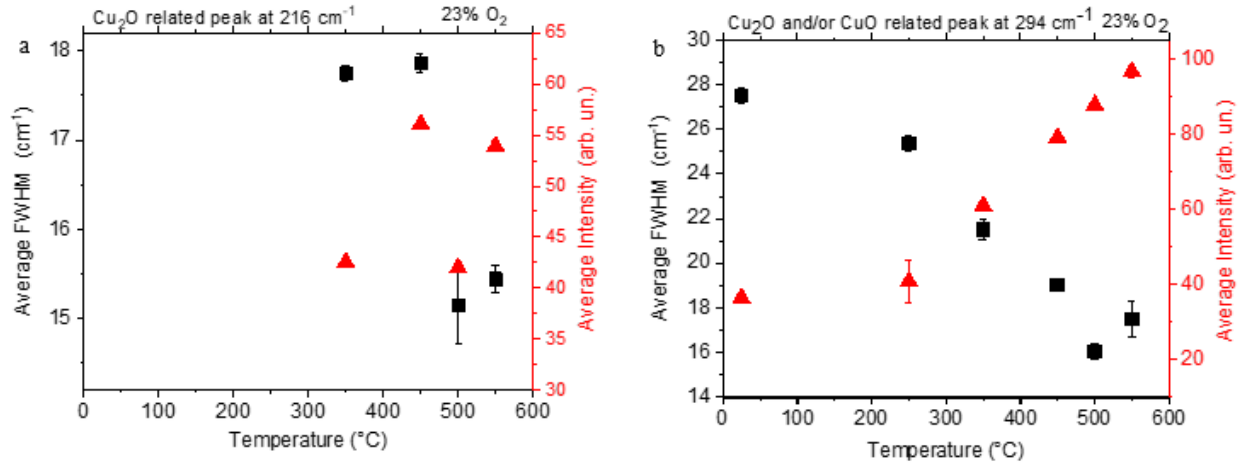


**Figure 5.7:** Intensity (red triangles) and FWHM (black squares) relative to the 216 cm$^{-1}$ mode (panel a) and to the 294 cm$^{-1}$ mode (panel b) as extracted from the fits of the data in Fig. 5.5b. The experimental data are the result of averaging over two positions on the samples, and the error bars represent the corresponding semi-dispersion. Data (in both panels a and b) refer to the 23% O$_2$ sample.

In all the spectra shown in Fig. 5.6, the peak at 521 cm$^{-1}$ comes from the Si substrate. In the thinner films, namely, those deposited at 15% oxygen partial pressure, the Si substrate signal is very intense in all the spectra, as expected due to the smaller film thickness. In the 15% O$_2$ films annealed at high temperatures, i.e. 500 °C and 550 °C, we observe a peak at 145 cm$^{-1}$ having low intensity, which can be assigned to phonons of symmetry $F_{1u}$ of Cu$_2$O [94, 100, 138, 140]. The next peak (in order of frequency shift) that we observe is at 214 cm$^{-1}$. It has very low-intensity in the as-deposited thin film and in the annealed ones at 250, 350, and 450 °C [138]. This peak shifts to 216 cm$^{-1}$ and largely grows in intensity for annealing temperatures higher than 500 °C. It corresponds to the second order Raman-allowed mode $2\Gamma_{12}^{-}$ of Cu$_2$O [100, 140]. The small peak at 435 cm$^{-1}$ in the 500 and 550 °C annealed sample can be ascribed to the combination of four phonon modes, $3\Gamma_{12}^{-} + \Gamma_{25}^{-}$, of Cu$_2$O [94, 127, 141]. The broad asymmetric peak at ~435 cm$^{-1}$ visible in all the samples (with the exception of the 450 °C sample, in which for a reason that we are still investigating the modes coming from the substrate are not very visible) is ascribed to the acoustic modes of the Si substrate. The broad peak centred at 302 cm$^{-1}$ and visible at temperatures 250, 350, 500 and 550 °C is a second order mode of the Si substrate.

That peak is clearly distinguishable (due to its spectral shape and frequency) from the prominent peak at 294 cm$^{-1}$, visible in the thin film annealed at 450 °C and attributed to a second order overtone mode with $A_{2u}$ symmetry belonging to $Cu_2O$ [100]. We notice that this peak would also be compatible with the $A_g$ mode of CuO when it is strained or nanostructured [94]. We have considered also this possible assignment because of the presence of grains in our thin films. The sample at 450 °C has a weak peak at 344 cm$^{-1}$, which may be attributed to a $B_g$ mode of cuo [6, 125]. the peak at 470 cm$^{-1}$ disappears at 500 °c and reappears weaker at 550 °C, this peak do not have CuO and $Cu_2O$ energy, probably belongs to other phases of the metastable $Cu_3O_2$ or the paramelaconite $Cu_4O_3$ phase. The peak at about 635 cm$^{-1}$, seen at 450°C, whose frequency agrees with the infrared-allowed transverse optical mode of $Cu_2O$ with symmetry $\Gamma_{15}^-$, can be observed in a Raman scattering experiment as a result of selection-rules violation mechanisms [6, 127, 142]. We observe that this peak may be compatible also with the $B_g$ mode of CuO and it could be interpreted as a Raman-allowed optical phonon mode of CuO [143]. The samples annealed at 250 °C and 350 °C, 500 °C and 550 °C show instead a peak at 624 cm$^{-1}$ attributed to $Cu_2O$ [138] [144]. In conclusion, similarly to the XRD data, the Raman data point to a phase transition occurring at 450 °C that makes this a crucial annealing temperature for the deposition process performed at lower $O_2$. Indeed, our results show that at low (15%) reactive deposition gas, $Cu_2O$ can be obtained at deposition.

We now turn our attention to the thin films sputtered at 23% oxygen partial pressure. Here, the increased thickness of the film which is 279 nm screens the contribution of the Si substrate. This can be reasonably expected for films made by highly absorptive materials, such as copper oxides [18]. The as-grown film and the one annealed at 250 °C contain both oxide phases of CuO and $Cu_2O$. Indeed, the spectra of these samples display an intense peak at 294 cm$^{-1}$ attributed to $Cu_2O$ (and possibly CuO as described before) [100, 144]. The broad peak at 635 cm$^{-1}$ is as discussed above [6, 127, 142, 143]. The moderate peak at 344 cm$^{-1}$ is CuO-related [58, 134]. The low intensity peak at 145 cm$^{-1}$ is assigned to $Cu_2O$ as discussed above [94, 100, 138, 140]. At 350 °C, we observe a phase transition involving oxygen diffusion. This is evident in the extra $Cu_2O$ signature peaks at 216 cm$^{-1}$ and 416 cm$^{-1}$ (see, e.g., the appearance of the 216 cm$^{-1}$ mode at 350 °C in Fig. 5.7a), as well as in the increase in intensity of the already present peaks at 294 cm$^{-1}$ and at 635 cm$^{-1}$, which become narrower and more intense. The intensity of the 294 cm$^{-1}$ mode increases even more for the subsequent annealing temperature of 450, 500 and 550 °C

(see its intensity as a function of annealing temperature in Fig. 5.7b). While its frequency stays quite constant with temperature (it varies by about $1 \, cm^{-1}$, namely less than the spectral resolution), its intensity starts to increase at 350 °C due to the already discussed phase transition. Furthermore, its FWHM, plotted in Fig. 5.7b, decreases, which points to an improved crystal quality for higher annealing temperatures. In conclusion, the correlation between XRD and Raman data shows that in the 23% sample, differently from the 15% sample, CuO is obtained at deposition (this is particularly evident in the XRD data). Moreover, the annealing process in vacuum on the higher oxygen pressure sample partially converts CuO to $Cu_2O$.

Finally, we investigated the homogeneity of the films by performing spatially-resolved Raman measurements over several samples. In Fig. 5.8 we show the results on two representative samples. We plot the Raman spectra magnified in the frequency region of the mode at $216 \, cm^{-1}$ measured on twelve different points, spaced from each other about 0.8 µm, of the samples annealed at 500 °C for both 15% $O_2$ (panel a) and 23% $O_2$ (panel b) samples. The fluctuations in the frequency are small, lower than the spectral resolution, which points to a good homogeneity of the samples (at least on a scale larger than the laser spot) in this region (6 x 6 µm$^2$). The homogeneity over larger distances was also confirmed by the measurements on two different points spaced by about 50-200 µm as explained in the caption of Figure 5.7.



**Figure 5.8:** Raman spectra magnified in the frequency region of the $Cu_2O$ mode at $216 \, cm^{-1}$ acquired on twelve different positions of the samples prepared with 15% (panel a) and 23% (panel b) $O_2$ partial pressure and annealed at 500 °C. Dashed lines mark variation in central frequency of the mode, that for a) is about $2 \, cm^{-1}$ and for b) is about $1.2 \, cm^{-1}$. Data were obtained by mapping the sample over an area of 6 x 6 µm$^2$ with steps of 0.5 µm. An offset was added between spectra. Fluctuations in the intensity can be attributed to slightly different focusing conditions (the focus was not optimized in each point, as it was instead done in the single point measurements in Fig. 5.6).

## 5.2 Investigation of the reproducibility of different deposition processes on Si and annealing

The purpose of this section is to compare the results of the different deposition processes performed with nominally the same parameters. For this study, we will focus on three samples deposited at high (23%) oxygen partial pressure on Si, both pristine and annealed at 500°C. One of these samples (that we will call from now on the S3) is the same one which Section 5.1 is focused on. The other two (S2 and S4) are discussed in this Section for the first time.

### SEM results

Figure 5.9 displays the SEM images of as-deposited thin films, showing compactly packed grains of uniform sizes that are uniformly distributed on the substrates. The as-deposited S2 and S3 deposition samples look very similar while the micrograph of S4 deposition, though blur, differs from the other two, justifying the further structural analysis.
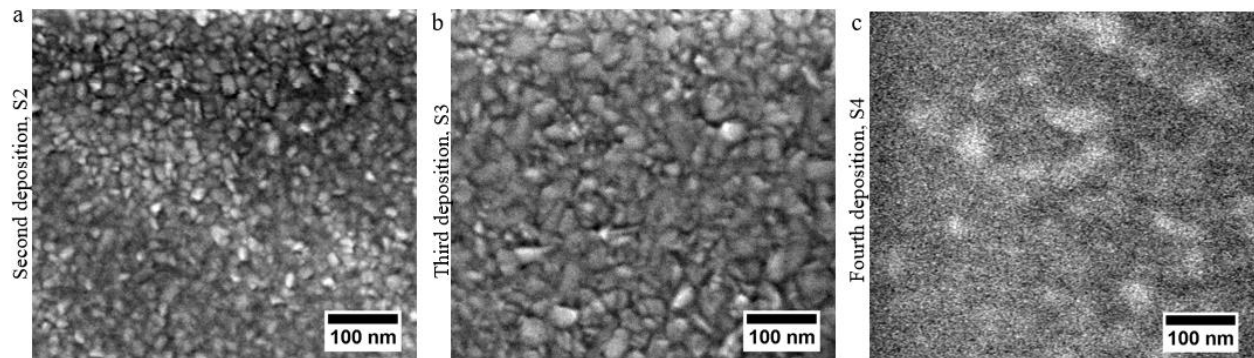


**Figure 5.9:** SEM surface morphology of sputtered thin films on Si substrates deposited at 23% $O_2$ partial pressure before annealing treatments. All three films were deposited with nominally the same parameters in different, not simultaneous, deposition processes. Panels a, b and c represent second, third and fourth depositions, hence, will be referred to as S2, S3 and S4, respectively.

**EDX results**

The copper to oxygen ratio estimated by the weight and atomic percentage of each element in the three depositions at nominally 23% oxygen partial pressure are tabulated in Table 5.1. The results show that the resulting actual oxygen partial pressure has some variations, as the second and third deposition turned out to be very similar (with oxygen ratio of 23%), while the fourth deposition results in a slightly lower oxygen ratio (3% less than the other two). Moreover, the EDX measurements confirm that annealing reduces the oxygen content, as discussed in Section 5.1. In particular, here they show that the oxygen content of the S4 as-deposited sample (20%) is equivalent to the oxygen present in the annealed samples at 500 °C of the S2 and S3 deposition. We will see in the following, via the Raman and XRD results, how this different actual oxygen content affects the structural composition of the grown films.

| Samples (23% O2) | Ann. Temperature (°C) | Elements | Weight% | Atomic% |
|---|---|---|---|---|
| 2nd deposition (S2) | not annealed | O | 23 | 54 |
|  |  | Cu | 77 | 46 |
|  | 500 | O | 20 | 50 |
|  |  | Cu | 80 | 50 |
| 3rd deposition (S3) | not annealed | O | 23 | 55 |
|  |  | Cu | 77 | 45 |
|  | 500 | O | 20 | 49 |
|  |  | Cu | 80 | 51 |
| 4th deposition (S4) | not annealed | O | 20 | 50 |
|  |  | Cu | 80 | 50 |
|  | 500 | O | 16 | 43 |
|  |  | Cu | 84 | 57 |

**Table 5.1**: EDX results for Cu-O elements showing as-deposited and annealed at 500 °C thin films deposited on to Si at 23% $O_2$ partial pressure for all three depositions with nominally the same parameters. The data were acquired on an area of 1 x 1 $\mu m^2$.

## XRD results

Figure 5.10 presents the XRD patterns obtained on the S2, S3, and S4 samples, as-deposited (panel a) and annealed at 500°C (panel b).
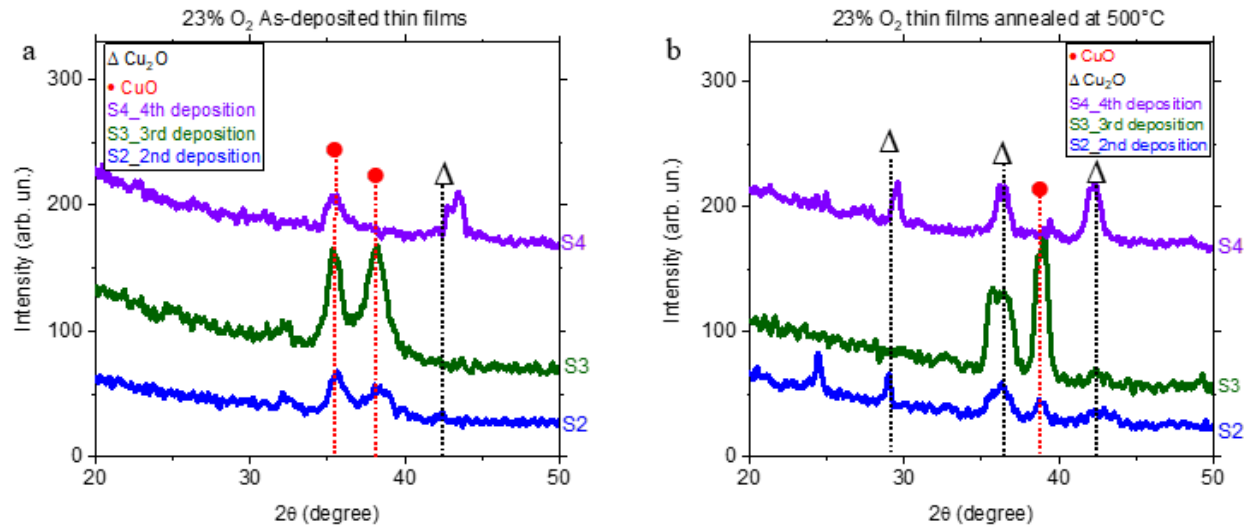


**Figure 5.10:** XRD patterns of nanoporous thin films prepared on Si substrates by RF-magnetron sputtering at nominally 23% $O_2$ partial pressure for all three depositions. Panel a refers to the as-deposited films and panel b to the annealed films at 500°C. The triangles and circles indicate peaks attributed to $Cu_2O$ or CuO, respectively, and the dashed lines highlight their evolution. The spectra are vertically shifted for clarity.

All the pristine films (with the exception of  S4) show diffraction peaks attributed to CuO at 35.43° (-111). S2 and S3 samples show also a peak at 38.54 (111), which is attributed to CuO too; in the S4 sample, instead, a peak appears at 42.82°, ascribed to $Cu_2O$ patterns (200). The thin films annealed at 500°C (see Fig. 5.10b) have three peaks indexed to planes of the $Cu_2O$ phase, namely the reflections at 29.56° (110), which is absent in S3, at 36.18° (111) and at 42.43° (200). The CuO peak at 38.54 (111) has a small intensity in S4. Here, we observe that annealing mediation is helpful in the formation of the $Cu_2O$ phase, which was clearly non-existent in the as-deposited thin films. The S4 deposition with three percent less oxygen than S2 and S3 shows highly intense peaks of $Cu_2O$ upon annealing. This result is in good agreement with the results discussed in Section 5.1 for the 15% and 23 % thin films.

## Raman results

Figure 5.11 displays Raman spectra obtained on S2, S3, and S4 as-deposited (panel a) and annealed at 500°C (panel b) films. The thickness of the S3 film screens the contribution of the Si substrate peak at 521 cm$^{-1}$, as previously discussed. The thicknesses for S2 and S4 are 150 nm and 145 nm, respectively, thinner than the 279 nm-thick S3.
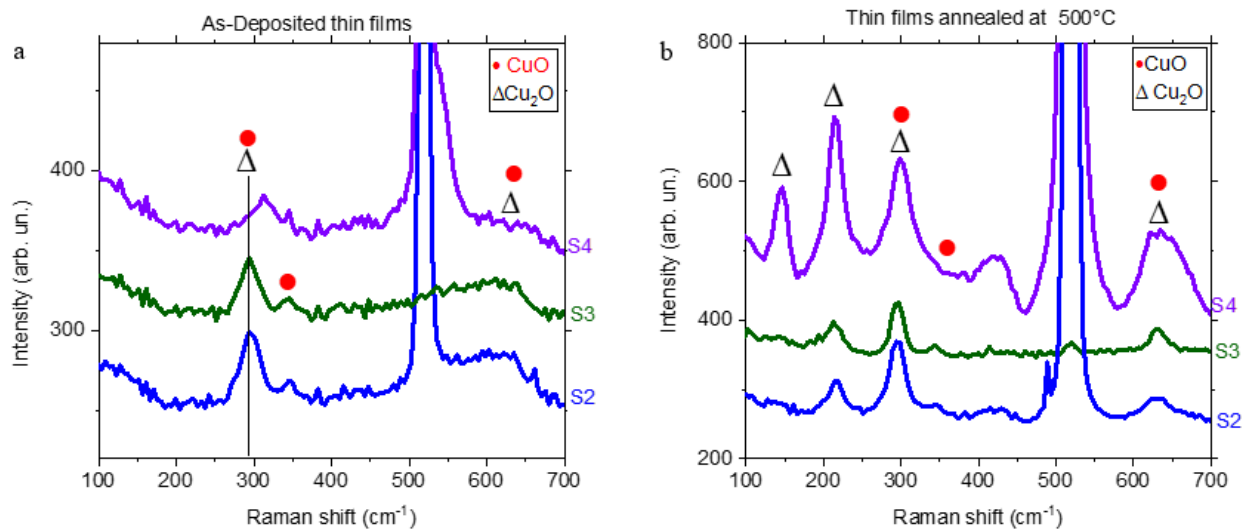


**Figure 5.11:** Raman spectra of nanoporous thin films prepared on Si substrates by RF-magnetron sputtering at nominally 23% $O_2$ partial pressure for all three depositions. Panel a refers to the as-deposited films and panel b to the annealed films at 500°C. Peaks attributed to $Cu_2O$ or CuO are indicated by triangles and circles, respectively. The thickness of the S3 film screens the contribution of the Si substrate peak at 521 cm$^{-1}$, as discussed in 5.1. The spectra were vertically shifted for clarity. The black line shows the evolution of the peak at about 300 cm$^{-1}$.

The S2 and S3 samples in panel a all display the same Raman modes at 298 cm$^{-1}$, 344 cm$^{-1}$ and 635 cm$^{-1}$, while the S4 peaks are at 313 cm$^{-1}$ and ~635 cm$^{-1}$. The modes interpretation is the same as in Section 5.1, and here it is summarized in the figure using the triangles and the circles to identify modes characteristic of a specific oxide phase. The mode at 313 cm$^{-1}$ was not interpreted in Section 5.1, and we are still investigating possible interpretations. S4 is quite different from S2 and S3, in agreement with the EDX results. In the thin films annealed at 500°C, see Fig. 5.11b, the Raman modes in S2 and S3 are basically the same: the peaks are located at 145 cm$^{-1}$ (with very low intensity), 213 cm$^{-1}$, 298cm$^{-1}$, 344cm$^{-1}$, 428 cm$^{-1}$ and 635 cm$^{-1}$. S4 has very similar peaks. Although the peaks of S4 increased in intensity upon annealing, no new peaks arose. The spectra of the annealed S4 look more similar to those of the annealed S2

and S3, despite the difference in as-deposited samples. In summary, even if the as deposited samples have quite different properties, the annealing makes them more similar, and therefore it seems a promising route to improve the reproducibility of the deposition processes.

In conclusion, in Sections 5.1 and 5.2 we have investigated copper oxide thin films grown at varying oxygen partial pressure on Si and studied the effect of annealing in vacuum on the resulting films to study possible routes to yield pure phase cuprous oxide ($Cu_2O$). We have shown that nominally identical deposition processes can result in slightly different oxygen content, and that annealing in vacuum is helpful in obtaining films with more similar properties. Moreover, we have shown that with increasing annealing temperature, porosity in the films arises. The thin films' structural properties were studied using Raman spectroscopy and XRD; both techniques gave consistent results, showing that the lower oxygen partial pressure at deposition favours the formation of $Cu_2O$. The annealing in vacuum favours the formation of $Cu_2O$, as CuO is reduced to $Cu_2O$ when annealed at temperatures above the critical temperature of 350 °C, especially for the deposition at higher oxygen partial pressure. The EDX composition analysis further supports the reduced oxygen content in these films. The homogeneity of the grown thin films was assessed using Raman mapping as well as KPFM measurements. Furthermore, KPFM measurements suggested that CuO segregates and vanishes at annealing temperatures above 500 °C.

In the next two sections, we will describe the deposition on glass substrates and compare the properties of the samples deposited on Si and on glass.

## 5.3 Effects of substrates on the properties of $Cu_xO$ films

This Section is to examine the effects of substrates on the depositions performed onto Si and FTO-coated glass substrates. Here we will focus on the fourth and fifth depositions that hence are referred to as S4 and S5, respectively. These depositions were performed onto Si and FTO coated substrates that were placed side by side on the same substrates holder to have identical deposition conditions for reproducibility purpose. The S4 deposition is at high (23%) oxygen partial pressure and the S5 deposition is at low (15%) oxygen partial pressure. The

properties of the S4 and S5 depositions onto Si were discussed in the previous sections, more specifically S4 in Section 5.2 and S5 in Section 5.1). The FTO depositions (S4 and S5) are discussed here for the first time.

**EDX results**

Here we examine the effect of substrates on the composition of the $Cu_xO$ thin films. From the EDX results of S4 on Si at nominally 23% oxygen partial pressure in Section 5.2 (table 5.1), we know that the oxygen content is 20%. The FTO-coated substrate alongside resulted instead in a 24% oxygen concentration at deposition. The 4% difference in the oxygen content can likely be attributed to the oxygen contribution from the FTO ($SnO_2$-F) layer, since EDX has a penetration depth of a few micron. The investigation of the S5 sample shows that the Si (Fig 5.2, Section 5.1) maintained 15% oxygen pressure at deposition and its FTO counterpart is 17%, namely it gained 2% of oxygen likely from the FTO oxide, as confirmed from the EDX quantitative results. The EDX for the as-deposited films is shown in Fig. 5.12.
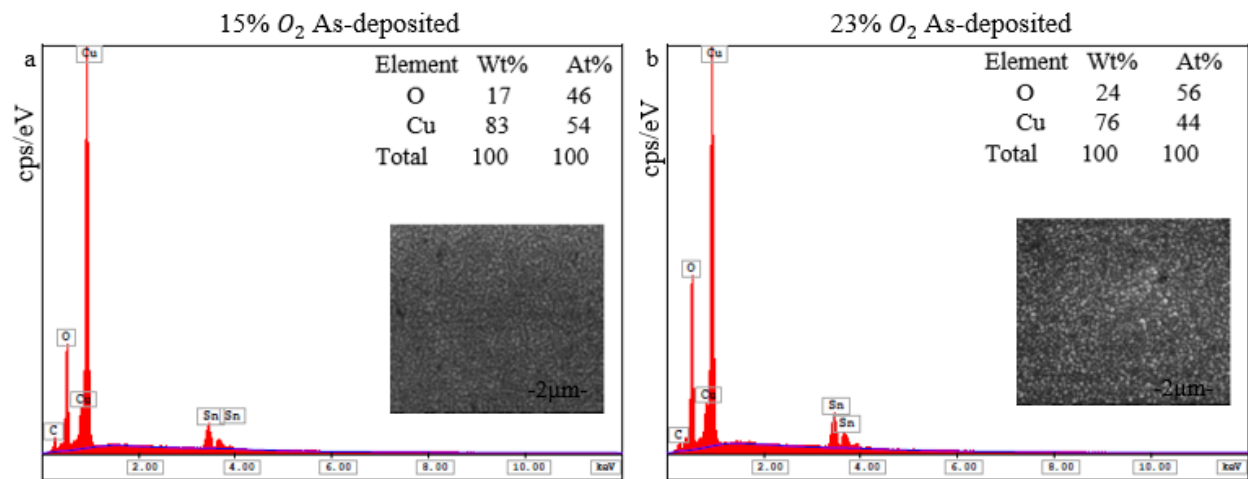


**Figure 5.12:** EDX spectra and inset with the SEM micrograph showing the as-deposited sputtered thin films deposited at 15% (a panel) and 23% (b panel) $O_2$ partial pressure. The data acquired on an area of 1 x 1 $\mu m^2$. In the tables, Wt% indicates the weight percentage and At% indicates atomic percentage.

## XRD Results

The structural investigation was performed via XRD and Fig. 5.13 displays the spectra of the films deposited simultaneously on Si and FTO. The XRD peaks of the FTO substrate, visible in the olive diffractogram, are also present in the XRD spectra of the thin films on FTO. As a result, the majority of peaks from the FTO samples stem from FTO rather than from $Cu_xO$. In Figure 5.13, we stack, in order, diffractograms taken on films on: Si at 15% $O_2$, Si at 23% $O_2$, reference FTO, 15% $O_2$ and 23% $O_2$ FTO. This is done for convenience for enabling the comparison. The obvious shift of the blue spectrum from the rest could be because of strain/stress, resulting from the deposition of $Cu_xO$ on top of the FTO layer or from a slight tilting of the sample during the XRD measurement. Since we cannot distinguish which of these effects is causing the shift the result is presented without any shift correction.
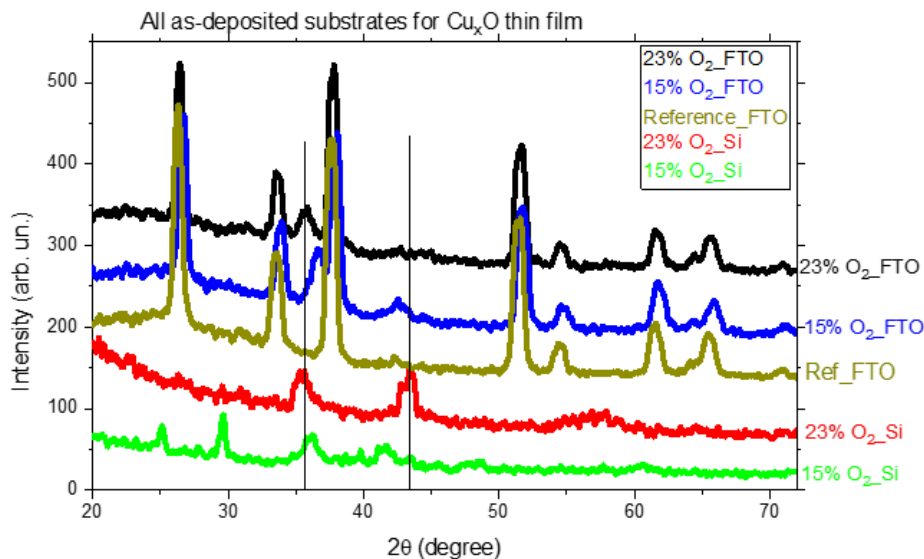


**Figure 5.13:** XRD spectra of the as-deposited thin films prepared onto Si and FTO-coated substrates by RF-magnetron sputtering at 15% and 23% $O_2$ partial pressure. The olive color spectrum is the FTO reference sample and it shows that indeed most of the peaks are coming from the FTO layer of the substrates. The black line is showing the evolution of the peaks. The observed shift in the blue spectra could be a result of strain created by $Cu_xO$ when deposited on top of the FTO layer. Therefore, we did not use the FTO peaks to calibrate the raw data.

The peaks associated to the copper oxides in the green diffract gram, i.e. the 15% O on Si, are similar to those obtained from the films deposited on FTO, with the exception of an extra

peak coming from Si at 29°. Overall, the similarities in the XRD data point out a similar stoichiometry of the films deposited on silicon and on FTO, when the films are deposited with the same parameters. The difference in the 15% and 23% deposition spectrum of the as-deposited thin films of Cu$_x$O is expected as they clearly have different stoichiometry owing to their deposition ratio. The FTO competing peaks with Cu$_x$O films are peaks at 26.49°, 38.12°, 51.54°, 61.47°, 65.88°.

Fig. 5.14 shows the spectrum of the 15% O$_2$ at deposition with an inset of the difference between an un-annealed FTO reference sample and the Cu$_2$O deposited sanple, to serve as a guide to the eye to show the distinct peaks of Cu$_x$O. The upper peaks of the inset are the Cu$_x$O peaks while the downward peaks are from the FTO.
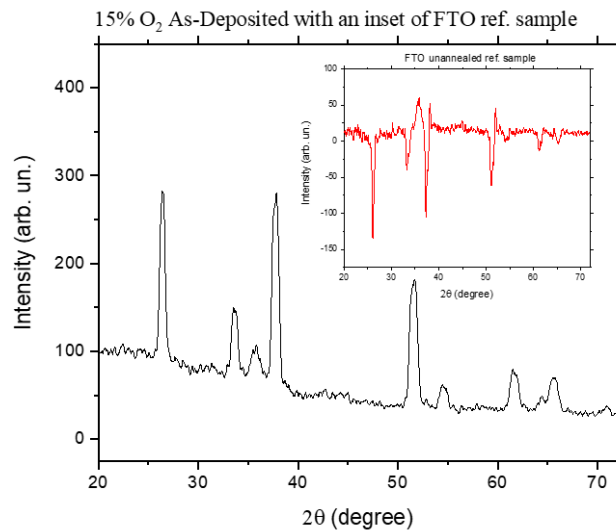


**Figure 5.14:** XRD peaks of the pristine thin film deposited at 15% $O_2$ partial pressure with an inset. The inset shows the difference between the $Cu_2O$ deposited layer and the FTO-coated layer. The peaks with positive intensity belong to the Cu$_x$O while the ones with negative intensity belong to the FTO of the substrates.
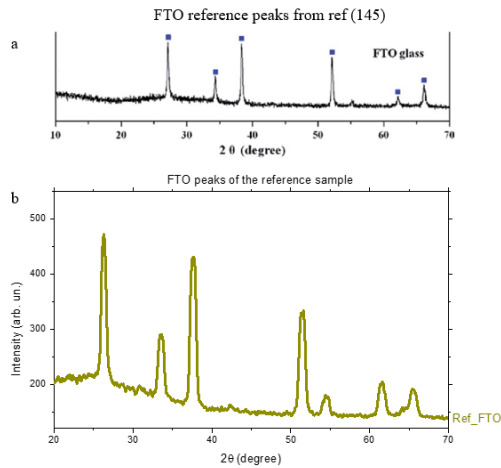
**Figure 5.15:** XRD reference spectra, panel a shows XRD peaks obtained from reference [145]. Panel b shows the FTO spectra of the substrates used for this project. All the peak positions from both panels are very similar though panel a is from 10-70° while panel b is from 20-70°.

The peaks of the FTO reference sample are not assigned, however; it is compared to a reference spectrum [145] as depicted in Fig. 5.15. The reference peaks are in the same positions as the peaks measured on our reference sample.

**Raman results**

Figure 5.16 presents the Raman spectra of the as-deposited thin films on Si and FTO that were placed side by side on the same substrate holder during deposition. Raman signals of pristine samples are very weak, and this results in spectra with low signal to noise ratio. However, the peaks are still visible, and their assignment is the same that is discussed in Section 5.1 and 5.2. When comparing the spectra obtained for 15% $O_2$ deposited on silicon (green) and on FTO (red), first of all we notice the intense silicon peak at 521 cm$^{-1}$ for the silicon sample, which clearly isn't present in the FTO sample. The characteristic peaks for copper oxide at 214 and 635 cm$^{-1}$ that are present in the silicon sample are slightly more pronounced in the FTO sample. Although some additional peaks can be observed in the FTO samples, these cannot be attributed to any copper oxide phase and are thus most likely from the FTO. In the sample deposited at 23% $O_2$ on FTO, the spectrum (in black) shows the same peaks at 313 and 624 cm$^{-1}$ as the blue spectrum, which was taken on the film on silicon. Furthermore, all the FTO spectra

also show a peak at approximately 536 cm$^{-1}$, which seems to be present in the silicon sample as well, although there it is obscured by the very intense silicon peak. This figure illustrates that the resulting thin films´ properties do not depend strongly on the underlying substrate, as long as the same deposition parameters can be guaranteed.
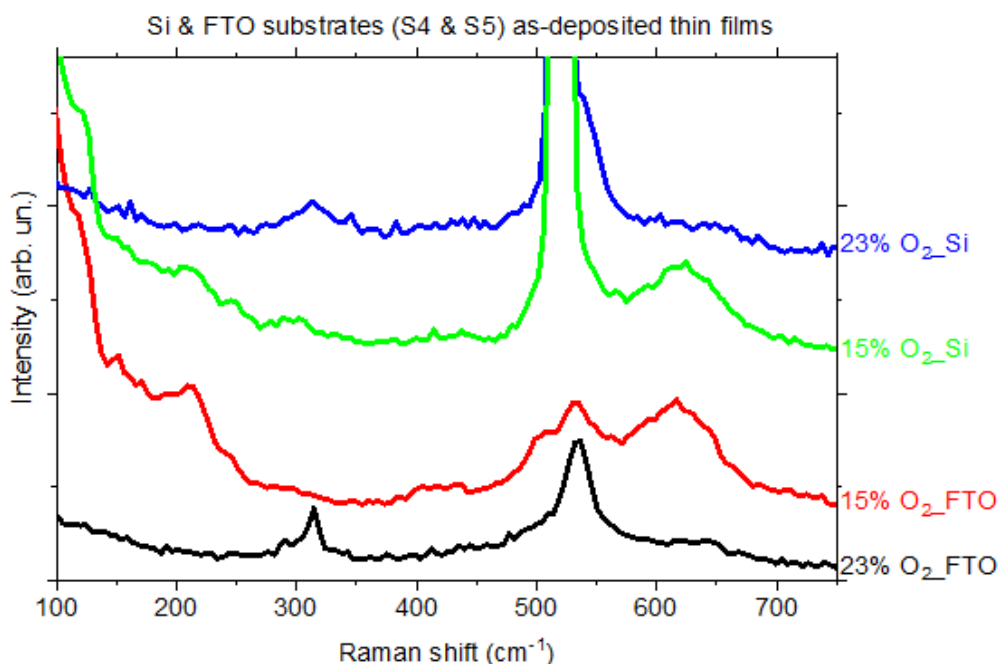


**Figure 5.16:** Raman spectra of the as-deposited thin films prepared on Si and FTO-coated substrates. As shown also in Figure 5.6, Raman signals of pristine samples are very weak. Therefore, here the spectra have been arbitrarily rescaled in order to enhance the visibility of the peaks.

In conclusion, films deposited on Si and on FTO with the exact same deposition parameters have rather similar properties. The slight dissimilarity of a higher O$_2$ percentage revealed by EDX for the deposition on FTO could be traced to a contribution from the oxygen in the FTO films. Therefore, it can be expected that thermal treatment of films on FTO would lead to similar results as thermal treatment on films on Si. To test this hypothesis, we performed a similar analysis as in the previous section, by annealing the films deposited on FTO at different temperatures, and verifying their structural and stoichiometric properties. Furthermore, thanks to the transparent substrate, these samples could also be used for optical transmission measurements. The results of all these studies are reported in the following two sections.

## 5.4 Investigation of Cu$_x$O thin films deposited on FTO substrates

This section examines the Cu$_x$O thin films deposited on to FTO-coated substrates at both 15% and 23% O$_2$ partial pressures and annealed at different temperatures. The characterization techniques employed here are SEM, XRD and Raman.

### SEM results

The SEM micrographs obtained at an acceleration voltage of 5.00 kV on the FTO samples are displayed in Fig. 5.17a. We observe pattern changes at every increase of the annealing temperature. The thermal treatment on the thin films results in changes in the microstructures such as appearance of bigger grains and a phase change as confirmed by the structural composition investigation performed by XRD and Raman. The reason for these changes is as explained in Section 5.1.
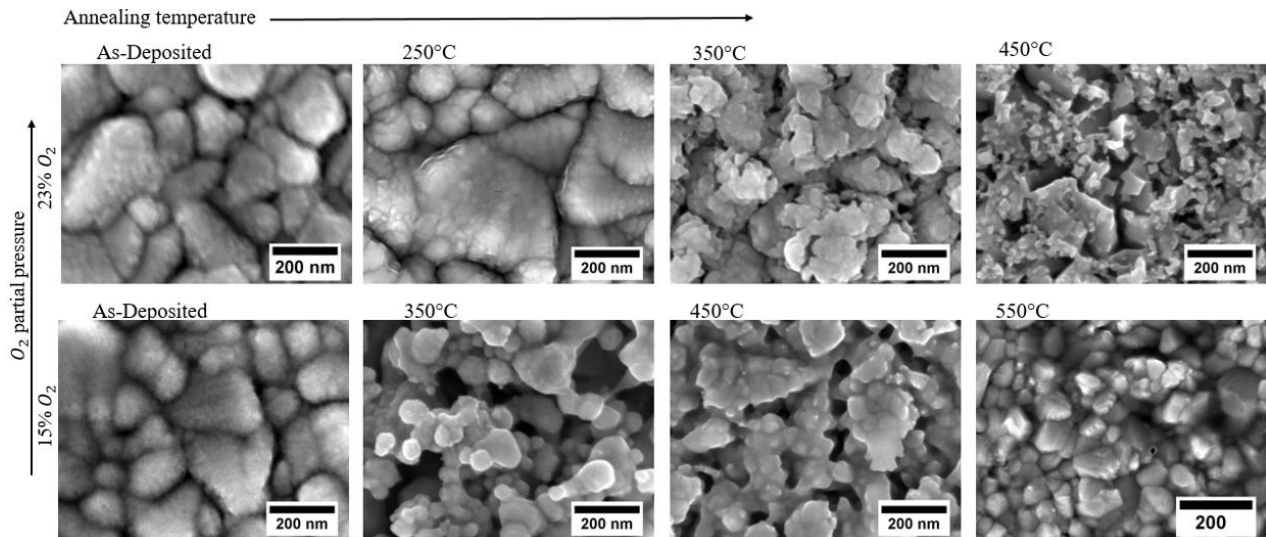


**Figure 5.17a:** SEM surface morphology of sputtered thin films onto FTO coated glass substrates. Top panels refer to deposition at 23% and bottom panels to 15% O$_2$ partial pressure. Annealing temperature increases from left to right.

We measured the thicknesses of the films by cross sectional SEM imaging, obtaining values of ~150 nm and ~157 nm for thin films sputtered at 15% and 23% O$_2$ partial pressure, respectively, as displayed in Fig. 5.17b.
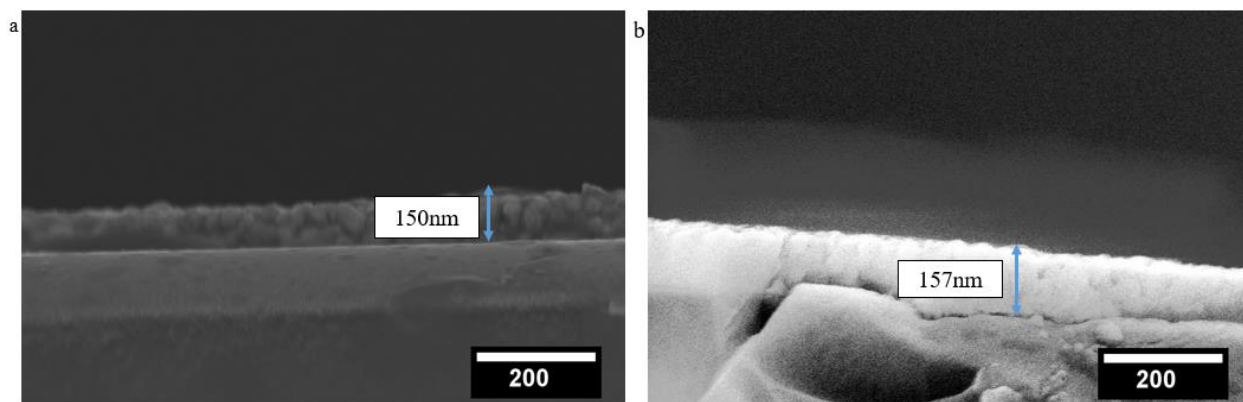
**Figure 5.17b:** SEM cross sections of sputtered thin films onto FTO coated glass substrates. Left and right panels refer to deposition at 15% and 23% $O_2$ partial pressure, showing a thicknesses of ~150 nm and ~157 nm, respectively.

## XRD results

For the XRD analysis, we used the same databases as in the previous sections. Figure 5.18 presents the thin films sputtered on to FTO-coated glass substrates.
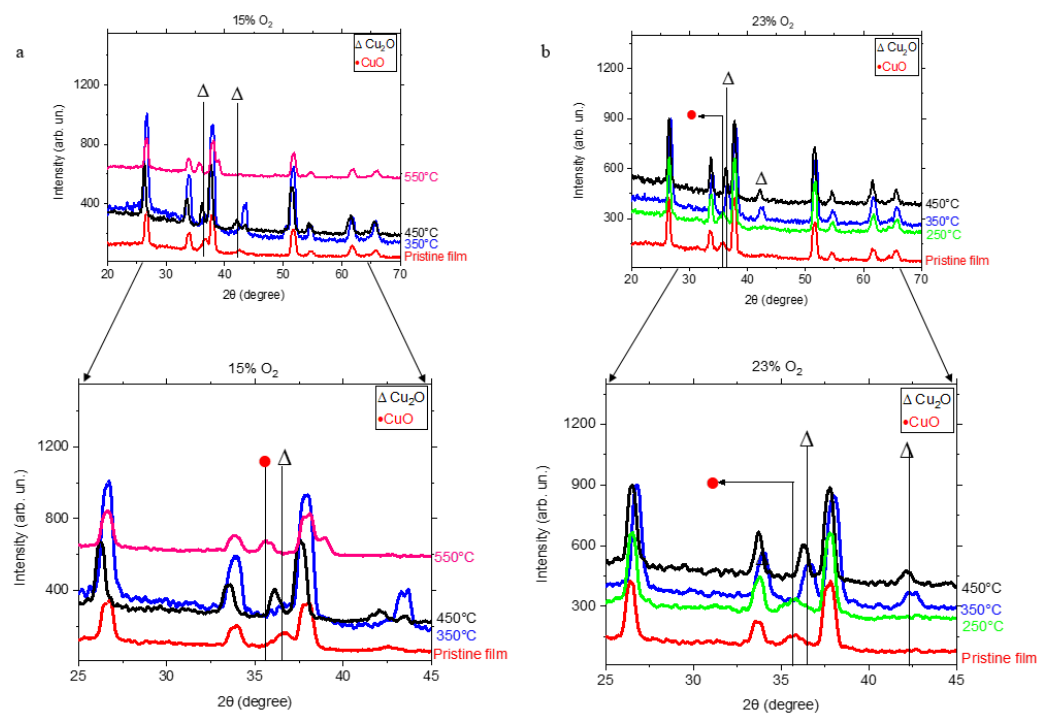


**Figures 5.18:** XRD patterns of nanoporous thin films sputtered onto FTO-coated glass substrates by RF-magnetron sputtering at 15% (panel a) and 23% (panel b) $O_2$ partial pressure. Triangles and circles indicate peaks attributed to

Cu$_2$O or CuO, respectively. The spectra are vertically shifted for clarity. Annealing temperature increases from bottom to top. The panels below are a zoom of the top panels. The black lines are drawn to show peak evolution.

The films grown at oxygen partial pressure of 15% reveal CuO monoclinic phase patterns through peaks at 35.85° (-111) when annealed at 550°C. The Cu$_2$O characteristic peaks at 2θ = 36.28° and 42.25° are assigned to planes of (111), (220) and are visible for the pristine film and the film annealed at 350°C and 450°C. The 23% percent oxygen partial pressure sample presented in Fig. 5.18b has the monoclinic phase reflections at 38.05° attributed to (-111) plane. The cuprous oxide signature peaks at 2θ = 36.16° and 42.56°C assigned to planes of (111) and (200) become visible at annealing temperatures of 350 and 450°C. These results confirm bi-oxides phases in both depositions and show the effect of annealing at high temperature. Every peak interpretation remains the same as discussed in Section 5.1, XRD results. The FTO layer from the substrate has many peaks competing with the Cu$_x$O thin films, making it difficult to differentiate these peaks (see the FTO reference sample peaks in Fig. 5.12 in Section 5.3). The cuprous oxide characteristic peaks at 2θ = 36.28°, 42.25°, 61.47° and 65.88° are assigned to planes of (111), (200), (220) and (221), respectively. The peaks attributed to cupric oxide monoclinic phase are at 38.05° and 51.45°, attributed to planes of (-111) and (111), respectively.

**Raman results**

Figure 5.19 shows the Raman spectra of films deposited onto FTO coated glass substrates at 15% and 23% oxygen partial pressure.
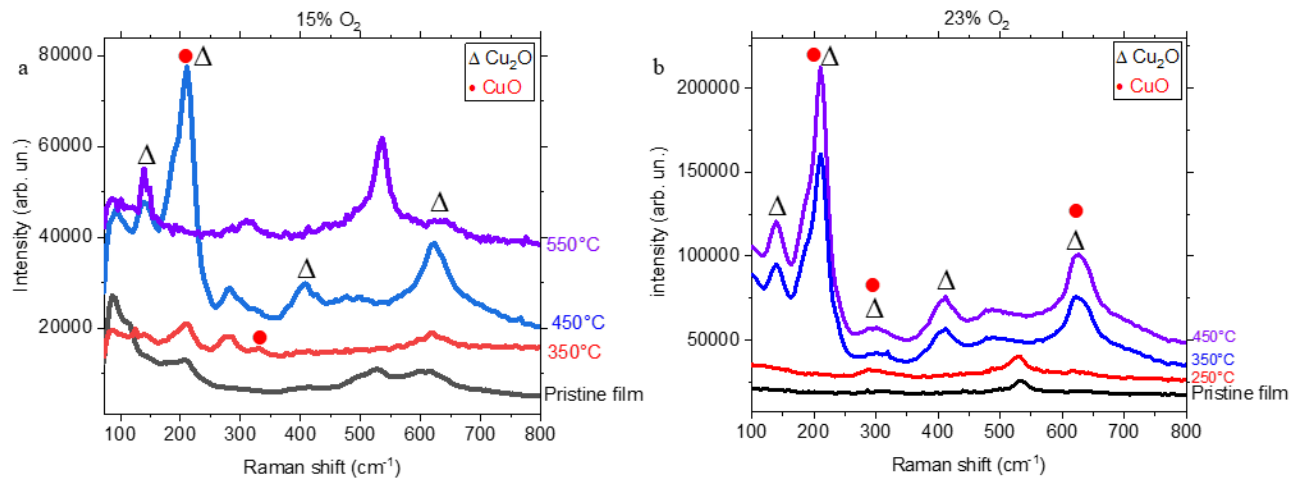


**Figure 5.19:** Raman spectra of nanoporous thin films sputtered onto FTO coated glass substrates by RF-magnetron

There are some prominent CuO Raman signatures appearing at 213 $cm^{-1}$ and at 298 $cm^{-1}$ for both oxygen pressures; the two peaks are most likely attributed to Raman first order modes of symmetry $A_g$ [94, 145]. As discussed in the interpretation of Figure 5.6, we cannot exclude that these modes belong also to $Cu_2O$. The mode at ~298 $cm^{-1}$ is present in all the spectra collected from samples annealed at different temperatures of the sample with 23% $O_2$ partial pressure. From the spectra of Fig. 5.19a taken on the 15% $O_2$ sample it can be seen that the intensity of the mode at 142 $cm^{-1}$ is lower in the pristine and 350°C sample, and becomes moderate at 450°C and 550°C. This peak at 145 $cm^{-1}$ can be assigned to phonons of symmetry $F_{1u}$ of $Cu_2O$ [94, 100, 138, 140]. The 213 $cm^{-1}$ mode is absent at 550°C, and this disappearance might be due to the conversion of CuO to $Cu_2O$ at higher annealing temperatures, as explained in Section 5.1. The annealed thin films at 350°C, 450°C and 550°C have a mode at 334 $cm^{-1}$ that could correspond to the $B_g$ mode of CuO [6, 125]. The peak at 412 $cm^{-1}$ is yet to be identified. The mode at 624 $cm^{-1}$ is assigned to $Cu_2O$ [146]; this peak increases in the 450°C sample and loses its intensity at 550°C.

In Fig. 5.19b, spectra of films deposited at 23% $O_2$ are shown. The moderate intensity mode at 142 $cm^{-1}$ appears only at the higher annealing temperatures of 350°C and 450°C [100, 138]. The peak at 635 $cm^{-1}$ appeares only at the higher annealing temperatures of 350°C and 450°C [6, 125, 143].

The phase transition also appears at high annealing temperatures of 350°C and 450°C, as observed in the results discussed in Section 5.1.

There are some peaks not identified, as they do not correspond to the symmetries of both cupric and cuprous oxides but we suspect that they could belong to either the metastable oxide of $Cu_2O_3$ or the paramelaconite $Cu_3O_4$ phases of the copper oxides as discussed in the references [84, 85, 86, 87] and the DFT studies of the three phases in ref. [96].

## 5.5 Optical Transmission results

The transmission of the samples deposited on FTO was studied using the SSEF UV-Vis spectrometer described in Section 4.6. The wavelength range is from 350-850 nm. The samples were annealed at 250, 350, 450 and 550 °C. These measurements on the FTO samples are presented here for the first time. The transmission results in Fig. 5.20 show that both films grown at 15% and 23% $O_2$ partial pressures (pristine and annealed) all have lower transmission in the ultraviolet region and higher transmission in the visible to near IR region of the spectra, with the exception of the sample in panel a annealed at 350°C. This sample was not visually transparent and was heavily scratched. The optical image of the samples is display in Fig. 5.21.
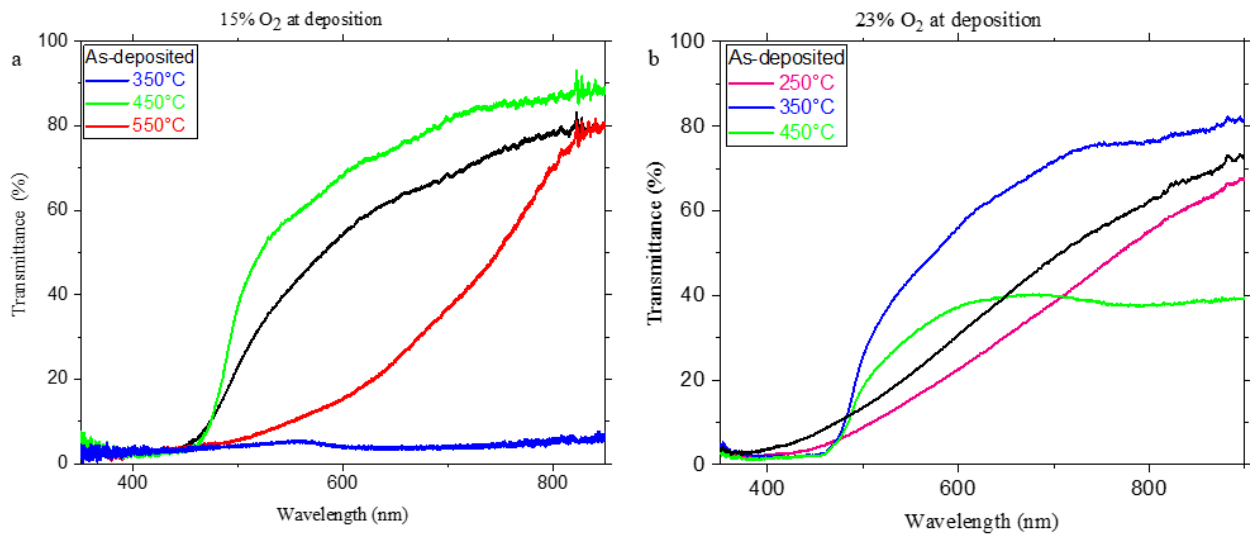


**Figure 5.20:** Transmission measurements for the deposition onto glass substrates. Panel a refers to deposition at 15% partial pressure and panel b to 23% $O_2$. The two panels show lower transmission in the ultraviolet to visible region and higher transmission in the near IR region of the spectra. The similar colors from panels a and b show samples annealed at the same temperatures while other colors correspond to different temperatures.

The optical band gap from the ultraviolet-visible light spectra was determined from the transmission measurement by plotting $(\alpha h v)^2 vs (h v)$ and linearly extrapolating the straight line to the x-axis. The 2 in the exponent is for the direct bandgap calculations, while for the indirect band gap plot the exponential of 2 is replaced by ½; $h v$ is the energy of incident photons. The absorption coefficient $\alpha$ is given by $\alpha = \frac{1}{d} In \frac{1}{T}$, where $d$ is the thin film thickness and $T$ is the transmission. The wavelength was converted to energy using the relation E (eV) = 1240/wavelength (nm).

We recorded the transmission spectra of each sample and tabulated the results of the analysis in table 5.2, including the extrapolated direct optical band gap.

15% Oxygen partial pressure samples    23% Oxygen partial pressure samples
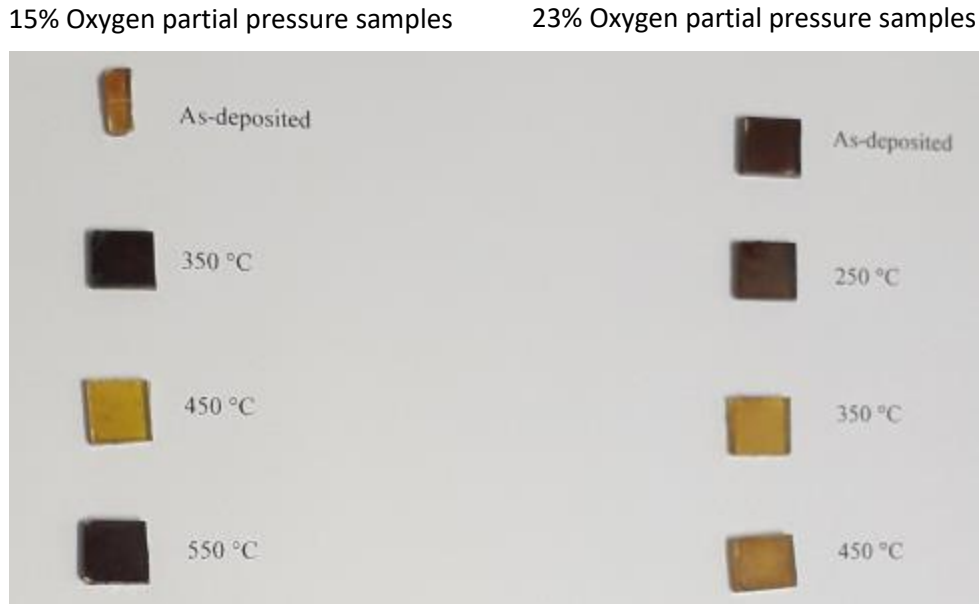


**Figure 5.21:** Photo of the FTO-coated samples used for the absorption measurement. The right is 15% and the left is 23% oxygen partial pressures.

Deposition at 15% oxygen partial pressure

a

| Temperature (°C) | Transmission (%) | Extrapolated bandgap (eV) |
|---|---|---|
| RT | 80 | 2.49 |
| 350 | Nil | Nil |
| 450 | 90 | 2.51 |
| 550 | 88 | 2.10 |

Deposition at 23% oxygen partial pressure

b

| Temperature (°C) | Transmission (%) | Extrapolated bandgap (eV) |
|---|---|---|
| RT | 66 | 2.40 |
| 250 | 68 | 2.31 |
| 350 | 81 | 2.49 |
| 450 | 39 | 2.48 |

**Table 5.2:** Results of the maximum-recorded transmission percentages and the linearly extrapolated direct optical band gap values. The left side of the table refers to deposition at 15% $O_2$ and the right side to 23% $O_2$ partial pressure. The 350 °C in panel a, has no result hence the Nil.

Figures 5.22 and 5.23 depict the extrapolated band gap for both cases of direct and indirect semiconductors for the thin films grown at 23% oxygen partial pressure as a

representative sample. The 15% oxygen required more investigations to understand the acquired results hence will not be discussed in this work. Meanwhile, for $Cu_2O$ theband gap is expected to be direct and have a value of 2.1- 2.62 eV [3, 5, 77, 93], for CuO it's still being debated if it's a direct or indirect band gap, while band gap values of 1.21-1.5eV [69, 82, 83] have been reported. The semiconductor direct band gap extrapolation confirms the presence of $Cu_2O$ phase in the pristine films and all the annealed thin films, since the extracted band gap values correspond to the $Cu_2O$ band gap. Furthermore, the indirect plots show some lower band gap values at 1.68ev and 1.31eV for the as-deposited film and lowest annealing temperature of 250 °C respectively. This could indicate the existence of CuO thin films, thus the bi-oxide phase co-existence as seen in our XRD and Raman analysis. The absence of the indirect band gap in the higher annealing thin films shows that the CuO phase is absent.
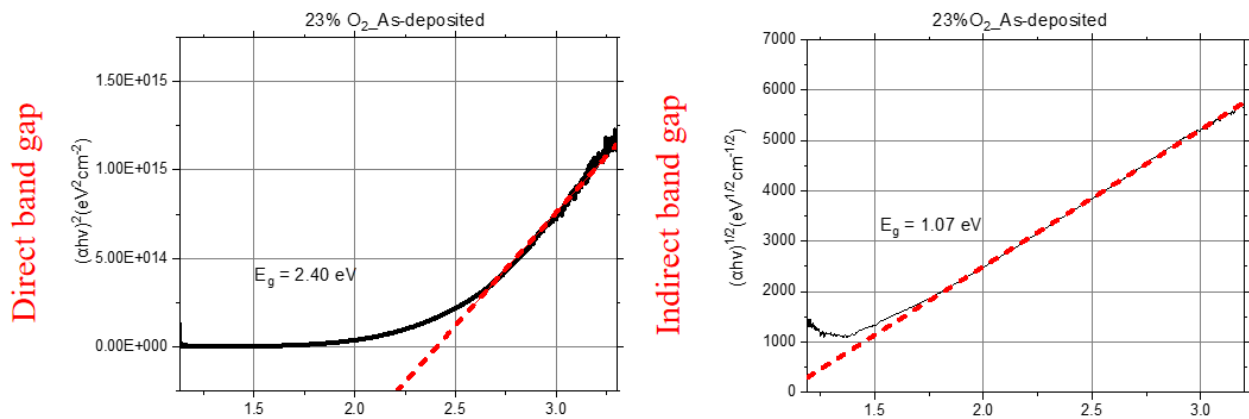


**Figure 5.22:** Optical band gap of the As-deposited thin films of $Cu_xO$ grown at 23% oxygen partial pressure onto glass substrates. Panel a, assumes the $Cu_xO$ as a direct band gap semiconductor and panel b as an indirect semiconductor. The red dashed lines are linear extrapolations of the straight path segment of the Tauc's plot.
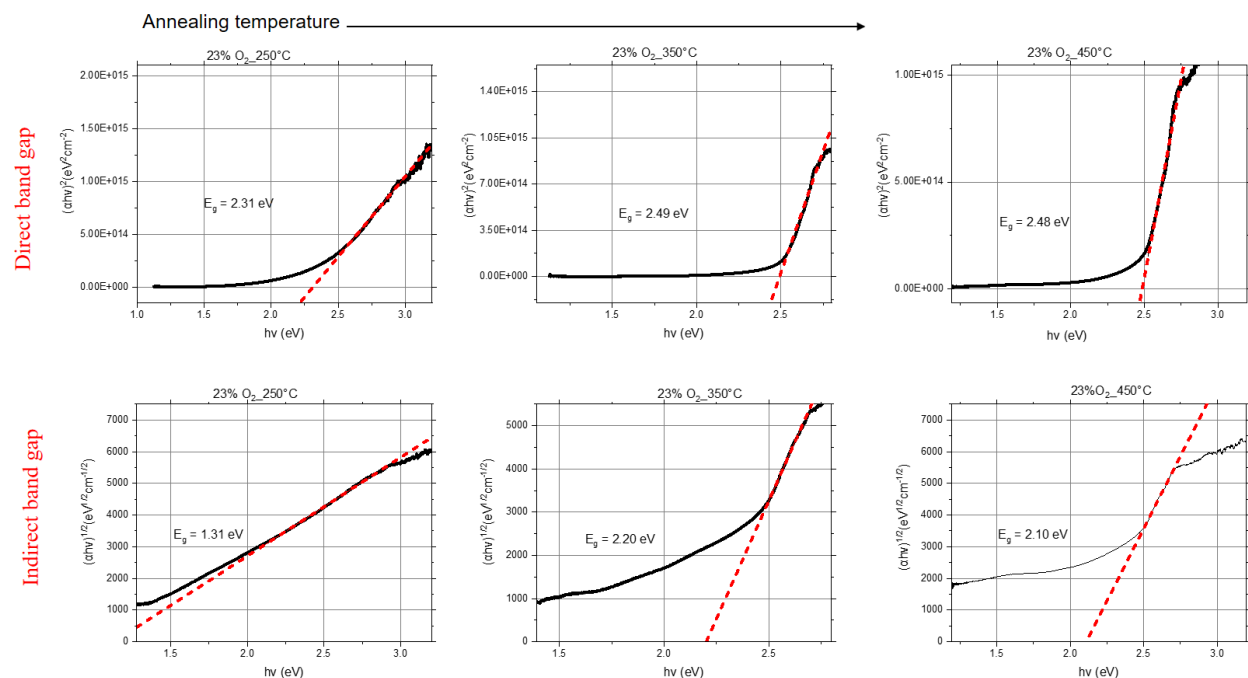
**Figure 5.23:** Optical band gap of the thin films of $Cu_xO$ grown at 23% oxygen partial pressure on glass substrates and annealed. The temperature of the thin films increases from left to right. The top panel assumes the $Cu_xO$ as a direct band gap semiconductor and the bottom panel as an indirect semiconductor. The red dashed lines are linear extrapolations of the straight path segment of the Tauc's plot.

In conclusion, the transmission results show the transmittance of the grown thin films in the spectral region of 350-850 nm. The transmission in the visible region of the spectra, shows the grown thin films are good substrates for $Ga_2O_3$ in making dye senisitized solar cells. The result also pointed out the co-existence of the bi-phase of the copper oxide, as well as the transition to $Cu_2O$ under annealing. This further confirms that annealing is a viable pathway to obtain thin copper oxide films.

## 5.6 Investigation of aging effects via AFM/KPFM and SEM techniques.

In this section, we present the aging effect of the samples several months after storage at ambient temperature. The techniques employed for the investigation are SEM and AFM/KPFM. Prior to this investigation, we did a lot of literature search and very few studies on the stability and aging of copper oxides were available [79, 96] and to the best of our knowledge none has

reported the crystallite growth that is peculiar to films grown on Si substrates, as we are showing in this section.

With the purpose of observing the material's durability in view of its photovoltaic applications, we investigated the aging effects on the thin films deposited on both the Si and FTO substrates. This was done by comparing AFM, KPFM and SEM images taken immediately after deposition (see, e.g., Figures 5.1 and 5.3 for the deposition on Si substrate) with those obtained after several months aging period at ambient conditions and shown in this section. Figure 5.24 shows the AFM and KPFM images of aged, non-annealed samples deposited on Si at 15% oxygen partial pressure (15 months aging, bottom panels) and at 23% oxygen partial pressure (21 months aging, top panels). In the 15% samples, AFM and KPFM images show the existence of crystallites with a dendritic pattern, and a different pattern for the 23% oxygen. Both were not present immediately after deposition.
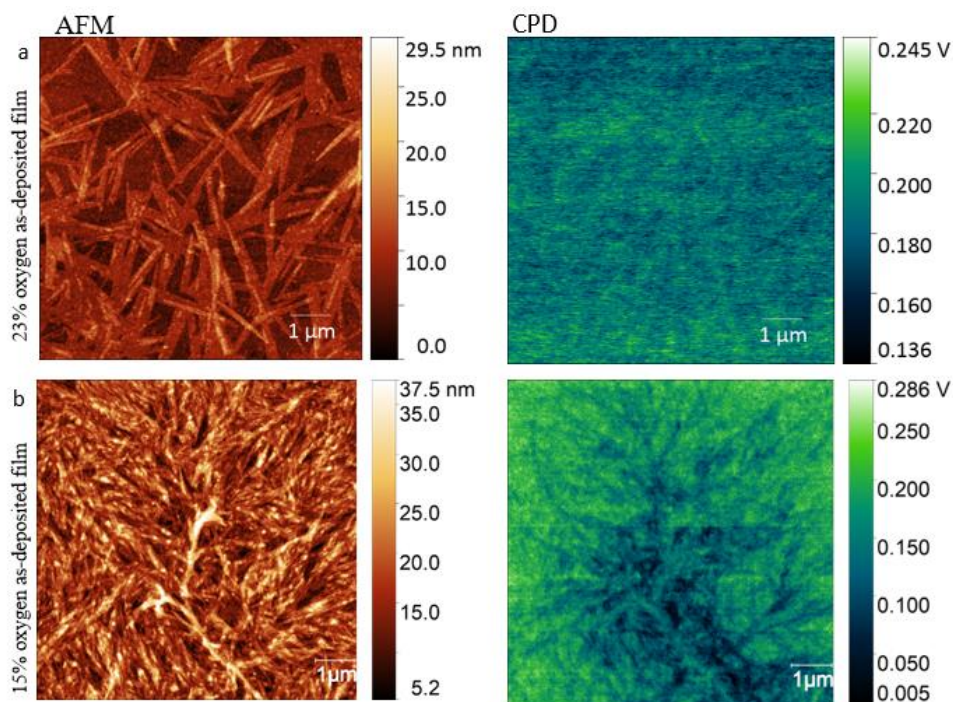


**Figure 5.24:** AFM (left) and CPD (right) images of both non-annealed films deposited at 23% $O_2$ (top panels or a) and 15% $O_2$ (bottom panels or b) showing crystallites growth. Top panels correspond to 21 months aging period and bottom panels to 15 months aging period. Samples were stored at ambient conditions. None of these crystallites were observed in the samples when they were imaged immediately after deposition.

Aging effects were also found in the samples annealed at low temperature. As an example, we present in Fig. 5.25 AFM and KPFM measurements performed on the thin film deposited at 23% $O_2$ partial pressure and annealed at 250 ℃. These results indicate the presence of the crystallites also on the surface of this sample, though they were not present immediately after deposition.
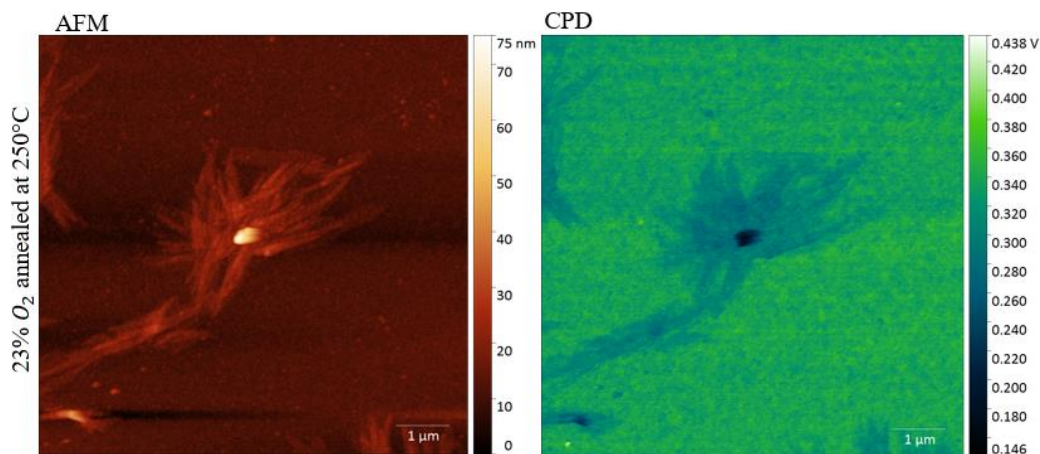


**Figure 5.25:** AFM and CPD images of the film deposited at 23% $O_2$ and annealed at 250 ℃ taken 21 months after deposition and showing crystallites growth. The sample was stored at ambient conditions. None of these crystallites were observed in the sample when it was imaged immediately after deposition.

In addition, we investigated the effect of the aging time and original partial pressure conditions during deposition. To this end, we compared the morphology of the crystallites on films deposited under different $O_2$ partial pressure conditions and aged for the same duration (SEM micrographs in Fig. 5.26 a and b). Within the same aging period, the crystallites exhibit different patterns of growth depending on the deposition conditions. Similarly, we have compared the morphology of the crystallites on films deposited under the same $O_2$ partial pressure conditions and aged for the different duration (SEM micrographs in Fig. 5.26 b and c). In this case, the crystallites exhibit a further evolution over time.
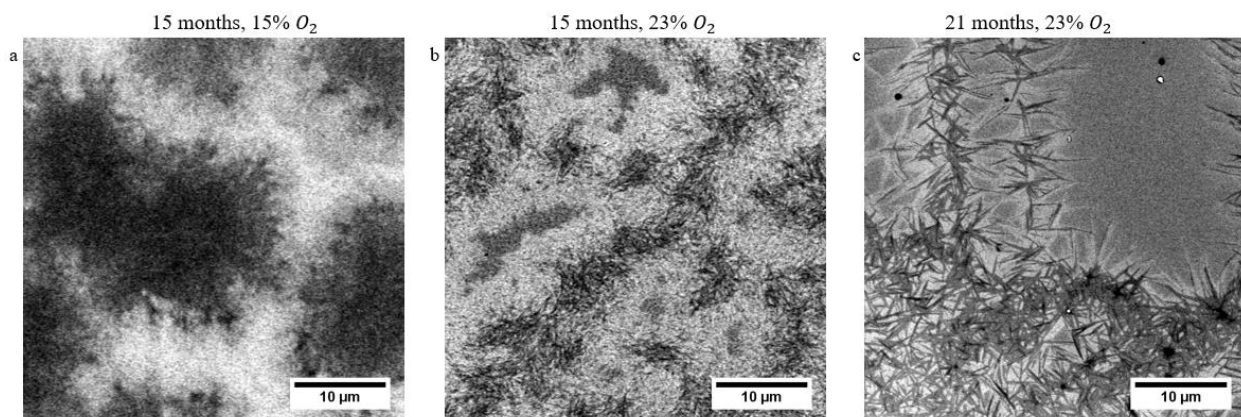
**Figure 5.26:** SEM images of pristine films deposited onto Si substrates at 15% $O_2$ (panel a) and 23% $O_2$ (panels b and c) showing crystallites growth. Panels a and b correspond to 15 months of aging period and panel c to 21 months aging period. Samples were stored at ambient conditions. The samples shown in panels b and c do not have the same pattern of crystallites as in panel a. Samples in panels a and b have the same aging period, but they exhibit crystallites with different size and pattern. None of these crystallites were observed in the samples when they were imaged immediately after the deposition.

The samples annealed at higher temperatures did not show this crystallites growth, even 28 months after their deposition, indicating that the higher annealing temperatures help to enhance the stability of these films, in addition to the effects on the copper oxide phases that we have already discussed. This investigation clearly exposes the instability of copper oxide when not subjected to high temperature vacuum annealing. This aging phenomenon is not unique to a specific oxygen level during the film deposition, since it occurs for both oxygen partial pressures. We recommend more investigations and studies in this regard, as very limited literature is available on the aging of copper oxide. Interestingly, to the best of our knowledge, no existing studies have shown crystallites growth as a sign of copper oxide instability, despite its high relevance for the development of long-standing photovoltaic devices.

Finally, it is worth stressing that while the films deposited on Si substrates show some crystallites growth on the pristine and lower annealing temperatures of 250°C, the thin films deposited onto FTO substrates did not show any sign of aging effects after 19 months of storage in ambient conditions like the Si samples.

In conclusion, we found that the pristine samples deposited on Si and those annealed at low temperatures displayed unwanted crystal growth when exposed to atmospheric conditions

for a few months. Quite remarkably, annealing the samples prevented this unwanted growth. Namely, the SEM and AFM studies prove the stability of the films annealed at temperatures equal or higher than 350 °C. The reason for the absence of crystallites growth in the samples deposited on FTO is still under investigation. However, this absence suggests that deposition onto FTO substrates could be a viable (and cheap) alternative to obtain highly stable $Cu_2O$ thin films.

# Conclusions

In this thesis, we have described the deposition and characterization of $Cu_xO$ thin films by RF magnetron sputtering onto Si and FTO-coated substrates. The main challenge related to the deposition is that the oxygen content required to obtain copper oxide films with a pure phase is yet to be standardised. Indeed, all the reviewed literature agrees on the difficulty in identifying the quantity of oxygen required for single-phase formation. Moreover, in our experience, one technical issue was also the reproducibility, as we have shown that two depositions with the same nominal oxygen content can result in a slightly different effective oxygen content in the obtained film. In summary, a successful deposition processes in terms of reproducibility requires attention to all the deposition parameters inclusive of the chamber pressure.

We looked at an alternative route for producing pure phase $Cu_2O$ from the $Cu_xO$ and/or CuO mixed phases formed at deposition by exploring the annealing mediation route. The annealing was performed in vacuum at the temperatures of 250, 350, 450, 500 and 550°C on samples all cleaved from the same deposition. This alternative post-deposition treatment, i.e. vacuum annealing, worked well for thin films annealed above the critical temperature of 350 °C. Namely, in this case, we were able to achieve single $Cu_2O$ phase thin films, as CuO reduced to $Cu_2O$. We suggest that, in the future, in-situ annealing in the XPS chamber should be compared to our route of annealing after deposition. In the latter case, the samples are (unavoidably) exposed to atmospheric conditions outside the deposition chambers. Furthermore, the storage conditions before annealing can also be important and should be further investigated. The advantage of our method is that we were able to cleave samples after deposition, while the in-situ annealing would not give this opportunity and, therefore, annealing would be performed on samples resulting from different deposition processes. This is relevant in this research phase in order to investigate the effect of the different parameters independently.

The Si and the FTO-coated glass substrates were prepared systematically for the deposition. The characterization of the deposited thin films was performed always in the same order, as described in the following.

The SEM measurements of the cross section of the thin films revealed the film thicknesses. With increasing annealing temperature, we observed by top viewing SEM imaging the formation of large grains and the presence of porosity in the thin films on both Si and FTO substrates. The EDX provided the quantitative composition of the contributing elements (Cu and O) in the thin films; most importantly, it showed a decreased oxygen content in the annealed thin films which is also another hint pointing towards the formation of $Cu_2O$. The thin films deposited onto FTO substrates contained oxygen higher than the nominal oxygen partial pressure at deposition, the extra oxygen content was attributed to contribution from the FTO ($SnO_2$-F) layer the oxide of the coated layer as pointed out by the EDX analysis.

The AFM measurements showed the topography of the films. We found that the pristine samples and those annealed at low temperatures displayed unwanted crystallites growth when exposed to atmospheric conditions for a few months. Quite remarkably, annealing the samples at high temperature prevented this unwanted growth. The SEM and AFM prove the stability of the films annealed at temperatures equal or higher than 350 °C for the deposition on Si substrates. Interestingly, the absence of crystallites in the films deposited on FTO suggests that deposition onto these substrates could be a viable (and cheap) alternative to obtain highly stable $Cu_2O$ thin films. We recommend more studies/research in this regard, as very limited literature is available on the aging of copper oxide and, to the best of our knowledge, no existing studies have shown crystallite growth as a sign of copper oxide instability, despite its importance for the development of long-standing photovoltaic devices.

The KPFM measurements showed the homogeneity of the thin films and suggested that the CuO segregates and vanishes at annealing temperatures above 500 °C.

The techniques we employed for structural investigation (XRD and Raman spectroscopy) gave consistent results, showing that the lower oxygen pressure during deposition favours the formation of $Cu_2O$. Instead, at higher oxygen pressures, the oxides co-exist and/or only the CuO phase exists. Furthermore, both XRD and Raman spectroscopy further corroborated the transition from CuO to $Cu_2O$ when the film underwent vacuum annealing. In addition, the good

homogeneity of the grown thin films was assessed using spatial dependent Raman spectroscopy. On the other hand, the interpretation of the XRD results of the films on the FTO-coated layer substrates were difficult due to the competing signal stemming from the FTO and the deposited $Cu_xO$. Therefore, we recommend future studies on other coated substrates as well.

Concerning the optical properties, the deposited films have lower transmission in the ultraviolet region and higher transmission in the visible region to near IR region of the spectrum, suggesting that they can be good substrates for dye sensitized solar cells.

In conclusion, we investigated the most important properties of the deposited films, discussing their dependence on deposition parameters, post-deposition annealing treatment, and aging time. All the exploited investigation methods were complementary and the obtained data and analysis led to coherent results. This work could aid in the reliable and reproducible production of high quality $Cu_2O$ films on Si and on FTO substrates for photovoltaic applications.

# Outlook

The scope of this project was to develop a suitable nanoporous p-type material with a large band gap in the optically transparent wavelength range for dye-sensitized solar cells. This can then be used in the so-called tandem solar cells, which have higher operational voltages of 1.5V and a much better light absorption than NiO, the most commonly used material in the dye sensitized solar cells so far. NiO has some disadvantages, mainly due to defects. A promising alternative is $Cu_2O$, which has a band gap of about 2.5eV and is slightly p-type due to copper defects. These properties, among others, make $Cu_2O$ suitable for solar cells. However, the efficiencies achieved so far are very low. This is mainly because the analysis and understanding of the material properties and their influence on the solar cell device performances are still at an early stage. On the other hand, this is exactly the reason for which overall improvement potentials are expected. Hence, we provided our contribution to the deposition and thorough investigations of the $Cu_2O$ thin films. There are several very promising theoretical predictions for the use of these and similar non-toxic and abundant materials. Further improvements are expected, among others, from the use of mixed metal oxides such as $CuGaO_2$, but here the material properties are even less investigated. In the near future, we will attempt the development of an RF-magnetron sputtering process to produce the ternary compound of $CuGaO_2$. To optimize the material properties, key parameters such as high porosity (to obtain a high surface-to-volume ratio), large band gap (optically transparent in the visible range), p-type conductivity with high charge carrier concentration are to be optimized in order to finally produce a functional solar cell device.

Finally, based on the experience we have developed in the deposition of copper oxides, we believe that for both the copper oxides and the mixed copper-gallium-oxides, the procedure for deposition has to be impeccable for reproducible realisation of metal oxides. For instance, also the loading procedure of the sample in the chamber can have an impact on the obtained film and, therefore, it should be perfomed always in tha same manner. In summary, it is very important to maintain a clear line up procedure from start to end. The flow of gases has to be controlled systemically too, e.g. if the oxygen was the first gas introduced into the chambers

before the Argon gas then this sequence has to be maintained for achieving reproducible results for subsequent depositions.

Furthermore, in our study, the annealing was conducted in vacuum after deposition and the samples were taken out of the chambers and prepared for the annealing: This is a reasonable procedure, with some advantages as discussed in Chapter 5, but we suggest to explore also in-situ annealing during deposition, which could be better to avoid atmospheric interference especially as a growth route for pure copper oxide phase.

The studies conducted on aging effect gave a distinctive result. Further studies should be conducted in this regard, as very limited literature is available on the aging of copper oxide and no existing studies, to the best of our knowledge, have shown crystallite growth as a sign of copper oxide instability, despite its importance for the development of long-standing photovoltaic devices. Further insight into the aging studies will be gained by investigating these samples also by Raman spectrometry and XRD to see the differences between prestine samples and the ones after aging.

# Additional Figures



**Figure 6.1:** The photos of Si substrates for 23% oxygen partial pressure depositions. The samples were labeled S1, S2 and S3 as arranged in the figure. Right on top of the sample I is the Si reference sample.
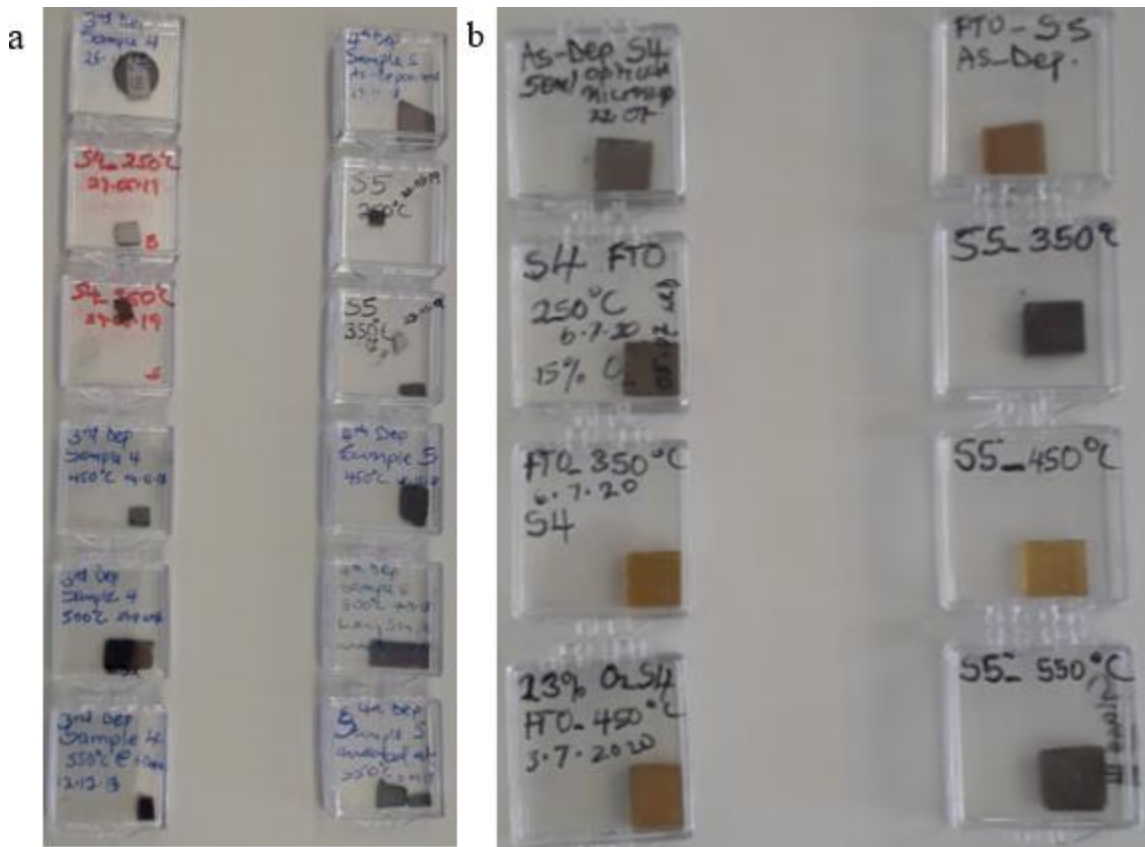
**Figure 6.2:** The photos of S4 and S5 samples. Panel a is deposition onto Si substrates. Panel b is deposition onto FTO-coated glass substrates. The left of both panels a and b are 23% $O_2$ the right of the panels are 15% $O_2$ partial pressure. The samples were placed side by side on the substrate holder, each of Si and FTO together for sputtering.
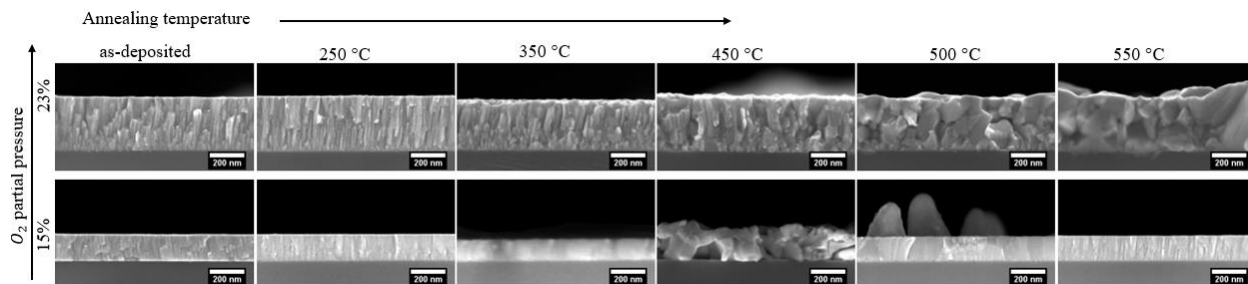


**Figure 6.3:** SEM cross sections of sputtered thin films on Si substrates deposited at 15% (bottom panels) and 23% (top panels) $O_2$ partial pressure. Annealing temperature increases from left to right.
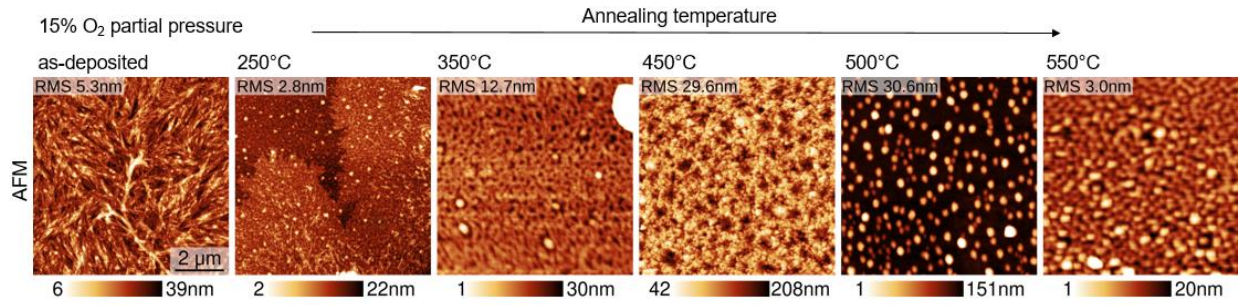
**Figure 6.4:** AFM images of sputtered thin films on Si substrates deposited at 15% $O_2$ partial pressure. Annealing temperature increases from left to right.

**Publications**

- **M. Umar**, M.Y. Swinkels, M. De Luca, C. Fasolato, L. Moser, G. Gadea Diez, L. Marot, T. Glatzel and I. Zardo. *$Cu_xO$ thin films deposited on FTO substrates*, under preparation (2020)
- **M. Umar**, M.Y. Swinkels, M. De Luca, C. Fasolato, L. Moser, G. Gadea Diez, L. Marot, T. Glatzel and I. Zardo. *Morphological and stoichiometric optimization of $Cu_2O$ thin films by Deposition Conditions and Post-Growth Annealing*, just accepted in Thin Solid Films (2021)
- Yuri P, Rybakov, **Medina Umar**, Muhammed Iskandar (2019) Mechanical Properties of Carbon Nanotubes in a Chiral Model of Graphene*, J.Mech.Cont.& Math. Sci.*, Special Issue-1, March (2019) pp 420-428 Doi.org/10.26782/jmcms.2019.03.00041

# Acknowledgements

The quest to learn and the ability to comprehend are two different things.

Considering going for a PhD was an internal fight for me. In the end, the quest to learn overshadowed everything else and here I am today with so little words to show my appreciation to everyone who helped me.

My incessant gratitude to Prof. Dr. Ilaria Zardo, who gave everything to help me find my feet. Thank you Ma for not giving up on me. In you, I found my Angel. You are blessed beyond measures.

Dr. Thilo Glatzel, I appreciate you. I hope I pick your patience and excellent working relationship with others for my working life.

I thank Prof. Dr. Ernst Meyer for accepting me as part of the Nanolino Group.

I am thankful to Barbara Kammerman and Astrid Kalt. The duos are wondeful.

To my immediate supervisor Milo Yaro Swinkels (Gentle Giant), words are not enough to thank you for the time you devoted to see me through the years.

To my lifeline, Marta De-Luca, I am glad I met you, thank you for nurturing me scientifically and for always being there for me, from material gifts to housing me in Roma…Grazie Mille. The Zumba dance sessions were the most social activities I had, they were truly relaxing, thank you for introducing me… I almost forgot this unique activity in Basel.

To Claudia Fasolato thank you for the shoulders, you gave me especially when I was bereaved. Your positive aura and cheerfulness I will always cheerish. The evenings at the Rhein were pleasurable moments and the breakfast at Fiumicino aeroporto was super.

Alessio Campo and wife, I appreciate your assistance both for the scientific and personal matters. I will miss Sicilian sweets and almond nuts. Thank you for being a Brother. Hoping to visit Sicilly someday.

Oliver Braun, thanks for the ice cream at my interview and the encouragement.

Lukas Gubser, even when you don't talk I know you care.

Gerard Gadea Diez, I appreciate the science and the silent friendship thank you.

And the group got bigger, I appreciate everyone of you, Begona Abad Mayor, Nicola Forrer, Diego de Matteis, Yashpreet Kaur, Nadine Gächter, Giulio de Vito, Tsai-Hsuan Hsieh, Grazia Raciti and the Baby of the house, Arya Chaitanya you are welcome. Thank you all for all we shared. The memories will linger on, the Phononics group is home away from home for me. I enjoyed all of the Barbecues especially the one at my interview, I felt the bond, the lunchs, dinners and the Christmas dinners, I wish for one more time (Don't call me Oliver Twist). To see, participate and eat freshly baked pizza was an experience and that was right in my Prof's home with her amazing family...sure, that was a homily touch to the group, not every student

will experience this warmness in their study life, so I am glad for the opportunity. In these three memorable years, more than half the time Prof. Zardo shared her lunch with me, I will miss this special love (tears roll down my cheeks). Whatelse can I possibly ask for that I didn't get. Once again thank you ma.

Nanolino group, thank you: Laurent Marot for the sputtering, scientific discussions and the sputtering machine photo, Roland Steiner for both the science and your friendship (sorry that I couldn't continue with the skiing practice), Lucas Moser for helping with the depositions. Marco Zutter for the AFM, Antoine Hinaut & Alexina Ollier for the long winter hike and Carl Drechsel who is always looking after everyone, Rémy Pawlak, Sebastian Scherb, Guilherme de Vilhena, Philipp D'Astolfo, Kunal Soni, Rodrigo Antunes, Jung-Ching Liu, Fabien Sanchez, Zhao Liu, Yves Pellmont and Urs Gysin. The fun out there in the mountains and the music night, the memories with you all I will keep. Alexina thanks for making out time for my hair do.

I appreciate all the Ladies from the Physics Women Networking Event, Unibasel.

Giuilo Romagnoli, thank you for helping out with the Glass Diamond Cutter and also Patrick, from the general workshop.

I am indebted to Prof. Dr. J. S. A. Adelabu of University of Abuja, Prof. Dr. Yu. P. Rybakov and Prof. Dr. Elena, Golubovskaya (RUDN).

Annie, thank you so much for your kindness, living together is so much fun and I appreciate your life experiences you shared with me. I will miss the homemade cookies and cakes.

My cute friend Miss Katerina M. Prechtel, I appreciate your love and the gorgeous smiles.

The Mandukas, Onedibes, Blooms, Ferraros and Sandra your friendship I will always appreciate and other members of BCF family not mentioned.

Some special people exist in my life: Henry H. A. Oboro, thank you for the helping hand you gave when I needed it most... I wish you all of Life's happiness. Engr. Dr. C. C. Oyeka thank you for helping me see far. Dr. O. O. Osusu, your spiritual guide and encouragement I will always be thankful. Usman Osuma Adamu thank you for always checking on me, Mrs Uche Okoye and her family thanks for your love and care. Hon. Peter Iziogie Aguele congratulations on your 'big' win. I am happy for you. To my family and friends, thank you all for the immense support.

Along came Rt Hon. Yusuf Suleiman Lasun. Thank you for everything... God bless you more.

<div align="center">OHOMORIHI MAKU AVO.</div>

# Bibliography

[1] C. N. Bonvee, "Intuitions and Summaries of Thought,," in *Intuitions and Summaries of Thought,*, vol. 2, New York, 1857, p. 139.

[2] Smithsonian Institution. Annual report of the Bureau of Ethnology, "mithsonian Institution report," 1989.

[3] L. Guo, M. Zhao, D. Zhuang, M. Cao, L. Ouyang, X. S. R. Li and G. Z, "Influences of CuO phase on electrical and optical performance of $Cu_2O$ films prepared by middle frequency magnetron sputtering," *Appl. Surf. Sci.,* vol. 359, p. 36–40., 2015.

[4] C. Azanza Ricardo, M. D'Incau, M. Leoni, C. Malerba, A. Mittiga and P. Scardi, "Structural properties of RF-magnetron sputtered $Cu_2O$ thin films," *Thin Solid Films,* vol. 520, p. 280–286, 2011.

[5] J. Sohn, S.-H. Song, D.-W. Nam, I.-T. Cho, E.-S. Cho and J.-H. Lee, "Effects of vacuum annealing on the optical and electrical properties of p-type copper-oxide thin-film transistors," *Semicond. Sci. Technol.,,* vol. 28, no. 1, p. 015005, 2013.

[6] V. S. Levitskii, V. I. Shaplovalov, A. E. Komlev, E. S. Shutova, , "Raman spectroscopy of copper oxide films deposited by reactive magnetron sputtering.," *Technical Physics Letters,* vol. 41, p. 1094–1096, 2015.

[7] R. A. José and M. Fernàndez-Gracia, Synthesis, properties and application of oxide nanoparticles,, R. A. José and M. Fernàndez-Gracia, Eds., New Jersey: Whiley, 2007.

[8] C. Noguera, Physics and chemistry at oxide surfaces;, U.K: Cambridge University Press, 1996.

[9] V. E. Henrich and P. Cox, Surface Chemistry of Metal Oxides, Cambridge: Cambridge University Pres, 1994, pp. 91-94.

[10] R. Wyckoff, Crystal structures, 2nd edition ed., New York: Wiley, 1964.

[11] S. Srivastava, M. Kumar, A. Agrawal and D. S. K., "Synthesis and Characterization of Copper Oxide nanoparticles," *Journal of Applied Physics (IOSR-JAP) ,* vol. 5, no. 4, pp. 61-65, 2013.

[12] A. S. Zoolfakar, A. R. R, J. A. Morfa and P. O. a. K.-z. K. O'Mullane, "Nanostructured copper oxide semiconductors: a perspective on materials, synthesis methods and applications," *Journal of Materials Chemistry C,* vol. 27, no. 2, pp. 5247-5270, 2014.

[13] C. N. R. Rao, "Annu. Rev. Phys. Chem.," 1989.

[14] I. Periodic table of Encyclopedia Britanica, "Periodic table of Encyclopedia Britanica, Inc," 30 April 2020. [Online]. Available: https://www.britannica.com/science/physical-constant. [Accessed 30 04 2020].

[15] C. R. A. J. Chelliah, P. S. T., S. Rajasekar, S. Immanuel, V. Bhojan and S. Rajesh, "Pulsed laser deposited molybdenum oxides (MoO3 & MoO2) thin films for nanoelectronics device application Conference," in *Fourth International Conference on Devices, Circuits and Systems At: Karunya Institute of Technology and Sciences.*, Coimbatore, India, 2018.

[16] H. Okumura, K. Sato and T. Kakeshita, "Electronic structure, defect formation energy, and photovoltaic properties of wurtzite derived CuGaO2;," *Journal of Applied Physics,* vol. 161584, no. 123, 2018.

[17] C. D´ıaz, M. L. Valenzuela, M. A. Laguna-Bercero, A. Orera, D. Bobadilla, S. Abarca and O. Pe˜na., "Synthesis and magnetic properties of nanostructured metallic Co, Mn and Ni oxide materials obtained from solid-state metal macromolecular complex precursors," *RSC Adv., and Prog. Polym. Sci., 2008, 33,,* vol. 27729, no. 7, p. 399–447, 2017.

[18] B. K. Meyer, A. Polity, D. . Reppin, M. Becker, P. Hering, P. J. Klar, T. Sander, C. Reindl, J. Benz, M. Eickhoff, C. Heiliger, M. Heinemann, J. Bl¨asing, A. Krost, S. Shokovets, C. M¨uller and C. Ronning, "Binary copper oxide semiconductors: From materials towards devices," Physica Status Solidi B," *Status Solidi B,* vol. 249, no. 8, pp. 1487-1509, 2012.

[19] M. Umar, S. Y. M, D. L. M. C. Fasolato, M. L, G. G, L. Marot and G. T. a. Z. I, "Morphological and Stoichiometric Optimization of Cu$_2$O Thin Films," *Thin solid films,* 2020, under review.

[20] S. Siol, C. J. Hellmann, S. Tilley, M. Graetzel, J. Morasch, J. Deuermeier, W. Jaegermann and K. A., "Band Alignment Engineering at Cu$_2$O/ZnO Heterointerfaces," *ACS Appl. Mater. Interfaces,,* vol. 8, no. 33, p. 21824–21831, 2016.

[21] C. Kazimierz, "Electronic and ionic conductivity in metal oxides Laboratory for Developments and Methods," 30 4 2020. [Online]. [Accessed 2020].

[22] S. K. Singh and R. Chauhan, "Study of optical properties of transition metal oxides on the basis of energy band and energy state analysis,," *Int. J. Eng. Sci. (IJES),* vol. 3 , no. 6, pp. 37-40, 2014.

[23] A. Millis, "Moment of magnetism.," *Nat. Phys.,,* vol. 749, no. 7, 2011.

[24] P. Kofstad, "Defects and transport properties of metal oxides.," *Oxid Met ,* vol. 44, pp. 3-27, 1995.

[25] E. Fortunato, P. Barquinha and R. Martins, "Oxide Semiconductor Thin Film Transistors: a review of recent advances,," *Adv. Mater.,,* vol. 24, no. 22, pp. 2945-2986, 2012.

[26] L. Petti, N. Münzenrieder, C. Vogt, H. Faber, L. Büthe, G. Cantarella, F. Bottacchi, T. Anthopoulos and G. Tröster, "Metal oxide semiconductor thin-film transistors for flexible electronics,," *Appl. Phys. Rev. 3 021303,* vol. 3, no. 2, p. 021303, 2016.

[27] E. Fortunato, D. Ginley, H. Hosono and D. C. Paine, "Transparent conducting oxides for photovoltaics,," *MRS Bull.,* vol. 32, no. 2, p. 242–247, 2007.

[28] S. Rühle, A. Anderson, H. N. Barad, B. Kupfer, Y. R.-H. E. Bouhadana and Z. Ariel, "All-oxide photovoltaics,," *J. Phys. Chem. Lett., 3, ,* vol. 3, pp. 3755-3764 , 2012.

[29] B. Y. P. Yuhas, "Nanowire-based all-oxide solar cells,," *J. Am. Chem. Soc. ,* no. 131, pp. 3756-3761, 2009.

[30] S. Nakano, N. Saito, k. Miura, T. Sakano, K. Ueda and K. Sugi, "Highly Reliable a-IGZO TFTs on plastic substrate for flexible AMOLED display," *J. Soc. Inf. Disp., 20 ,* pp. 364-371, 2012.

[31] M. Jahangir-Moghadam, K. Ahmadi-Majlan, X. Shen, T. Droubay, M. Bowden, M. Chrysler, D. Su, S. A. Chambers and J. H. Ngai, "Band-Gap Engineering at a Semiconductor-Crystalline Oxide Interface," *Adv. Mater. Interfaces ,* vol. 2 , no. 4, p. 1– 7, 2015.

[32] O. Lupan, V. Cretu, V. Postica, N. Ababii, O. Polonskyi, V. Kaidas, F. Schütt, Y. Mishra, E. Monaico, I. Tiginyanu, V. Sontea, T. Strunskus, F. Faupel and R. Adelung, "Enhanced ethanol vapour sensing performances of copper oxide nanocrystals with mixed phases," *Sens. Actuators B: Chem.,* no. 224, p. 434–448, 2016.

[33] L. Xu, H. Xu, S. Wu and X. Zhang, "Synergy effect over electrodeposited submicron $Cu_2O$ films in photocatalytic degradation of methylene blue," *Appl. Surf. Sci.,* vol. 258, no. 11, p. 4934–4938, 2012.

[34] J. Dong, H. Xu, F. Zhang, C. Chen, L. L. and Wu G, "Synergistic effect over photocatalytic active $Cu_2O$ thin films and their morphological and orientationnal transformation under visible light irradiation," *Appl. Catal. A,* vol. 470, p. 294–302., 2014.

[35] A. J. Deka B. J. and Thakur, "A review on solid oxide derived from waste shells as catalyst for biodiesel production.," *Renew Sust. Energy Rev.,* vol. 16, pp. 904-910, 2012.

[36] Simberg, D.; Park, J. H.; Karmali, P. P. ; Zhang, W. M.; Merkulov, S.; McCrae, K.; Bhatia, S.; Sailor, M.;Ruoslahti, E., "Differential proteomics analysis of the surface heterogeneity of dextran iron oxide nanoparticles and the implications for their in vivo," pp. 3926-33, 2006.

[37] E. Roduner, "Size matters: why nanomaterials are different,," *Chem. Soc. Rev.,* vol. 35, pp.

583-592, 2006.

[38]   R. Jose, T. Velmurugan and R. Seeram, "Metal oxides for dye-sensitized solar cells," *J. Am. Ceramic Soc,* vol. 92, p. 289–301, 2009.

[39]   A. L. Fahrenbruch and R. H. Bube, " Polycrystalline thin films for solar cells.," in *Fundamentals of solar cells,*, Eds. (eds.) ed., vol. 9, Academic Press, 1983, p. 330–416..

[40]   N. Elumalai, M. A. Mahmud, D. Wang and A. Udin, "Perovskite solar cell: progress and advancements,," *Energies,* vol. 9, no. 11, p. 861, 2016,.

[41]   M. A. Green, Solar cells: operating principles, technology, and system applications, Englewood Cliffs: Englewood Cliffs, Prentice-Hall, 1982.

[42]   G. F. W. J. Brown, "Third generation of photovoltaics Laser & Photonic reviews.," vol. 3, no. 4, pp. 394-405, 2009.

[43]   D. A. Eisenberg, M. Yu, C. W. Lam, O. A. Ogunseitan and J. M. Schoenung, "Comparative alternative materials assessment to screen toxicity hazards in the life cycle of CIGS thin film photovoltaics," *Journal of Hazardous Materials. ,* vol. 260, p. 534–542, 2013.

[44]   N. Vlachopoulos, P. Liska, A. J. and M. Gratzel, "Very efficient visible light energy harvesting and conversion," *Journal of the American Chemical Society,* vol. 110, no. 4, pp. 1216-1220, 1988.

[45]   T. S. Gershon, "Metal oxide applications in organic-based photovoltaics," *Material Science and Technology ,* vol. 27, no. 2, pp. 1357-1371,, 2011.

[46]   I. Celik, C. Z. Song, J. A. Y. Yan, J. M. Heben, J. Michael and D. Apul, "Life Cycle Assessment (LCA) of perovskite PV cells projected from lab to fab," *Solar Energy Materials and Solar Cells,* vol. 156:, p. 157–69., 2016.

[47]   K. Hironori, S. Kotoe, W. Tsukasa, S. Hiroyuki, K. Tomomi and M. Shinsuke, "Development of thin film solar cell based on Cu2ZnSnS4," *thin films. Sol. Energy Mater. Sol. Cells ,* vol. 65, no. 1-4, pp. 141-148, 2001.

[48]   M. Jiang and X. and Yan, " "Cu2ZnSnS4 thin film solar cells: present status and future prospects,"," in *Solar Cells-Research and Application Perspective*, E. A. Morales-Acevedo, Ed., Rijeka,, InTech, , 2013.

[49]   J. Wang, V. Ibarra, B. D, L. Xu, L. y and W. a. H. P. Julia, "Solution Synthesised p-type copper gallium oxide nanoplates as hole transport layer for organic photovoltaic devices,," *Journal of Physical Chemistry Letters, ,* vol. 6, no. 6, pp. 1071-1075, 2015.

[50] J. Tian and G. Cao, "Control of nanostructures and interface of metal oxidesemiconductors for quantum-dot-sensitized solar cell,," *Journal of Physical Chemistry Letters,,* vol. 6, pp. 1859-1869, 30 April 2105.

[51] L. Tsakalakos and J. F. J. a. K. Balch, "Silicon nanowire solar cell," *Applies Physical Letters,,* vol. 9, no. 23, p. 233117, 2007.

[52] T. Subramani, J. Chen, Y. L. Sun, W. Jevasuwan and F. N., "High-efficiency silicon hybrid solar cells employing nanocrystalline Si quantum dots and Si nanotips for energy management," *Nanomater Energy,* vol. 35, pp. 154-160, 2017.

[53] L. Dai, C. H. Sow, Lim, C.T and V. and Tan, "Metal Oxide Nanowires," in *Fundamental Research,*, A. H. (Ed., Ed., Fundamental Research, Abbass Hashim (Ed., InTech, 2011.

[54] H. Yu and A. J. L. D. A. W. L. Stapleton, " High performance flexible metal oxide /silver nanowire based transparent conductive films by scalable lamination-assisted solution method,," *Journal of Materiomics,,* vol. 3, no. 1, pp. 77-82, 2017.

[55] A. W. K. P. Musselman, D. C. Iza, H. C. Hesse, C. Scheu, J. L. MacManus-Driscoll and L. Schmidt-Mende, "Incompactible length scales in nanostructured $Cu_2O$ solar cells," *Journal of Advanced Functional Material,* vol. 22, no. 10, pp. 2202-2208, 2012.

[56] M. S. Bhuiyan, M. Paranthaman and K. Salama, ""Solution-derived Textured Oxide Thin Films-a review".," *Super Cond Sci. Technol.,* Vols. R1-R2., 2006.

[57] W. L. Hughes, "Synthesis and Characterization of ZnO Nanostructure for Piezoelectric Application"," Georgia Institute of Technology, U.S.A., 2006.

[58] S. Wolf and R. N. Tauber, "Silicon Processing for the VLSI Era," *Process technology,* vol. 1, p. 15, 1986.

[59] R. Madar and C. Bernard, "Thermodynamic modelling of selective chemical vapor deposition processes in Microelectronic silicon," *Journal Vacuum Science Technology,,* vol. A (8), no. 1413, 1990.

[60] D. Uhiman T. Surtwala, K. Davidson, J.M Boulton, and G. Teowee, Journal of Non Crystalline Solids, 218, 113. 1997.

[61] D. M. Mattox, Sputter deposition, in: The Foundations of Vacuum Coating Technology: A Concise Look at the Discoveries, Inventions, and the People behind Vacuum Coating, Past and Present,, Noyes Publications,, 2003, p. 11.

[62] K. L. Chopra and S. R. Das, Thin Film Solar Cells,, New York: Plenum press,, 1983.

[63] D. L. Smith, Thin-Film Deposition Principles and Practice, Washington D.C: Mc Graw Hill Inc, 1995.

[64] D. M. Mattox, "Physical sputtering and sputter deposition (sputtering),," in *Handbook of Physical Vapor Deposition (PVD) Processing*, 2nd edition ed., 2010, pp. 237-286.

[65] J. E. Mahan, "Physical Vapor Deposition of Thin Film",, John Wiley & Sons, Inc., 2000.

[66] M-T Le, Y-Un Sohn, J-W Lim and G-S Choi " Effect of Sputtering power on the nucleation and growth of Cu films deposited by magnetron sputtering,," *Material Transactions,,* vol. 51, no. 1, pp. 116-120, 2010.

[67] O. S. Heavens, Thin Film Physics,, First Edition, ed., Vols. 1, 533., London: Methuen & Co and Science Paperback, 1970.

[68] M. Ohring, The Materials Science of thin films Stevens Institute of Technology Department of Materials Science and Engineering Hoboken, New Jersey: Academic Press, 1992, pp. 22-23..

[69] S. C. Ray, "Preparation of Copper Oxide Thin Film by the Sol–gel like Dip Technique and Study of their Structural and Optical Properties," *Sol. Energy Mater. Sol. Cells,* vol. 68, no. 3-4, p. 307–312, 2001.

[70] E. Carbó-Argibay, X.-Q. Bao, C. Rodríguez-Abreu, M. P. D. Cerqueira, L. Liu and Y. Kolen'ko, "Up-scaling the Synthesis of $Cu_2O$ Submicron Particles with Controlled Morphologies for Solar H2 Evolution from Water," *J Colloid Interface Sci,* vol. 456, pp. 219-227, 2015.

[71] K. Self and W. Zhou, "Surface Charge Driven Growth of Eight-Branched $Cu_2O$ Crystals X Cryst," *Growth Des.,* vol. 16, p. 5377−538, 2016.

[72] V. Figueiredo, E. Elangovan, G. Goncalves, P. Barquinha, L. Pereira, N. Franco, E. Alves, R. Martins and E. Fortunato, "Effect of post-annealing on the properties of copper oxide thin films obtained from the oxidation of evaporated metallic copper," *Appl. Surf. Sci.,* Vols. 254,, p. 3949–3954, 2007.

[73] L.-K. Liau, Y.-C. Lin and Y.-J. Peng, "Fabrication Pathways of p-n $Cu_2O$ Homojunction Films by Electrochemical Deposition Processing.," *J Phys Chem C,* vol. 117, no. 50, pp. 26426-26431, 2013.

[74] J. Hsieh, P. Kuo, K. Peng, S. Liu, J. Hsueh and S. Chang, "Opto-electronic properties of sputter-deposited $Cu_2O$ films treated with rapid thermal annealing," *Thin Solid Films,* vol. 516, no. 16, pp. 5449-5453, 2008.

[75] A. S. Reddy, G. V. Rao, S. Uthanna and P. S. Reddy, "Structural and optical studies on dc reactive magnetron sputtered $Cu_2O$," *films Mater. Lett., ,* vol. 60, no. 13-14, pp. 1617-1621, 2006.

[76] Y. S. Lee, M. T. Winkler, S.C. Siah, R. Brandt "Hall mobility of cuprous oxide thin films deposited by reactive direct-current magnetron sputtering," *Appl. Phys. Lett.,* vol. 98, p. 192115, 2011.

[77] C.-C. Hsu, C. H. Wu and Y. S. Wang, "Low power deposition of the polycrystalline $Cu_2O$ film with a high mobility and a low hole concentration by radio-frequency magnetron sputtering of a $Cu_2O$ target,," *J. Alloy. Compd,* vol. 663., p. 262–269, 2016.

[78] B. Purusottam-Reddy, K. Sivajee-Ganesh, K. Jayanth-Babu, O. Hussain and C. Julien, "Microstructure and super capacitive properties of rf-sputtered copper oxide thin films: influence of O2/Ar ratio," *Ionics , ,* vol. 21, no. 8, p. 2319–2328, 2015.

[79] E. Camacho-Espinosa, I. Rimmaudo, I. Reich, R. Mis-Fernàndez and J. Peña, "Stability of sputter Deposited Cuprous Oxide ($Cu_2O$) Subjected to ageing Conditions for Photovoltaic Application," *Journal of Applied Physics ,* vol. 123, p. 085301, 2018.

[80] M. Lenglet, K. Kartouni, J. Machefert, J. M. Claude, P. Steinmetz, E. Beauprez, J. Heinrich and N. Celati, "Low temperature oxidation of copper: The formation of CuO,," *Mater. Res. Bull.,* vol. 30, no. 4, p. 393–403, 1995.

[81] L.-J. Asbrink S. and Norby, Acta Crystallogr., 8, Ed., B 26, 1970.

[82] G. Papadimitropoulos, N. Vourdas, V. Vamvakas and D. Davazoglou, "Deposition and characterization of copper oxide thin films,," *Journal of Physics: Conference Series,* vol. 10, pp. 182-185., 2005.

[83] F. Marabelli, G. B. . Parravicini and F. Salghetti-Drioli, *Phys. Rev. B ,* p. 1433, 1995.

[84] A. Thobor and J. Pierson, "Properties and air annealing of paramelaconite thin films," *Materials Letters,* vol. 57, no. 22-23, pp. 3676-3680, 2003.

[85] C. Frondel, "Paramelaconite: A tetragonal oxide of copper," *American Mineralogist,* vol. 26 , no. 11, p. 657–672., 1941.

[86] M. O'Keeffe and J.-O. Bovin, "The crystal structure of paramelaconite, Cu4O3,," *American Mineralogist,,* vol. 63, pp. 180 -185,, 1978.

[87] N. Datta and Jeffery J. W, "The crystal structure of paramelaconite, Cu122+Cu4+O14," *Acta Cryst.,* vol. B34, pp. 22-26, 1978.

[88] L. O. Grondahl, "unidirectional current carrying device," *US Patent,,* 1925.

[89] L. O. Grondahl and P. H. Geiger, "A new rectifier," *IEEE Journal,* vol. 46, pp. 215-222, 1927.

[90] A. E. Rakshani, "Preparation, Characterization and photovoltaic properties of cuprous oxide – a review," *Solid State Electronics,* vol. 29, no. 1, pp. 7-17, January 1986.

[91] W. Shockley and H. J. Queisser, "Detailed Balance Limit of Efficiency of p-n Junction Solar cells," *Journal of applied Physics,* vol. 32, no. 3, p. 510, 1961.

[92] J. W. Hodby, T. E. Jenkins, C. Schwab, H. Tamura and T. D., "Cyclotron resonance of electrons and of holes in cuprous oxide, $Cu_2O$,," *Journal of Physics C: Solid State Physics, ,* vol. 9, no. 8, 28 04 1976.

[93] S. Ishizuka, T. Maruyama and K. Akimoto, "Thin film deposition of $Cu_2O$ by reactive radio-frequency magnetron sputtering," *J. Appl. Phys.,* vol. 39, pp. L786- L788, 2000.

[94] D. Cakir, Enhanced Raman signatures on copper based-materials. Other [cond-mat.other], Université Montpellier: HAL, 2017.

[95] Cuprite—Web mineral. Available from: http://www.webmineral.com/data/Cuprite.shtml, 2010. [Online].

[96] M. Heinemann, B. Eifert and C. Heiliger, "Band structure and phase stability of the copper oxides $Cu_2O$, CuO, and Cu4O3," *physical Review B,* vol. 87, p. 115111, 2013.

[97] T. Ohyama, T. Ogawa and H. Nakata, "Determination of deformation-potentials constants of $Cu_2O$ by microwave cyclotron resonance," *Phys. Rev. B ,* vol. 56, p. 3871, 1997.

[98] M. S. Abbas, M. Mahdi and Z. Hassan, "Fabrication of $Cu_2O$ nanocrystalline thin films photosensor prepared by RF sputtering technique," *Physical E ,* vol. 94, pp. 132-138, 2017.

[99] Z. Yao, S. Liu, L. Zhang, B. He, A. Kumar and X. Jiang, "Room temperature fabrication of p-channel $Cu_2O$ thin-film transistors on flexible polyethylene terephthalate substrates," *Appl. Phys. Lett.,* vol. 101, no. 4, p. 042114, 2012.

[100] S. S. Guru Srinivasan, B. Govardhanan, P. Aabel, M. Ashok and K. M. Santhosh, "ffect of oxygen partial pressure on the tuning of copper oxide thin films by reactive sputtering solar light driven photocatalysis," *Solar Energy ,* vol. 187, p. 368–378, 2019.

[101] A. Rydosz, "Amorphous and Nanocrystalline Magnetron Sputtered CuO Thin Films Deposited on Low Temperature Cofired Ceramics Substrates for Gas Sensor Applications," *IEEE Sensors J.,* vol. 14, no. 5, pp. 1600-1607 , 2014.

[102] L.-C. Wang, H. Jia, L.-Y. Shi, N. Liao, X.-J. Yu and D.-L. Jin, "Controlled synthesis of $Cu_2O$ micro-crystals with various morphologies by adjusting solution conditions.," *Inorg. Mater. ,* vol. 46, p. 847−851, 2010.

[103] W. H. Brattain, "The copper oxide rectifier," *Rev. Mod. Phys.,* vol. 23, p. 203, 01 07 1951.

[104] C. Carel, M. Mouallem-Bahout and Gaude´ J., "Re-examination of the non-stoichiometry and defect structure of copper(II) oxide or tenorite, Cu 1± z O or CuO 1± $\epsilon$," *Solid State Ion.,* vol. 117, p. 47, 1999.

[105] O. Scanlon, B. J. Morgan, G. W. Watson and A. Walsh, "Acceptor levels in p-type $Cu_2O$: rationalizing theory and experiment,," *Phys. Rev. Lett.,* vol. 103, p. 096405, 2009.

[106] J. P. Hu, D. J. Payne, R. G. Egdell, P. A. Glans, T. Learmonth, K. E. Smith, J. Guo and N. M. Harrison, "On-site interband excitations in resonant inelastic x-ray scattering from $Cu_2O$," *Phys. Rev. B,* vol. 77, p. 155115, 2008.

[107] RF Magnetron sputtering deposition system,, "[www.e-asact.org e-ISSN," [Online].

[108] L. I. Maissel and R. Gland, Handbook of thin film Technology,, New York, 1970., pp. 1103-1105..

[109] K. Denishev, "Some metal oxides and their applications for creation of microsystem (MEMS) and energy harvesting devices (EHD)," *Journal of Physics: Conference series,,* vol. 764, July 2016.

[110] K. H. Behrndt, New Structures in Metal Films Deposited at Low Temperatures.

[111] Schematic of a scanning electron microscope (online).

[112] G. Binnig, C. F. . Quate and G. Ch., "Atomic Force Microscope," *Phys. Rev. Lett.,* vol. 56, p. 930–933, 1986.

[113] W. Melitz, J. Shen, A. C. Kummel and S. Lee, "Kelvin probe force microscopy and its application,," *Surface Science Reports,* vol. 66, no. 1, p. 1 – 27, 2011.

[114] G. Günzburger, "Nanoscale characterization of dye sensitized solar cells - Kelvin probe force microscopy in liquid. Doctoral Thesis,," University of Basel, Faculty of Science, Basel, 2015.

[115] V. Lord Kelvin, "Contact electricity of metals," *Philosophical Magazine Series,* vol. 5, 1898.

[116] S Sadewasser, T. Glatzel " Experimental Technique and Working Modes. In: Sadewasser S., Glatzel T. (eds) Kelvin Probe Force Microscopy.," *Springer Series in Surface Sciences,* vol. vol 65, (2018).

[117] C. Sommerhalter, T. W. Matthes, T. Glatzel, A. Jäger-Waldau and M. C. Lux-Steiner, "High-sensitivity quantitative Kelvin probe microscopy by noncontact ultra-high-vacuum atomic force microscopy," *Appl. Phys. Lett.,* vol. 75, p. 286, 1999 .

[118] S. Sadewasser and T. Glatzel, "Kelvin Probe Force Microscopy," in *Springer Series in Surface Sciences* , vol. 48, Berlin Heidelberg:, 2012.

[119] W. G. Moffat, G. W. Parsall and J. Wuiff, The structure and properties of material Structure., vol. 1, John wiley and sons.,Inc., 1964, p. 208.

[120] J. I. Goldstein, D. E. Newbury, P. Echlin, D. Joy, A. D. Romig Jr, C. E. Lyman and E. Lifshin,, "Scanning Electron Microscopy and X-Ray Microanalysis", A text for Biologists,

Materials Scientists and Geologists, Second Edition ed., New York: Plenum Press, 1999.

[121] A. Segmüller, "Characterization of Epitaxial thin films by X-ray diffraction," *J. Vac. Sci. Technol.,* vol. A9:2477.

[122] R. Poilblanc and F. ,. Crasnier, "Spectroscopies infrarouge et Raman," *Grenoble sciences: EDP sciences,* 2006.

[123] N. B. Colthup, L. H. Daly and W. S. W. E., Introduction to Infrared and Raman spectroscopy, London academic press, 1990.

[124] C. Fasolato, I. Zardo, and M. De Luca, "Addressing crystal structure in semiconductor nanowires by polarized Raman spectroscopy," Ch 9 Nanowire (Springer), under review.

[125] J. Chrzanowsk and J. C. and Irwin, "Raman scattering from cupric oxide Solid State," *Communication,* vol. 70, pp. 11-14, 1989.

[126] L. Debbichi, M. C. Marco de Lucas, P. J. F and P. ". and Kruger, "Vibrational properties of CuO and Cu4O3 from first-principles calculations, and Raman and infrared spectroscopy,," *The Journal of Physical Chemistry C,,* vol. 116, no. 18, pp. 10232-10237, 2012.

[127] D. Powell, A. Compaan and J. R. Macdonald, "Raman-scattering study of ion-implantation-produced damage in $Cu_2O$," *Phys. Rev. B,* vol. 12, no. 1, p. 20, 1975.

[128] K. Reimann and K. and Syassen, "Raman scattering and photoluminescence in $Cu_2O$ under hydrostatic pressure," *Phys. Rev. B,* vol. 39, no. 15, p. 11113, 1989.

[129] R. J. Elliott, "Symmetry of Excitons in $Cu_2O$," *Phys. Rev.,* vol. 1242, pp. 340-345, 1961.

[130] L. Ren, X. Su, Y. Wang and J. a. N. K. Xu, "QSpec: online control and data analysis system for single-cell Raman spectroscopy," in *PeerJ 2: e436].*

[131] J. I. Pankove, Optical processes in semiconductors,, New York.: Prentice-Hall,, 1971.

[132] F. Wooten, Optical properties of solids,, New York: Academic Press. , 1972.

[133] E. Kusano, "Structure-Zone Modeling of Sputter-Deposited Thin Films: A Brief Review," *Applied Science and Convergence Technology,* vol. 28, no. 6, pp. 179-185, 2019.

[134] R. Y. J. E. Messier, "Voids: Geometry of thin film morphology," *J. Appl. Phys,* vol. 58:3739., 1985.

[135] V. Subramanian, P. K. Bhattacharya and A. A. Memon, "Chemical contamination of thin oxides and native silicon for use in modern device processing," *International Journal of Electronics,* vol. 78, no. 3, 2007.

[136] B. Singh and B. Mehta, "Relationship between nature of metal-oxide contacts and resistive switching properties of copper oxide thin film based devices," *Thin Solid Films,* vol. 569, p. 35–43, 2014.

[137] Z. Weifeng, C. Yue, P. Xihong, Z. Kehua, L. Yingbin and H. Zhigao, "The Phase Evolution and Physical Properties of Binary Copper Oxide Thin Films Prepared by Reactive Magnetron Sputtering," *Materials,* vol. 11, no. 1253, 2018.

[138] O. Messaoudi, H. Makhlouf, A. A. I. B. Souissi, G. Amiri, A. Bardaoui, M. Oueslati, M. Bechelany and R. Chtourou, "Synthesis and characterization of ZnO/Cu$_2$O core–shell nanowires grown by two-step electrodeposition method," *Appl. Surf. Sci.,* vol. 343, pp. 148-152, 2015.

[139] M. T. S. Nair, L. Guerrero, O. Arenas and P. Nair, "Chemically deposited copper oxide thin films: structural, optical and electrical characteristics," *Appl. Surf. Sci. ,* vol. 150, p. 143–151, 1999.

[140] Y. Wang, J. Ghanbaja, F. Soldera, S. Migot, P. Boulet, D. Horwat, F. Mücklich and J.-F. Pierson, "Tuning the structure and preferred orientation in reactively sputtered copper oxide thin films," *Appl. Surf. Sci.,* vol. 335, p. 85–91, 2015.

[141] Y. P. Yu and Y. R. Shen, "Resonance Raman studies in Cu$_2$O. I. The Phonon-assisted 1s yellow excitonic absorption edge," *Phys. Rev. B,* vol. 12, p. 1377, 1975.

[142] N. A. Mohemmed Shanid, M. AbdulKhadar and V.G. Sathe, " Frohlich interaction and associated resonance enhancement in nanostructured copper oxide films.," *J. Raman Spectrosc.,* vol. 42, p. 1769 – 1773 , 2011.

[143] H. Solache-Carranco, G. Juaˊ rez-Dıˊaz, A. Esparza-Garcıˊa, M. Brisen˜o-Garcıˊa, M. Galvaˊn-Arellano, J. Martıˊnez-Juaˊ rez, G. Romero-Paredes and R. Pen˜a-Sierra, "Photoluminescence and X-ray diffraction studies on Cu$_2$O," *Journal of Luminescence,* vol. 129, no. 12, p. 1483–1487, 2009.

[144] F. A. Akgul, G. Akgul, N. Yildirim, H. E. Unalan and R. Turan, "Influence of thermal annealing on microstructural, morphological, optical properties and surface electronic structure of copper oxide thin film," *Material chemistry and physics,* vol. 147, pp. 987-995, 2014.

[145] Y. Kong, H. S, F. W. L. Wang, Z. Hongkai, X. Zhao and S. Xian and Yuan, "Enhanced photoelectrochemical performance of tungsten oxide film by bifunctional Au nanoparticles," *RSC Advances,,* vol. 25, no. 7, pp. 15201-15210, 2017.

[146] Z. H. Gan, G. Q. Yu, B. K. Tay, C. M. Tan, Z. W. Zhao and Y. Q. Fu, "Preparation and Characterization of Copper Oxide Thin Flms Deposited by filtered Cathodic Vacuum Arc," *J.*

# List of Tables

# List of Figures

Fig. 5.5b. The experimental data are the result of averaging over two positions on the samples, and the error bars represent the corresponding semi-dispersion. Data (in both panels a and b) refer to the 23% $O_2$ sample.     60

5.8 Raman spectra magnified in the frequency region of the $Cu_2O$ mode at 216 $cm^{-1}$ acquired on twelve different positions of the samples prepared with 15% (panel a) and 23% (panel b) $O_2$ partial pressure and annealed at 500 °C. Dashed lines mark variation in central frequency of the mode, that for a) is about 2 $cm^{-1}$ and for b) is about 1.2 $cm^{-1}$. Data were obtained by mapping the sample over an area of 6 x 6 $\mu m^2$ with steps of 0.5 $\mu m$. An offset was added between spectra. Fluctuations in the intensity can be attributed to slightly different focusing conditions (the focus was not optimized in each point, as it was instead done in the single point measurements in Fig. 5.6).     62

5.9 SEM surface morphology of sputtered thin films on Si substrates deposited at 23% $O_2$ partial pressure before annealing treatments. All three films were deposited with nominally the same parameters in different, not simultaneous, deposition processes. Panels a, b and c represent second, third and fourth depositions, hence, will be referred to as S2, S3 and S4, respectively.     63

5.10 XRD patterns of nanoporous thin films prepared on Si substrates by RF-magnetron sputtering at nominally 23% $O_2$ partial pressure for all three depositions. Panel a refers to the as-deposited films and panel b to the annealed films at 500°C. The triangles and circles indicate peaks attributed to $Cu_2O$ or CuO, respectively, and the dashed lines highlight their evolution. The spectra are vertically shifted for clarity.     65

5.11 Raman spectra of nanoporous thin films prepared on Si substrates by RF-magnetron sputtering at nominally 23% $O_2$ partial pressure for all three depositions. Panel a refers to the as-deposited films and panel b to the annealed films at 500°C. Peaks attributed to $Cu_2O$ or CuO are indicated by triangles and circles, respectively. The thickness of the S3 film screens the contribution of the Si substrate peak at 521 $cm^{-1}$, as discussed in 5.1. The spectra were vertically shifted for clarity. The black line shows the peak evolution.     66

5.12 EDX spectra and inset with the SEM micrograph showing the as-deposited sputtered thin films deposited at 15% (a panel) and 23% (b panel) $O_2$ partial pressure. The data acquired on an area of 1 x 1 $\mu m^2$. The table beneath the graph shows the Cu to O elemental contents in weight (Wt %) and atomic (At %).     68

5.13 XRD spectra of the as-deposited thin films prepared onto Si and FTO-coated substrates by RF-magnetron sputtering at 15% and 23% $O_2$ partial pressure. The olive color spectrum is the FTO reference sample and it shows that indeed most of the peaks are

coming from the FTO layer of the substrates. The black line is showing the evolution of the peaks. The observed shift in the blue spectra could be a result of strain created by $Cu_xO$ when deposited on top of the FTO layer. Therefore, we did not use the FTO peaks to calibrate the raw data.

5.14 shows XRD peaks of the pristine thin film deposited at 15% $O_2$ partial pressure with an inset. The inset shows the difference of the FTO-coated layer from the $Cu_2O$ deposited layer. The upper peaks are the $Cu_xO$ while the lower peaks belong to the FTO peaks of the substrates.

5.15 XRD reference spectra, panel a shows XRD peaks obtained from an existing reference. Panel b shows the FTO spectra of the substrates used for this project. All the peak positions from both panels are very similar though panel a is from 10-70° while panel b is from 20-70°.

5.16 Raman spectra of the as-deposited thin films prepared on Si and FTO-coated substrates. As shown also in Figure 5.6, Raman signals of pristine samples are very weak. Therefore, here the spectra have been arbitrarily rescaled in order to enhance the visibility of the peaks.

5.17a SEM surface morphology of sputtered thin films onto FTO coated glass substrates. Top panels refer to deposition at 23% and bottom panels to 15% $O_2$ partial pressure. Annealing temperature increases from left to right.

5.17b SEM cross sections of sputtered thin films onto FTO coated glass substrates. Left and right panels  refer to deposition at 15% and 23% $O_2$ partial pressure, showing a thicknesses of ~150 nm and ~157 nm, respectively

5.18 XRD patterns of nanoporous thin films sputtered onto FTO-coated glass substrates by RF-magnetron sputtering at 15% (panel a) and 23% (panel b) $O_2$ partial pressure. Triangles and circles indicate peaks attributed to $Cu_2O$ or $CuO$, respectively. The spectra are vertically shifted for clarity. Annealing temperature increases from bottom to top. The panels below are a zoom of the top panels. The black lines are drawn to show peak evolution.

5.19 Raman spectra of nanoporous thin films sputtered onto FTO coated glass substrates by RF-magnetron sputtering at 15% (panel a) and 23% (panel b) $O_2$ partial pressure. The spectra were vertically shifted for clarity. Annealing temperature increases from bottom to top. The triangles and circles identify $Cu_2O$ and $CuO$, respectively.

observed in the samples when they were imaged immediately after the deposition. 83

**Medina Umar**
**Curriculum Vitae**

**PERSONAL DETAILS**

| | | | |
|---|---|---|---|
| **Date of birth** | 28$^{th}$ July 1982 | **Address** | 19, Ikaraworo street, |
| **Nationality** | Nigerian | | |
| **Email** | mails4medina@gmail.com | **Telephone** | Okene, Kogi State. |
| | | | +2348056417576 |

**EDUCATION**

| | |
|---|---|
| **2018-2020** | **PhD in Physics** at University of Basel, Switzerland |
| | Dissertation: "Deposition and Characterization of Wide Band Gap P-Type Metal Oxides for Photovoltaic Applications" |
| **2016-2017** | **(1$^{st}$ year) PhD in Physics** at Peoples' Friendship University of Russia, Moscow, Russia |
| **2010-2013** | **Master of Science** (Solid State Physics) at University of Abuja, Abuja |
| | Thesis: "Preparation and Characterization of Structural, Optical and Electrical Properties of PbSe Thin Film Using Chemical Bath Deposition Technique" |
| **2000-2006** | **Bachelor of Technology** (Physics /Computer Science), Federal University of Technology, Minna, Nigeria |
| | Project: Study of the Moisture Content and Bulk Density of Soil in Relation to its Temperature Values: A Case Study of Soils Around Bosso Campus of the Federal University of Technology, Minna, North Central Nigeria |
| **1992-1998** | **Senior School Certificate of Education (SSCE)**, Anglican Secondary School, Makurdi |

**FELLOSHIPS AND AWARD**

| | |
|---|---|
| **2020** | Förderbeitrag from the Freiwillige Akademische Gesellschaft (Switzerland) |
| **2016** | Study Fellowship Award from the University of Abuja (Nigeria) under the NEEDS |

## PUBLICATIONS

---

- **M. Umar**, M.Y. Swinkles, M. De-Luca, C. Fasolato, L. Moser, G. Gadea Diez, L. Marot, T. Glatzel and I. Zardo. *Morphological and stoichiometric optimization of $Cu_2O$ thin films by deposition conditions and post-growth annealing*. Thin Solid Films Volume 732, 31 August 2021, 138763 https://doi.org/10.1016/j.tsf.2021.138763
- Y.P. Rybakov, **M. Umar**, M. Iskandar, *Mechanical Properties of Carbon Nanotubes in a Chiral Model of Graphene*. J. Mech. Cont. & Math. Sci., Special Issue-1, 420-428 (2019) https://doi.org/10.26782/jmcms.2019.03.00041
- A.D.A. Buba, **M. Umar**, M.U. Gurku *Temperature Dependence of Optical Properties of PbSe Thin Films*. IOSR Journal of Applied Physics **8**(2), 56-61 (2016)
- Alayande, S.O., Akinlabi, A.K., Adewaleomosalewa .O. Ofudje, A., Ezeh, G., **Umar, M.,** Tubosun.I. E-Waste Burning: Impact on Metal Components of Dumpsites around Alaba Market, Lagos, Nigeria. *Journal Chemical Society of Nigeria, Vol. 40 No.1 pp 96-101* (2015).
- J.S.A. Adelabu, **M. Umar**, S. A. Jonah, J.O. Adeniyi, and I.E. Crown, *A Study of the Moisture Content and Bulk Density of Soil in Relation to its Temperature Values: A Case Study of Soils Around Bosso Campus of the Federal University of Technology, Minna, North Central Nigeria*. Environmental Technology and Science Journal (ETSJ), **4** (1), 97-106 (2011)

## HOBBIES

---

Reading, Watching Documentaries, Travelling